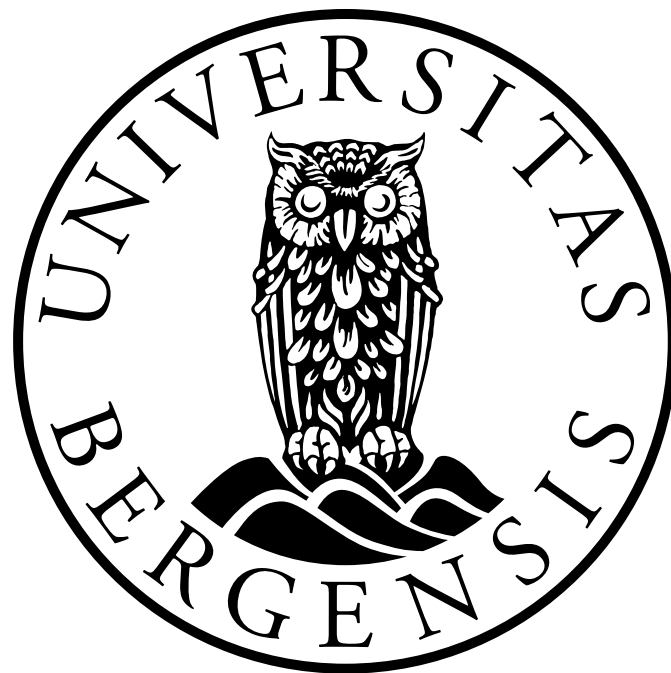# Controls on deformation band formation in carbonate grainstones along the Maghlaq Fault, Malta

MASTER THESIS
BASIN AND RESERVOIR STUDIES

Knut Ringen VITEN

UNIVERSITY OF BERGEN

DEPARTMENT OF EARTH SCIENCE

June, 2018

Abstract

Deformation bands are common structures in deformed porous rocks and sediments, that localise strain in millimetre to centimetre thick tabular zones. Deformation bands occurring in siliciclastic rocks have been described and studied in great detail over the last four decades, but only recently have the equivalent structures in carbonate rocks been allocated significant academic attention. The knowledge about how deformation bands evolve and affect petrophysical properties of the host rock is thus less established in carbonate rocks, prompting this study. Here, results of outcrop mapping and extensive analysis of microscopic observations are combined to determine the controlling factors on deformation band formation in the hangingwall of the extensional Maghlaq Fault on the southwestern coast of Malta. The studied deformation bands are outcropping in the carbonate grainstones of the Miocene Globigerina Limestone Formation (GLF), more specifically in the Lower Globigerina Member (LGLM) and the Middle Globigerina Member (MGLM).

By means of micro-structural observations, the studied deformation bands were in terms of kinematics classified as compactional shear bands (CSB). Porosity reductions of up to one order of magnitude were measured inside CSBs, relative to the host rock. At the outcrop, CSBs with similar orientations are recorded in both LGLM and MGLM, but the frequency of bands in LGLM is significantly higher than in MGLM. Microanalysis determined that different deformation mechanisms have dominated the strain localisation in the two stratigraphic members, with pressure solution dominating in LGLM compated to cataclasis combined with granular flow in MGLM. The preferential nucleation of CSBs in one unit over the other can, on the basis observations in the study, be attributed to the following controlling factors: (i) larger echinoderm grain size, leading to fewer grain contact points which enhances pressure solution, (ii) higher proportion of intergranular porosity which enables more deformation by granular flow and (iii) lesser proportion of foraminifera bioclasts, who resist deformation by cataclasis and pressure solution more than other bioclasts in the grain assemblage.

Deformation bands are known to affect fluid flow patterns in permeable, potential reservoir rocks. Further knowledge on how they form in porous carbonate rocks and which host rock properties promote their formation can help to predict the location and effect of subseismic deformation bands. The findings of this study can thus be of importance to projects related to geothermal reservoirs, groundwater aquifers, CO_2 storage and production of hydrocarbons from carbonate reservoirs.

Acknowledgments

v

Contents

Chapter 1

Introduction

This study builds upon two previous M.Sc. projects from 2015 (Thorsheim, 2015; Fossmark, 2015), where deformation bands in porous grainstones along the Maghlaq Fault, Malta, were studied in detail for the first time. These two projects focused on the spatial distribution and evolution of deformation bands, their microstructural properties and influence on fluid flow. This current study investigates controls on deformation band formation in carbonate grainstones by comparing observations both on the macro and micro scale.

1.1 Rationale

Deformation bands are defined as tabular zones of localized shear and/or volumetric compaction or dilatation, commonly found in porous rocks either as single structures or in the damage zone of proximal faults (Aydin, 1978; Antonellini et al., 1994; Fossen and Bale, 2007). The fact that deformation bands occur in potential reservoir rocks for geofluids have made understanding and predicting their formation and petrophysical properties a keen topic of interest as they impact the porosity and permeability of the host rock (Antonellini and Aydin, 1994; Fossen and Bale, 2007). The recent push for the implementation of carbon capture and storage (CCS), have further increased the need to better understand how sub-seismic structures affect fluid flow and reservoir compartmentalisation. Historically, their occurrence have been extensively documented in porous siliciclastic rocks (Fossen et al. (2007), and references therein) since the first discriptions by Aydin (1978) in the San Rafael Desert, Utah. However, over the last decade more literature regarding deformation bands in porous carbonates have been published (Tondi et al., 2006; Tondi, 2007; Rath et al., 2011; Rustichelli et al., 2012; Wennberg et al., 2013; Antonellini et al., 2014; Rotevatn et al., 2016b).

Although increased attention has been given to deformation bands in carbonate rocks over the last decade, big questions related to controls on their formation remain

unanswered. Whether it is the grain assemblage, porosity distribution or cement-content in carbonate grainstones that is the dominating control on the formation of deformation bands is still under debate (Baud et al., 2009; Vajdova et al., 2012). The well exposed grainstones in the hangingwall of the Maghlaq Fault, Malta, allows for extensive research into these topics through field scale mapping of the deformation band distributions and microscopic analysis of samples collected from the outcrop. The aims and objectives of this specific thesis are defined in the following section.

1.2 Aims and objectives

The primary aim of this thesis is to investigate and improve the knowledge about the nucleation and evolution of deformation bands in carbonate grainstones by comparing outcrop observations with thin section analysis of both host rock and deformation band samples. Specifically, the thesis aims to: (i) analyse and describe characteristics of host rock and deformation bands within the carbonate grainstones of the Globigerina Limestone Formation, in the hangingwall of the Maghlaq Fault, Malta, (ii) determine the porosity reduction from host rock to deformation bands, (iii) quantitatively assess the distribution of pore-sizes within the host rock and deformation bands, (iv) determine which deformation mechanisms dominated during the formation of deformation bands in different stratigraphic units, (v) present a hypothesis on the relative age and evolution history of the studied deformation bands and (vi) investigate the relationship between host rock characteristics and deformation band distribution. Based on these aims, the following objectives have been set for this thesis:

- Map and photograph the entire outcrop using an UAV and produce a high resolution 2D-model of the study area.

- Collect a representative amount of rock samples from the study area, sampling both host rock and deformation bands from all outcropping subunits.

- Analyse the collected samples by the use of a standard optical microscope and a scanning electron microscope to characterise in micro-structural features and lithological compositions.

- Quantitatively assess the degree of pore size reduction from host rock to deformation bands in carbonate grainstones by digitally analysing images acquired from a scanning electron microscope.

1.3 Study Area

The study area is located on the southwestern coast of Malta in the central Mediterranean Sea (see Figure 1.2). The Maltese Islands, consisting of Malta, Gozo and Comino, are located only 90 km south of Sicily, but are considered part of the Pelagian Platform of the African continental plate. Two main fault orientations are observed on the Maltese Islands, the most common being ENE-WSW and the other WNW-ESE (see Figure 1.2a). The only major onshore fault displaying a WNW-ESE orientation is the studied Maghlaq Fault on the southwestern coast of Malta. The Maghlaq Fault is considered to be the northernmost extent of the Pantelleria Rift System, located to the southwest of Malta. Along the southwestern coast, the well exposed Oligocene-Micoene carbonate succession can be studied in detail. The outcrop studied in this project, known locally as Ras il-Bajjada, is located on the hangingwall at the easternmost exposure of the Maghlaq Fault (see Figure 1.2b). Here, well exposed deformation bands are distributed within the Globigerina Limestone Formation.
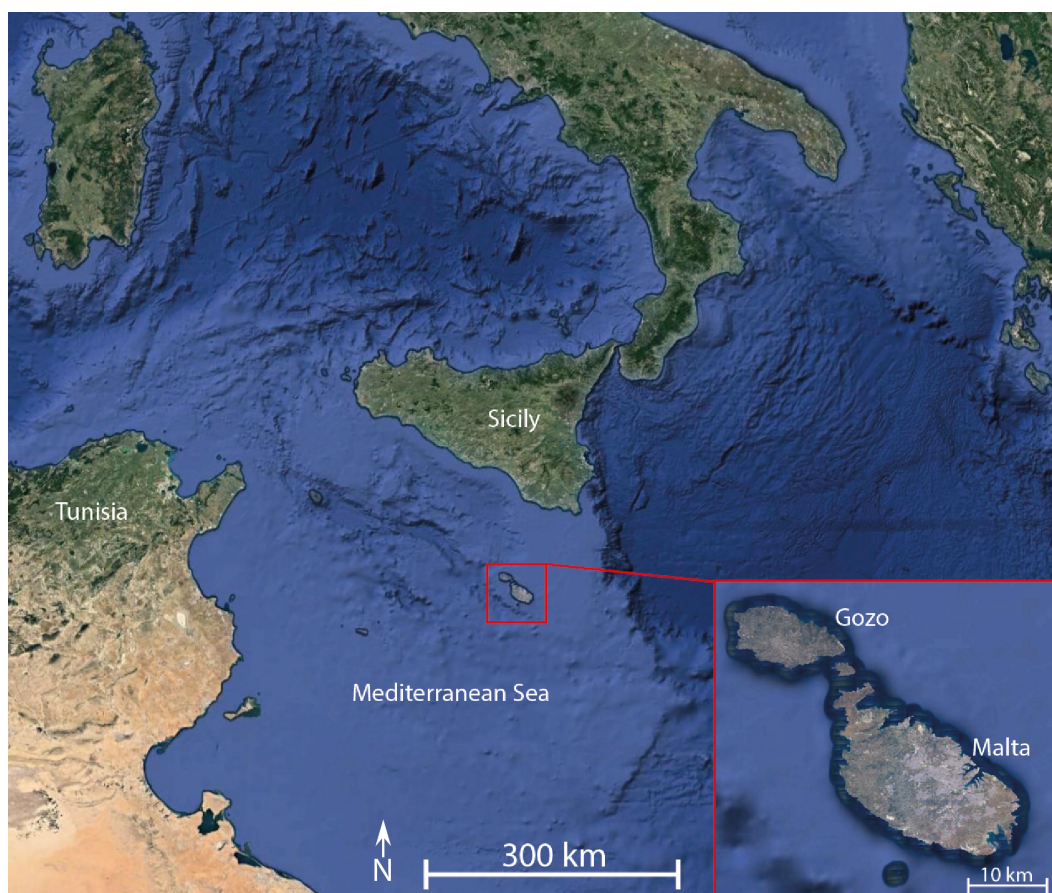
Figure 1.1: Satellite image of the Central Mediterranean, showing the location of the Maltese Islands. Malta is located about 90 km south of Sicily, and 300 km east of Tunisia. Images from Google Earth.
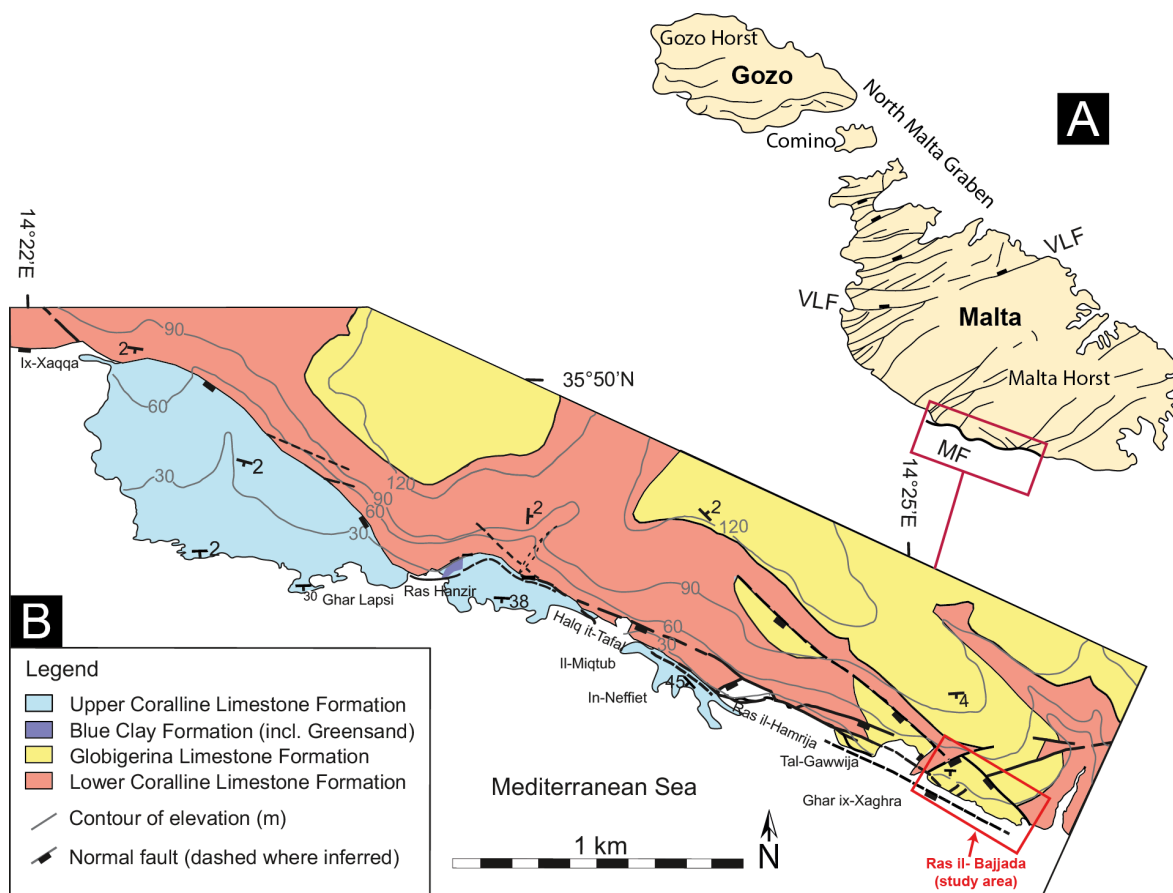
Figure 1.2: (A) A structural overview of the Maltese Islands, Malta, Gozo and Comino. The map shows the main faults on the islands, along with their orientation trends. The majority of faults on the islands show a SW-NE trend, with the largest being the Victoria Lines Fault (VLF) on Malta. The only major onshore fault with a SE-NW trend is the studied Maghlaq Fault, on the southwestern coast of Malta. (B) Geological map of the area along the Maghlaq Fault along the southwestern coast of Malta. The outcropping section of the fault is around 4 km. Modified from Bonson et al. (2007) and Rotevatn et al. (2016b).

Chapter 2

Theoretical background

The focus of this chapter is to explain the theory, concepts and terminology related to the classification and formation of deformation bands in porous rocks. Most of the existing literature considers structures in siliciclastic rocks (Fossen et al. (2017) and references therein), but the concepts are transferable to band formation in carbonates as well. The first part of the chapter will elaborate on the general characteristics of deformation bands, how they are classified and under what conditions they nucleate and grow. The second part describes deformation bands forming in carbonate rocks and how they differ in terms of appearance and formation. Abbreviations introduced in this and following chapters, are listed and explained on page 69.

2.1 Deformation bands

Deformation bands are common structures in porous rocks where applied stress causes zones of strain localization where porosity and permeability is reduced, relative to the host rock. Unlike in non-porous rocks, where deformation often is accommodated by brittle fractures, the presence of pore space in granular rocks promote different deformation mechanisms to alter the grain and porosity distribution. Deformation bands are usually mm-wide, cohesive and display localized shear and/or changes in volume of the deformed rock, but in contrast to fractures they do not develop a continuous slip surface (Aydin, 1978; Fossen and Bale, 2007; Cilona et al., 2012). Deformation bands can occur as single bands, in clusters or in networks of many individual bands (Aydin and Johnson, 1978). Deformation bands in sandstones have been thoroughly researched and documented since the late 1970's while the equivalent structures in carbonate rocks have only recently been studied in detail (Tondi et al., 2006; Rath et al., 2011; Rustichelli et al., 2012; Cilona et al., 2012; Antonellini et al., 2014; Rotevatn et al., 2016b). Deformation bands are considered important to hydrogeologists and petroleum geologists due to their effect on porosity and permeability in rocks, as

fracturing of a porous rock tends to increase its bulk permeability, while the formation of deformation bands reduces it (Gibson, 1998; Fossen et al., 2007; Fossen and Bale, 2007; Rustichelli et al., 2012). Networks of deformation bands can enhance the effect and induce a more tortoise flow pattern, increasing sweep efficiency (Fossen and Bale, 2007; Rotevatn et al., 2009; Fossen and Rotevatn, 2012) or lead to compartmentalization of a reservoir, making parts inaccessible for fluid production (Antonellini et al., 1994; Tondi et al., 2006; Tondi, 2007; Rath et al., 2011). Their small offset renders them unresolvable in most seismic data, but they can nevertheless significantly impact reservoir quality (Fossen and Bale, 2007; Ballas et al., 2015).

2.2 Classification of deformation bands

Deformation bands are generally classified in two different ways: by kinematics and/or by deformation mechanism. Aydin et al. (2006) presents a classification scheme based on the kinematics of strain accommodation in deformation bands (see Figure 2.1). Deformation bands can be created by compaction (volume decrease), dilatation (volume increase) or hybrids of these (compactional shear bands, dilational shear bands, shear enhanced compaction bands and shear-enhanced dilation bands). Compactional shear bands are the most common deformation bands found in the field (Fossen et al., 2007; Rotevatn et al., 2016b). Dilational shear bands are far less common, but have been identified in naturally occurring deformation bands (Du Bernard et al., 2002). Often combined with the kinematic classification scheme, deformation bands can also be classified into different categories based on the main deformation mechanisms involved during their formation (sensu Fossen et al. 2007): 1. Disaggregation bands (granular flow), 2. Phyllosilicate bands (smearing of phyllosilicates between grains), 3. Cataclastic bands (fracturing/crushing of grains; cataclastic flow) and 4. Solution and cementation bands (see Figure. 2.2). These four types of deformation bands will be elaborated on over the following sub-chapters.

2.2.1 Disaggregation bands

Disaggregation bands form when the host rock is subjected to compaction, dilation and/or shear forces causing granular flow, a process which involves sliding, rolling and rotation of grains without fracturing them. Disaggregation bands are usually formed at shallow burial depths (<1 km) in poorly consolidated sandstones (Hesthammer and Fossen, 2001), but have also been documented in carbonate grainstones (Rath et al., 2011). The formation of disaggregation bands is however not limited to shallow burial depths. Fluid overpressure at greater depths will counteract the stress across grain
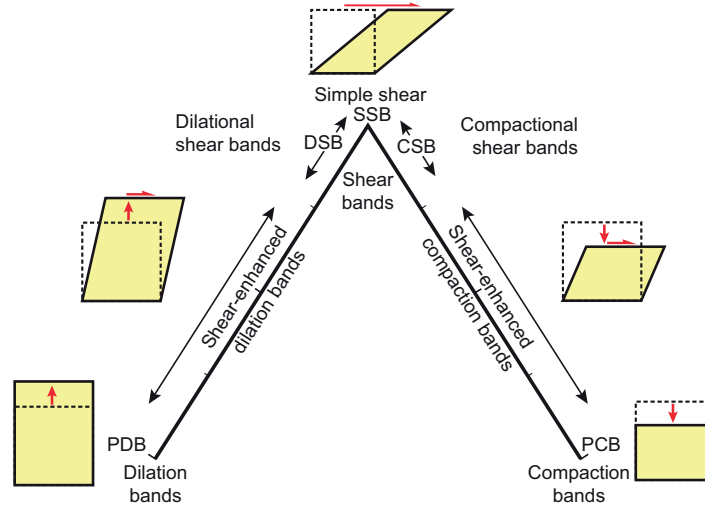
Figure 2.1: Kinematic classigication diagram of deformation bands formed by compaction, simple shear and dilation. PCB: pure compaction band; CSB: compactional shear band; SSB: simple shear band; DSB: dilational shear band; PDB: pure dilation band. Modified from Fossen et al. (2017).

contacts, promoting granular flow as opposed to cataclastic failure (Fossen et al., 2017). Disaggregation bands are commonly not considered significant barriers to fluid flow as they are not associated with significant reduction in porosity or permeability (Knipe et al., 1997). Because the grains are not altered in other ways than their position and orientation, these bands can be hard to identify in homogeneous rocks where the offset is not made clearly visible in layers or lamina of different colour or composition (Fossen et al., 2007). Tondi et al. (2006) documented compactive shear bands in limestones where the dominant deformation mechanisms where like that of disaggregation bands.

2.2.2 Phyllosilicate bands

Phyllosilicate bands, also known as framework phyllosilicates, mainly develop in porous rocks with a clay-, mica- or other platy mineral content above 10-15 % (Fossen et al., 2007). The platy minerals work as a lubricant and enhance grain boundary sliding which increases the sealing effect of the band (Fossen et al., 2007; Hesthammer and Fossen, 2001). Fisher and Knipe (2001) observed permeability reductions across phyllosilicate bands of up to six orders of magnitude. These bands are commonly found in clay- and mica-bearing sandstones that make up several Jurassic reservoirs in the North Sea (Fisher and Knipe, 2001), but as their development requires a phyllosilicate content excluding the rocks studied closely in this thesis, they will not be described further in detail.
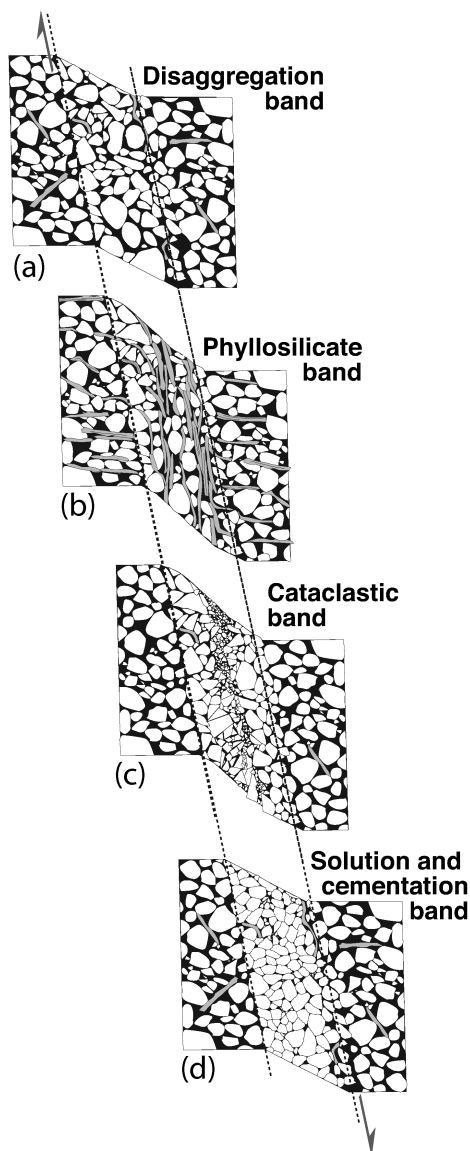
Figure 2.2: Classification of deformation bands based on dominating deformation mechanism. From Fossen et al. (2007).

2.2.3   Cataclastic bands

Cataclastic bands form form as a results of stress concentration at grain contact points, leading to grain fracturing/crushing. Cataclastic bands typically have a central zone with a variety of different grain sizes as well as a high matrix content due to grain-size reduction through fracturing (further enhanced by increased angularity of grains) and a lack of pore space (Aydin, 1978). The area around the central zone, often referred to as the transition zone (Fossen et al., 2007), the boundary zone (Antonellini et al., 1994), or the deformation band outer zone (Aydin, 1978), is characterized by compaction and a lower degree of fracturing. Cataclastic deformation bands are most commonly found in sandstones which have been buried to depths of 1.5 - 2.5 km,

but may also appear in unconsolidated sands (Cashman and Cashman, 2000; Ujiie et al., 2004). Deformation bands displaying cataclasis as a dominating deformation mechanism in carbonate grainstones have been documented by Rotevatn et al. (2016b) and in conjunction with pressure solution by Rath et al. (2011) and Cilona et al. (2012).

2.2.4 Solution and cementation bands

Solution bands in siliciclastic rocks are typically characterized by tightly packed, unfractured quartz grains of a smaller grain size than the matrix (Gibson, 1998; Fossen et al., 2007). The grain boundaries are often serrated or irregular and are commonly separated by a thin lining of dark phyllosilicates (Gibson, 1998). Cementation bands usually develop along with cataclasis or grain boundary sliding when fresh reactive surfaces are revealed. In sandstones where minerals like chlorite or illite coat the grains of the host rock, cementation is enhanced during the formation of cataclastic deformation bands. The coating is fractured during cataclasis and grain boundary sliding, and reactive surfaces of quartz are exposed (Fossen et al., 2007). Pressure solution plays a more prominent role in the development of deformation bands in carbonate rocks, where solution seams within existing compacted deformation bands form at grain contacts (Cilona et al., 2012). It has been suggested that pressure solution may be a more dominant deformation mechanism in contractional regimes (Tondi et al., 2006; Cilona et al., 2012) compared to extensional (Rath et al., 2011; Rotevatn et al., 2016b).

2.3 Sensitivity of deformation band formation to host rock properties

Table 2.1: Factors influencing the degree of cataclasis in deformation bands (Fossen et al., 2017).

Variable	Granular flow	$\rightarrow$	Catalasis
Burial depth (confining stress)	Unconsolidated	$\rightarrow$	Well lithified
Lithification	Shallow	$\rightarrow$	Deep
Fluid overpressure	High	$\rightarrow$	Low
Cement strength	(low) $FeO(OH) \rightarrow$	$CaCO_3$	$\rightarrow SiO_2$ (high)
Grain roundness	Angular	$\rightarrow$	Rounded
Grain sorting	Poor	$\rightarrow$	Good
Grain strength	Strong	$\rightarrow$	Weak
Phyllosilicate content	High	$\rightarrow$	None
Tectonic regime	Extensional	$\rightarrow$	Contractional
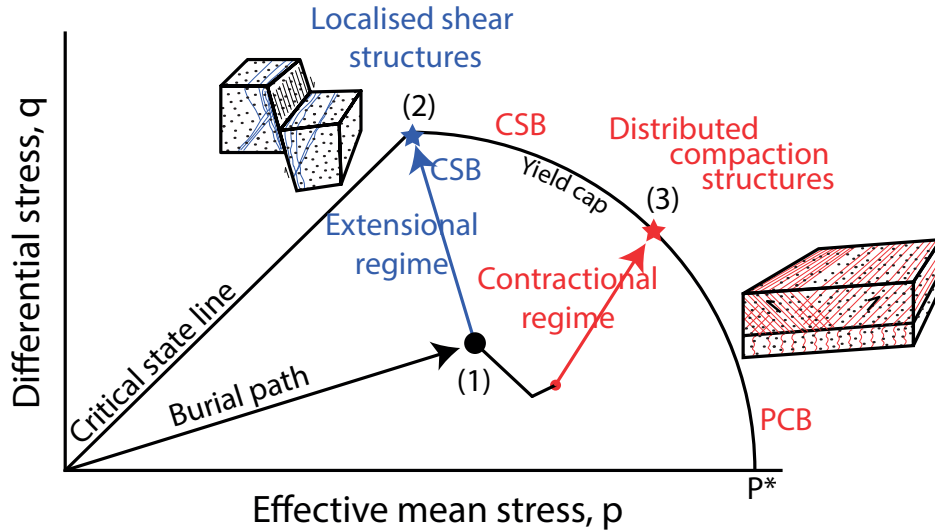
Figure 2.3: A q–p diagram displaying the stress path of a sandstone subjected to burial. (1) The rock is exposed to extension (increased q, reduced p), forming localised compactional shear bands (CSBs) when the stress path hits the yield cap at (2). In an contractional setting (increasing q, increasing p), the stress path intersects the yield cap where distributed shear-enhanced compaction bands (SECBs) or pure compaction bands (PCBs) are expected (3). P*: crushing pressure. Modified from Fossen et al. (2017).

Laboratory experiments and field observations have shown that the deformaion mechanisms producing deformation bands are sensitive to a wide range of host rock properties, as well as depositional and structural conditions (Wong et al.). Of these factors, the most important are burial depth, tectonic stresses and host rock characteristics, listed in Table 2.1). For example, at low overburden stresses, the individual grains in a granular rock experience less stress at contact points with other grains (Fossen et al., 2017). This enables grains to rotate, translate and slide into pore spaces, forming disaggregation bands. Higher stresses however, enhances cataclasis of the grains with fractures initiating at contact points. Significant fluid pressure in the rock will counteract the overburden stresses, enabling the formation on disaggregation bands or even dilational bands at higher depths (Fossen et al., 2017). Looking at the formation of compaction bands, Cheung et al. (2012) observed that well sorted rocks were more prone to cataclasis as fewer contact points between grains increased the relative stress for each point.

Studies have shown that the kinematics and deformation mechanisms observed in deformation bands can deduce the tectonic regime at the time of deformation (Soliva et al., 2013). Figure 2.3 shows the stress path of a porous sandstone subjected to stresses in an (1) extentional and (2) contractional regime. Plastic deformation occurs as the path crosses the yield envelope, or cap (Schultz and Siddharthan, 2005). Deformation bands where the compaction component of the displacement is greater than or equal to the shear component, will develop in a contractional regime where the confin-

ing pressure, p, is high relative to the differential stress, q (Fossen et al., 2017). This situation arises as contractional regimes are associated with added horizontal stress, in contrast to extentional regimes where the horizontal stress component is reduced and leads to a higher differential stress. Pure compaction bands (PCB) can, in contrast to what is displayed in 2.3, develop in extensional regimes as bed-parallel bands formed by the increased differential stress of vertical sediment loading during burial (Tondi et al., 2006; Rustichelli et al., 2012; Rotevatn et al., 2016b).

2.4   Effect on fluid flow

Several studies have investigated the effect of deformation bands on fluid flow (Sternlof et al., 2006; Fossen and Bale, 2007; Rotevatn et al., 2009; Fossen and Rotevatn, 2012). Although deformation bands show a porosity reduction of over one order of magnitude and a permeability reduction of up to six orders of magnitude (Antonellini et al., 1994; Fisher and Knipe, 2001; Rath et al., 2011; Ballas et al., 2015), it is their distribution, orientation and frequency that ultimately determines whether they prove to be advantageous or disadvantageous in a production scenario (Fossen et al., 2017). In a layered siliciclastic reservoir, the development of deformation bands favours stratigraphic units with the highest porosity, and by extension the highest permeability (Fossen and Rotevatn, 2012). A bulk reduction in porosity and permeability in the most permeable layer would force reservoir fluids to flow in a more tortuous manner, potentially leading to an improved sweep of the reservoir (Rotevatn and Fossen, 2011). Lateral differences in thickness, permeability and porosity greatly affects the sealing capability of both single and clusters of deformation bands (Torabi and Fossen, 2009). Torabi et al. (2013) concluded that in sandstones, only continuous slip surfaces with thick surrounding clusters of cataclastic bands would have the required sealing potential for significant hydrocarbon traps. Cataclasis of carbonate grains however, can start at shallow burial depths compared to feldspar and quartz grains in sandstones. This makes deformation bands in carbonates more likely to impact the reservoir properties (porosity and permeability) of a rock even at shallow burial depths (Fossen et al., 2017).

2.5   Deformation bands in carbonate rocks

Although the amount of field work carried out on deformation bands in sandstones outweigh that on carbonates, a range of different naturally occurring bands have been documented in recent year (Tondi et al., 2006; Rath et al., 2011; Rustichelli et al., 2012; Cilona et al., 2012; Rotevatn et al., 2016a). So far, deformation bands in carbonate rocks have primarily been documented in high-porosity grainstones made up of bio-

clastic fragments or sparite ooids (Tondi et al., 2006; Rath et al., 2011; Cilona et al., 2012), but they have also been described in chalks (Wennberg et al., 2013) and low-porosity (primary) platform limestones (Antonellini et al., 2014). Several studies have also investigated the deformation of carbonate rocks through laboratory experiments to determine the inelastic behaviour and failure mechanisms involved in deformation band formation (Vajdova et al., 2004; Baud et al., 2009; Zhu et al., 2010; Cilona et al., 2012; Vajdova et al., 2012). It is important to distinguish between naturally occurring and laboratory made deformation bands when looking at carbonate rocks as most of the experimental studies have been carried out on dry rocks, whereas the natural formation of deformation bands likely involves fluids (Cilona et al., 2012).

Of the four main deformation mechanisms involved in deformation band formation listed in section 2.2, three have been documented in deformation bands occurring in carbonate rocks: (1) granular flow, (2) cataclasis and (3) pressure solution. Pressure solution in carbonates plays a more prominent role in the further development of deformation bands beyond the initial formation, compared to siliciclastic rocks (Tondi et al., 2006). Pressure solution within already compacted bands, together with the development of Hertzian cracks at grain contacts, is one of the main contributors to grain size reduction and further evolution of naturally occurring bands without considerable cataclasis (Cilona et al., 2012). The grain or bioclast assemblage of the rock may also affect the degree of pressure solution in grainstones. Rustichelli et al. (2012) found that pressure solution seams localized at the contact points of bioclasts lacking internal porosity, mainly echinoderms and red algae. Although a common factor in the further development of deformation bands in carbonates, pressure solution is not an imperative component. Rath et al. (2011) investigated the effect of cementation during the development of deformation bands in high porosity carbonate grainstones. They discovered that two different deformation mechanisms dominated before and after precipitation of blocky cement; grain compaction, translation and rotation for the first generation and cataclasis for the second. Higher yield strength of the rock as a result of cement precipitation along the grains caused the bioclasts and cement to deform by cataclasis.

Carbonate grains are weaker than the primary constituents of siliciclastic rocks, feldspar and quartz, which enables cataclasis in unconsolidated carbonates to occur at shallower burial depths than in sandstones (Fossen et al., 2017). Through comparing naturally occurring compactive shear bands to laboratory induced ones, Cilona et al. (2012) was able to determine that the bands in their bioclastic Majella grainstone (similar to Tondi et al. (2006)) had formed under pressure conditions of below 10 MPa. There have been several studies aimed at understanding how porous carbonate rocks deform at different confining pressures (Vajdova et al., 2004; Baud et al., 2009;

Zhu et al., 2010). Baud et al. (2009) observed that compactive shear bands developed through granular flow and pore collapse at low confining pressures, but that cataclasis impedes and surpasses compaction localization as the dominant deformation mechanism at high pressures. In carbonate rocks, compressibility and porosity are positively correlated. Laboratory experiments show that the critical stress from hypostatic loading which causes pore collapse, is reduced with increasing porosity of the host rock (Vajdova et al., 2004).

Chapter 3

Methods

This chapter will focus on the different methods and techniques used during field work and subsequent data analysis. The first part of the chapter will describe the data acquisition done in the field, while the second part focuses more on specific instruments and workflow connected to digital image analysis and the methods used to conduct quantitative analyses on acquired datasets.

3.1 Field work

Field work associated with this thesis was carried out over 9 days on Malta during October of 2017. As previous studies have collected extensive structural and sedimentological information from the outcrop, the primary objective of this field work was to build upon the existing data using new methods. Collecting samples of deformation bands and host rock for thin sections studies while documenting their structural and stratigraphic context was also an essential part of the field work.

3.1.1 Outcrop mapping

The resolution of available satellite images from the outcrop is not sufficient to allow detailed structural or stratigraphic mapping on them. To further develop the existing stratigraphic and structural interpretations on the outcrop, even after the return from Malta, high resolution images of the entire outcrop was collected using an unmanned aerial vehicle (UAV). The UAV used was a DJI Phantom 4 Pro, equipped with a 20 megapixel camera able to collect images both above and oblique to the surface. A high resolution 2D-model compatible with ArcMap was produced from the UAV-captured images. Detailed descriptions of structural elements within the study area was carried out to complement the collected UAV-images. Deformation bands appearing on the outcrop were described with regards to the stratigrahpic unit they occurred in, band

orientation and relation to nearby structures. The displacement and orientation of faults in the study area was also documented.

3.1.2 Sedimentological logging

The stratigraphy of the study area had already been logged and described in detail by previous studies, but with the help of local sedimentologist Peter Gatt (University of Malta), adjustments to previous interpretations have been made. The units outcropping within the study area were classified according to the classification schemes for carbonate rocks after Dunham (1962) and Folk (1959). The scheme proposed by Dunham (1962) (3.1) classifies the rock according to mud content and depositional textures. The classification scheme by Folk (1959) differentiates between the matrix composition and bioclasts present in the rock. Detailed photographs with a mm-scaled resolution were taken using a digital single-lens reflex camera. Scanlines running perpendicular to the coastline were studied to document how deformation band distribution was affected by changes in lithology.
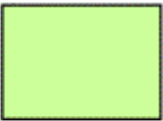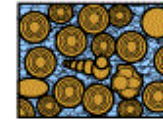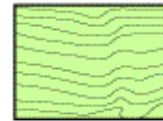
Figure 3.1: Dunham classification scheme for limestones, subdividing on the basis of mud-content and depositional textures. Modified by C. Kendall from Dunham (1962)

3.2 Microscopic analysis

The samples collected during field work on Malta were sent to the Independent Petrographic Services Ltd in Aberdeen for thin section preparation. The samples were impregnated with blue epoxy before being polished using aluminium oxide to a thickness

of around 30 µm. The use of dyed epoxy allows pores and cavities to be easily recognised in optical microscopic analysis and makes digital measurements of 2D-porosity possible through color-filtering. Samples of host rock and deformation bands (where present) from all outcropping units in the study area were studied both in an optical polarizing light microscope and a scanning electron microscope (SEM). Combining observations and measurements from these fundamentally different microscopes allowed for detailed analysis not applicable to data from either one.

3.2.1 Light microscopy

A Nikon Eclipse LV100POL standard polarizing light microscope was used to study the thin sections. A mounted digital Nikon-camera allowed for photomicrographs to be captured at the three magnifications available through different lenses (4X, 10X, 40X). Photomicrographs of thin section slides through an optical microscope provide information related to the overall composition of the rock, as well as the amount of macro-porosity present. Most of the photomicrographs presented as a part of this study was taken at a 4X-magnification, with a resolution allowing for the detection of grains with a diameter of >2 µm. However, due to the thin section thickness of 30 µm, significant uncertainties apply to the assessment of grains below this size (see Section 3.4). To closely study microprocesses like pressure solution and microfractures, or to investigate cements and microporosity, a microscope with significantly higher resolution is neeeded.

3.2.2 Scanning Electron Microscopy

A scanning electron microscope provides the high resolution and high magnification images needed for detailed microanalysis. The available SEM at UiB is a ZEISS Supra 55VP Field Emission Scanning Microscope (Figure 3.2) with a potential resolution of 0.8 nm and capable of a magnification above $1\,000\,000\,000$ X. A sketch of a SEM, showing the components and basic functions is shown in Figure (3.3). An electron gun (cathode) generates a high-energy beam (15 keV) of electrons which is directed towards the sample through an anode. The electron beam passes through an electromagnetic condenser lens, which focuses the beam on the sample surface. The primary electrons generated by the gun hit the sample material, causing secondary electrons to be emitted into the vacuum-filled chamber. These secondary electrons, known as backscatter secondary electrons (BSE), are in return absorbed by a detector which digitally interprets and processes the signal into an image displayed on the monitor. In the case of this study, a backscatter electron detector, or BSD, is used to capture the secondary electrons. The yield of these electron scales with atomic number, result-

ing in the grayscale contrasts seen between grains or particles of different compositions (Chen et al., 2015). The combined use of the SEM and BSD is shortened to BSE-SEM. Another detector, called the electron dispersive spectroscopy detector (EDS), allows for the element composition analysis of selected points on the sample. The detector captures emitted x-rays from the sample and identifies the element present based on the energy-level of the emitted photon.

To enhance the amount of reflected secondary electrons, a thin layer of a conductive coating is applied to the sample surface before analysis. Both carbon and gold coating was applied to the studied thin sections, but gold coating provided the best image in SEM. When only applying carbon coating, images were often distorted due to a "specimen charging effect" (Seeger et al., 2006). This effect is caused by rapid charge build-up from high energy electrons hitting the sample material (Sim et al., 2010). In SEM-BSE images this can be observed as bright white spots or horizontal lines.

Figure 3.2: Supra 55VP Field Emission Scanning Electron Microscope used for thin section analysis. (Photo: Courtesy of Irene Heggstad, UiB)

3.3   Digital Image analysis (DIA)

Image-based analysis of the collected sample material is an effective method to characterize both the host rock composition and the deformation band properties. Total optical porosity (TOP) or 2D macroporosity, can be determined through digital image
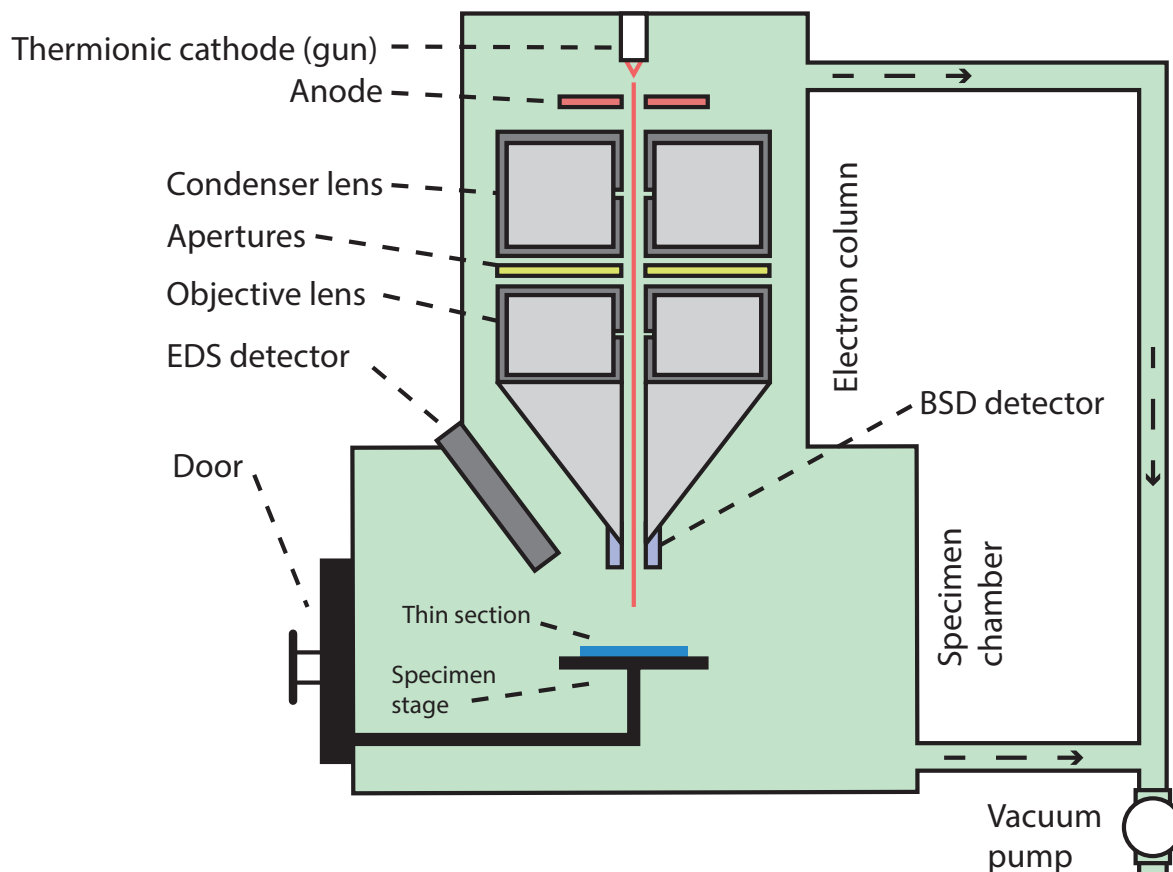
Figure 3.3: Schematic displaying the main components in the scanning electron microscope (SEM) used. An electron gun at the top of the electron column generates a high energy beam of electrons which passes through a number of lenses and apertures before hitting the sample in the specimen chamber. The backscatter secondary electron detector (BSD) absorbs electrons emitted from the sample, which in turn is digitally converted into a grayscale image. The electron dispersive spectroscopy detector (EDS) interprets x-rays emitted from the sample to determine the element composition of specific points. Figure modified after Northern Arizona University (2008)

analysis (DIA) on photomicrographs whilst the high resolution of BSE-SEM images allows for detection of both 2D macro- and microporosity through DIA (Anselmetti et al., 1998). The open source software ImageJ 1.50i (Schneider et al., 2012) was used for all measurements conducted through DIA in this work.

3.3.1 DIA of photomicrographs

The photomicrographs taken through the polarizing microscope are stored as RGB (Red, Green, Blue), 24-bit images. As the thin sections have been impregnated with blue epoxy, DIA can be used to extract the pore space area of an image by counting blue pixels as shown in Figure 3.4. To make sure only pore space is counted by the software, an interval between 0-255 for hue, saturation and brightness have to be manually set. Small differences in colour and brightness between images means the intervals
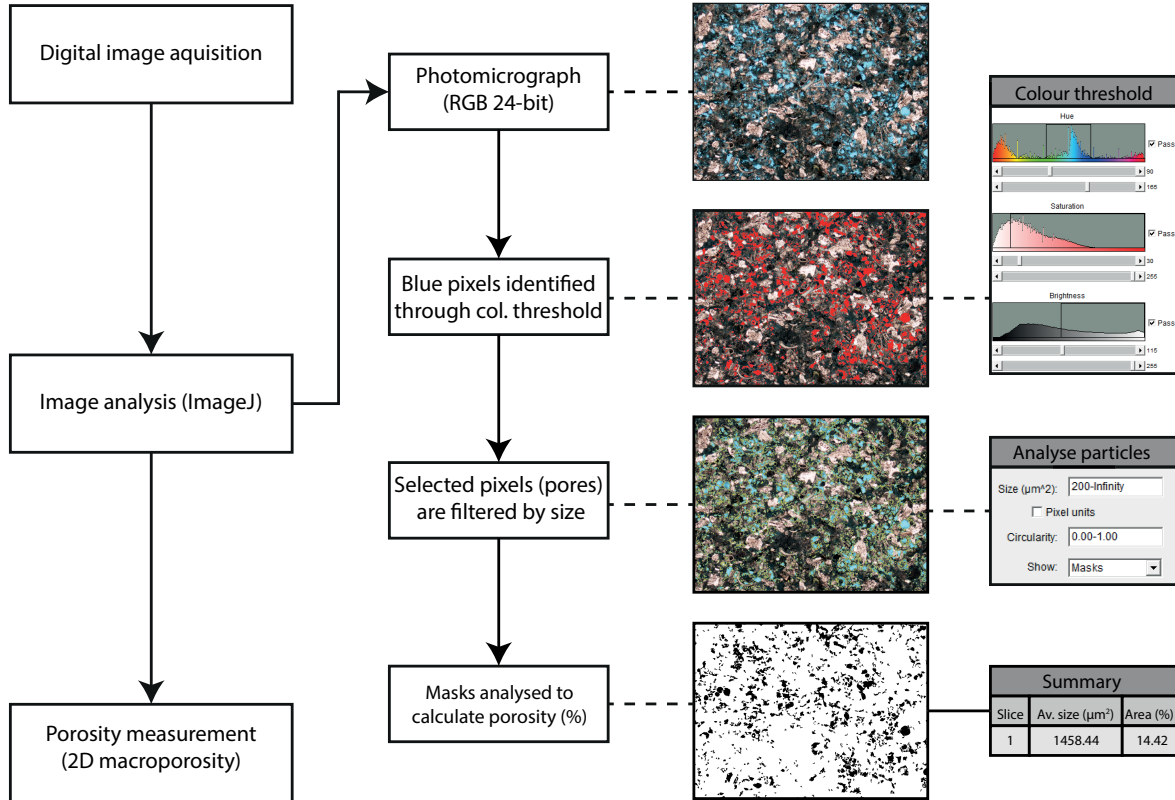
Figure 3.4: Flowchart depicting 2D porosity estimation from thin section photomicrographs (RGB) using ImageJ. By adjusting the colour threshold, pixels coloured by the blue epoxy are counted by the software. A lower threshold for pore size is set to $200\,\mu m^2$ to ensure only macroporosity is calculated.

may have to be altered slightly for each measurement. The colour threshold image is continuously compared to the original, so that only pores are included in the parameters. A lower threshold for the measured macroporosity on the photomicrographs was set at $200\,\mu m^2$, to comply with the resolution of the optical microscope $(10\,\mu m)$ and geological definitions of microporosity $(500\,\mu m^2$ (Anselmetti et al., 1998)). A binary image is produced where dark pixels represent the macropores. Pixels are then counted by the software, calculating an estimate of the 2D macroporosity.

3.3.2 DIA of BSE-SEM images

The digital images generated by the BSE-SEM are stored as 8-bit grayscale images, with compositional differences in the sample seen as variations of 256 shades of gray. The process to isolate and count pore spaces is described in the flowchart seen in Figure 3.5. All pixels of a single shade or within a manually set interval can be selected and counted using ImageJ. For porosity measurements, the darkest shades are selected. Comparisons between the threshold image and the original is done continuously to ensure accurate estimates. Measurments of pore space, bioclasts or quartz grains can
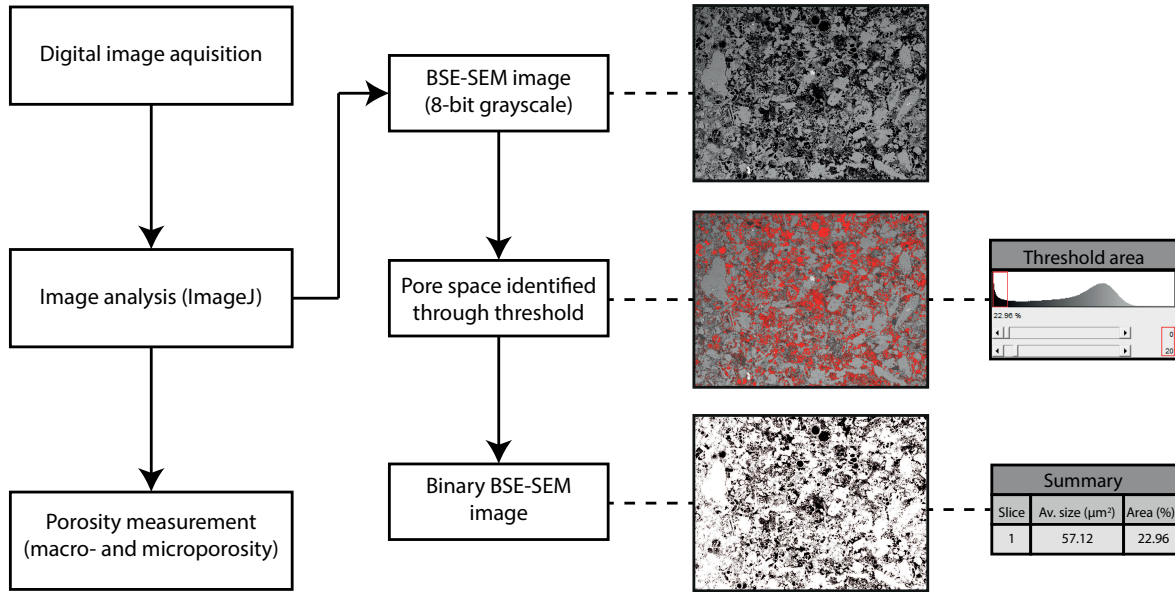
Figure 3.5: Flowchart depicting 2D porosity estimation from 8-bit grayscale BSE-SEM images using ImageJ. The pore space appears as black or dark in the BSE-SEM images. The method shown can be used to calculate the total 2D porosity in an image, including both macro- and microporosity. Modified from Thorsheim (2015).

all be done using this principle. Compared to photomicrographs, the BSE-SEM images show distinct grain boundaries and significant contrast between particles and pore space. This reduces the degree of interpretation needed to manually set the threshold, leading to more accurate measurements and better quantitative data.

Quantitative analysis on BSE-SEM images

In conjunction with porosity measurements carried out on the analysed BSE-SEM images, properties like size and perimeter of each measured pore was also collected. These datasets were used to investigate host rock properties and compositional differences between units and samples from the outcrop, especially related to the distribution of pore quantities and sizes. To present similarly acquired datasets, albeit particle size distributions, Torabi et al. (2007) and Torabi and Fossen (2009) used Exceedance Frequency (EF) plotted against the measured variable. EF is as a unitless factor, which for a specific measurement variable is defined as the relative amount of greater measurements. In a dataset consisting of 4 measurements (1,2,3,4), the exceedance frequency of 3 is 1, as only one measurement is larger than 3. This statistical method, in combination with cumulative plots of the porosity contribution of pore sizes, was used to display the pore size distribution of the collected samples (see Results). Pore size distributions in grainstones were also presented using similar statistical analysis methods by (Cilona et al., 2012).

3.4   Sources of errors

Photomicrograps aqcuired from optical microscopes have well known limitations related to the fact that they are 2D projections of a 3D sample (thin sections have a thickness of 30 µm). This can lead to misrepresentation of clast- and pore sizes within the thin section based on their geometric distribution. Whether clasts are situated at the thin section top or bottom is considered random, so the over- or underrepresentation of clasts or pores from geometrical distributions can be neglected as long as optical parameters during acquisition remain consistent. The problem of clast- and pore distributions is not transferable to BSE-SEM images. Here, only the top µm of the sample is penetrated by the electron beam (Kanaya and Okayama, 1972), giving an accurate representation of the grain- and pore distributions at that slice. When collecting BSE-SEM images it is necessary to adjust the magnification to allow detection of micropores, while also making sure that the captured area is representative of the sample. The resolution of the BSE-SEM images used for porosity estimates is just below 1 µm, excluding detection of the smallest pores in the samples.

Chapter 4

Geological background

4.1 Regional tectonic setting

4.1.1 Tectonic evolution of the Mediterranean

The Mediterranean has had a complex tectonic evolution dominated by both orogenic and extensional processes related to the Meso-Cenozoic convergence of Africa and Eurasia (Dewey et al., 1989; Argnani, 1990; Rosenbaum et al., 2002). Based on the tectonic history, the Mediterranean can be split into a western and an eastern basin. Oligocene and Miocene extensional deformation and syn-rift deposits found in the western Mediterranean are not characteristic of the more geologically stable eastern basins where preserved Mesozoic oceanic crust is believed to underlie sediments (Figure 4.1)(Rosenbaum et al., 2002). The extension in the west, initiated during the Oligocene, was primarily caused by eastward subduction rollback of the subsiding oceanic lithosphere (Lonergan and White, 1997; Gueguen et al., 1998). The convergence rate between the African and Eurasian plates was relatively low compared to the rollback, which led to extension of the overriding plate (Royden, 1993). The geology of the central Mediterranean, the Tyrrhenian Sea and Pelagian Platform, has a similar tectonic characteristics as in the west, with basin formation in the foreland associated with the Apennine-Maghrebian shortening (Argnani, 1990). Basin formation and rifting of the Pelagian Platform, as a response to the Apennine-Maghrebian shortening, is what initiated the development of the Pantelleria Rift System during Plio-Quaternary times (Argnani, 1990).
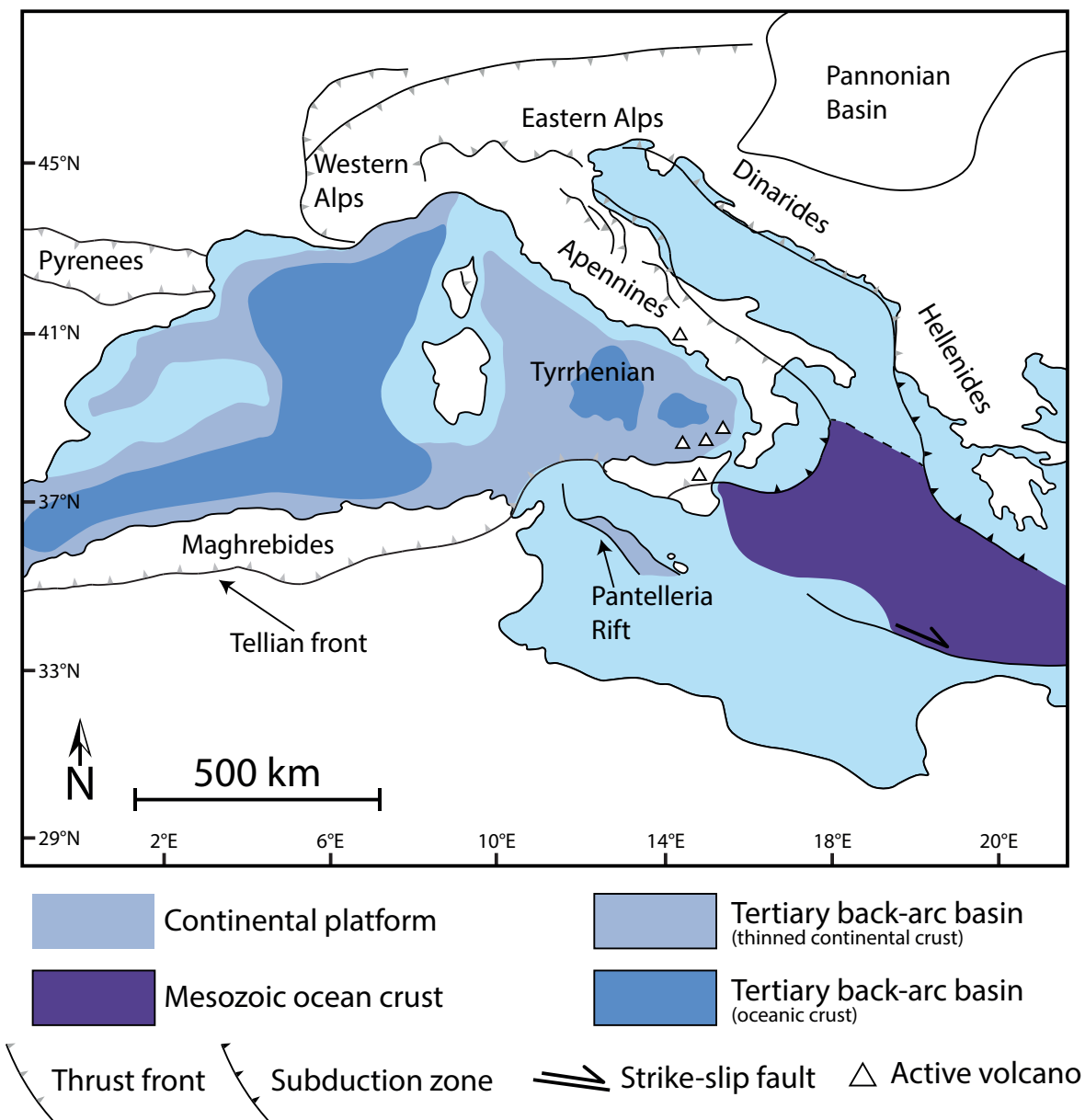
Figure 4.1: Tectonic setting of the western Mediterranean basins and the Alpine orogen (only Mediterranean marine basins are coloured). Ca = Calabria; Co = Corsica; GK = Grand Kabylie; PK = Petite Kabylie; Sa = Sardinia; Si = Sicily. Modified from Rosenbaum et al. (2002).

4.1.2   The Pantelleria Rift System

The Maltese Islands of Malta, Gozo and Comino are located on the NE flank of the Pantelleria Rift system on the Pelagian platform, about 90 km south of Sicily in the western part of the central Mediterranean (Figure 4.2). The Pelagian Platform is part of the African continental plate and stretches from Tunisia and north-western Libya to the Hyblean platform of south-eastern Sicily. The ESE-WNW striking Pantelleria Rift is a trough developed on the Pelagian Platform within the foreland of the Sicilian

Apennine-Maghrebian thrust and fold belt (Bonson et al., 2007). The rift system
contains three elongate and deep troughs (Pantelleria, Linosa and Malta Troughs),
which in some locations accommodate up to 2 km of Plio-Quaternary deposits whilst
maintaining water depths of over 1.7 km (Jongsma et al., 1985). The Pantelleria
Trough is separated from the Malta and Linosa troughs by a N-S-trending belt of
localized basins, uplifts and alkaline volcanic centres which has acted as a transfer
fault-zone between the different parts of the rift system (Argnani, 1990; Dart et al.,
1993). Most of the rifting took place during Plio-Quaternery times while sedimentation
rates dropped relative to displacement in the central basin (Dart et al., 1993). The
Maltese archipelago emerged during early Messinian times due falling sea-level and
uplift of the northern rift flank from the Miocene and onwards (Bonson et al., 2007).
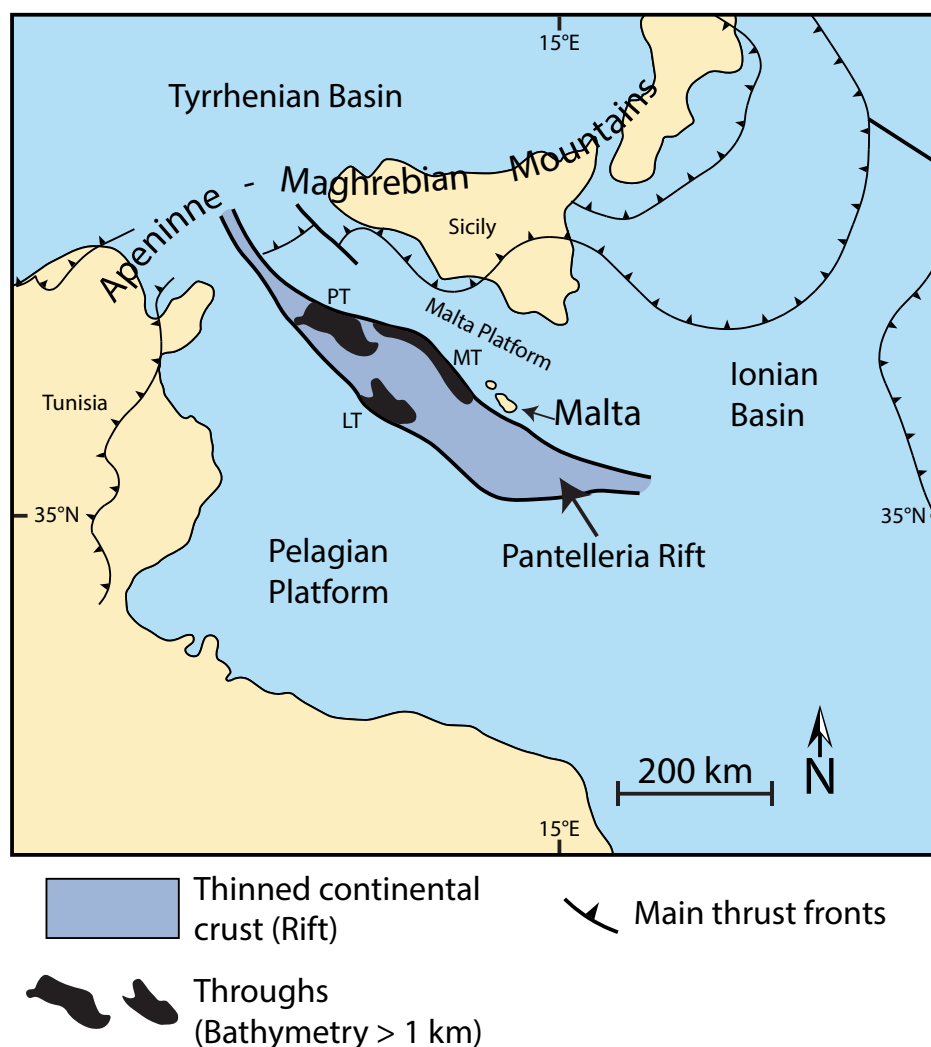
Figure 4.2: Map of the central Mediterranean region showing the location of the Maltese
archipelago with respect to the Pantelleria Rift and Maghrebian-Apennine thrust and fold
belt. Modified from Dart et al. (1993) and Bonson et al. (2007)
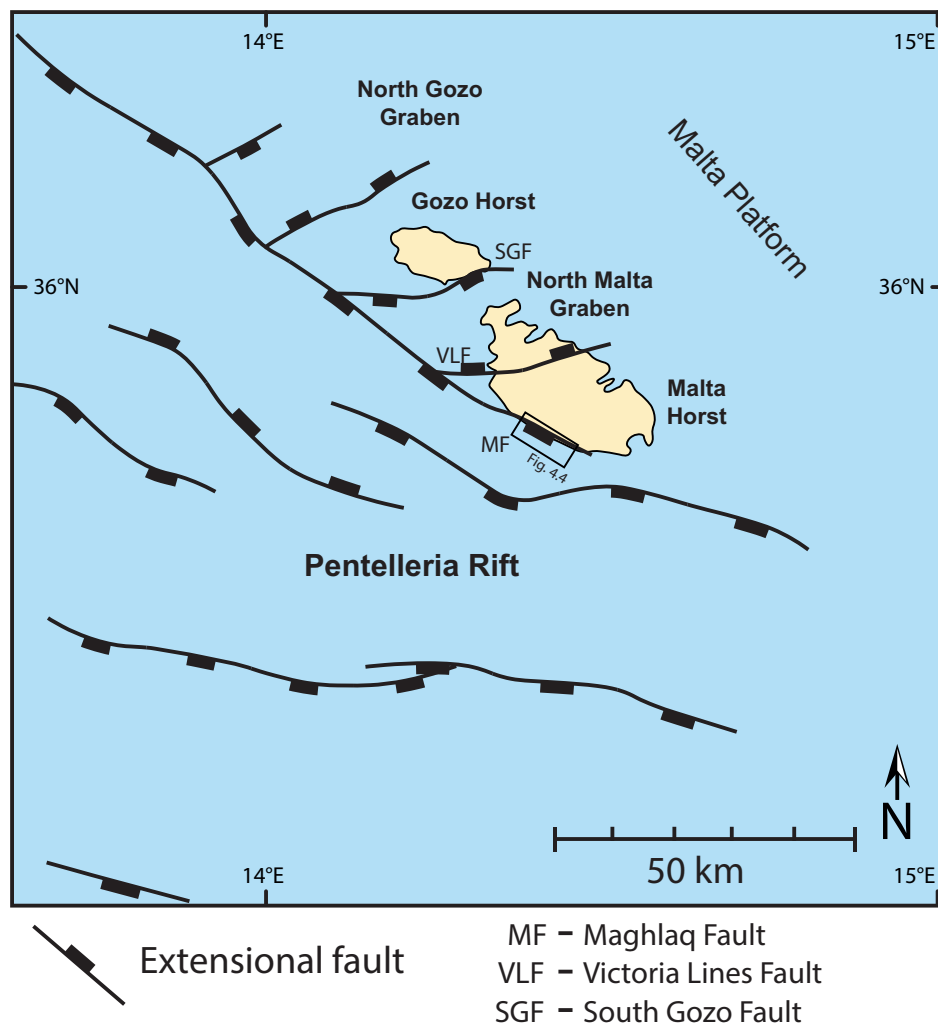
Figure 4.3: Principal structures of the Maltese graben System. SGF, South Gozo fault; VLF, Victoria Lines fault; IMF, Il Maghlaq fault. Modified from Dart et al. (1993).

4.1.3 The Maltese graben system

The Maltese Graben system consists of numerous Miocene-Pliocene extensional basins in the Pantelleria Rift on the Pelagian Platform. The emergence of the Maltese archipelago coincided with the Messinian salinity crisis in the Mediterranean and up-lift of the Pantelleria rifts northern flank. The Maltese graben system is comprised of five major structural units (Figure 4.3); the Gozo and Malta Horsts, North Gozo Graben (NGG), North Malta Graben (NMG) and the Maghlaq fault (Dart et al., 1993). Two intersecting extensional fault trends have been identified within the graben system; ESE-WNW and ENE-WSW. Although the latter trend dominates throughout the archipelago, the largest studied fault on Malta (throw >210m) is the ESE-WNW trending Maghlaq fault (Bonson et al., 2007). Both the North Gozo and North Malta grabens are about 14 km wide, but the former is considerably deeper than the other. Both grabens are confined by faults, where the largest fault throw in the NGG is 1600

m whilst the largest fault in the NMG, the Victoria Lines fault, has a displacement of 195 m (Dart et al., 1993). According to Bonson et al. (2007), the two fault trends developed from the early Miocene (<21 Ma) to present day and were both developed in response to N-S stretching of the Apennine-Maghrebian foreland (Argnani, 1990; Dart et al., 1993).

4.1.4 The Maghlaq fault zone

The Maghlaq Fault (MF) is located on the SW coast of Malta (see Figure 4.4) and is the only major fault on the island with the WNW-ESE, Pantelleria Rift orientation (Pedley et al., 1976). It is characterized by Bonson et al. (2007) as a left-stepping, normal, en échelon fault with a displacement of at least 210 m. The fault is comprised of several segments of 1-2 km in length with an ESE-WNW trend and a dip of 60°-75°towards SSW. The segments are separated by near orthogonal, shorter (50-400 m) fault segments that strike E-W or ENE-WSW. The Maghlaq Fault zone is composed of a 5-40 m wide zone of considerably deformed rocks separated by a set of large slip zones from the less deformed rocks of the hanging- and footwall. On the footwall slip surface, kinematic indicators like movement striations confirm a normal displacement with a minor sinistral component (Bonson et al., 2007).
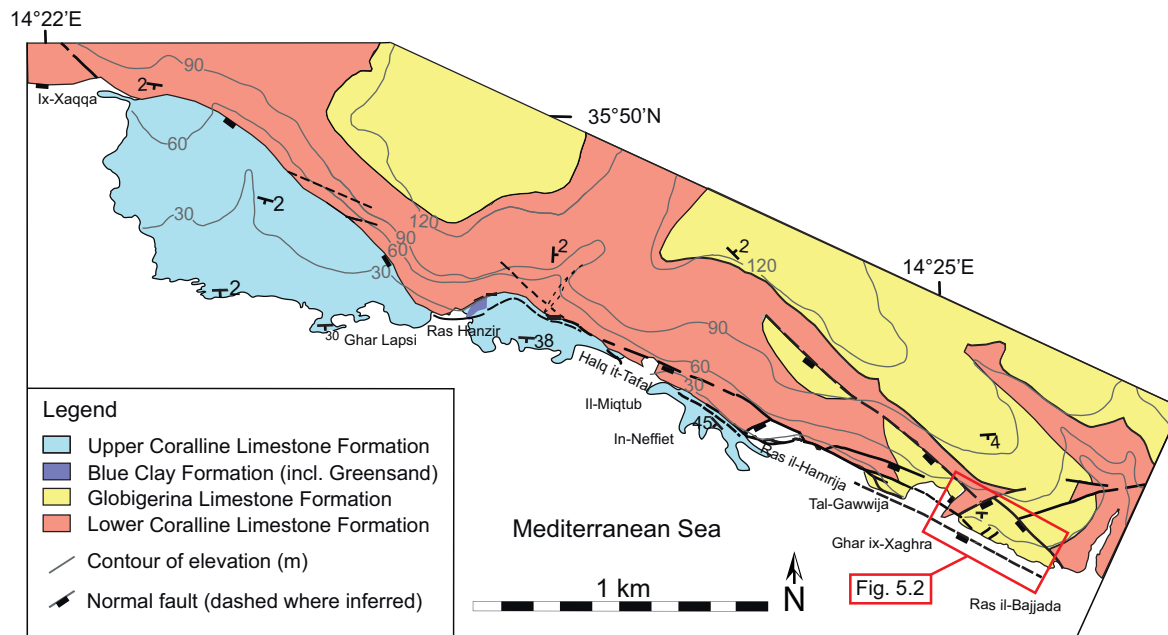
Figure 4.4: Geological map of the area along the Maghlaq Fault along the southwestern coast of Malta. The outcropping section of the fault is around 4 km. Modified from Bonson et al. (2007) and Rotevatn et al. (2016b).

4.2   Regional stratigraphic setting
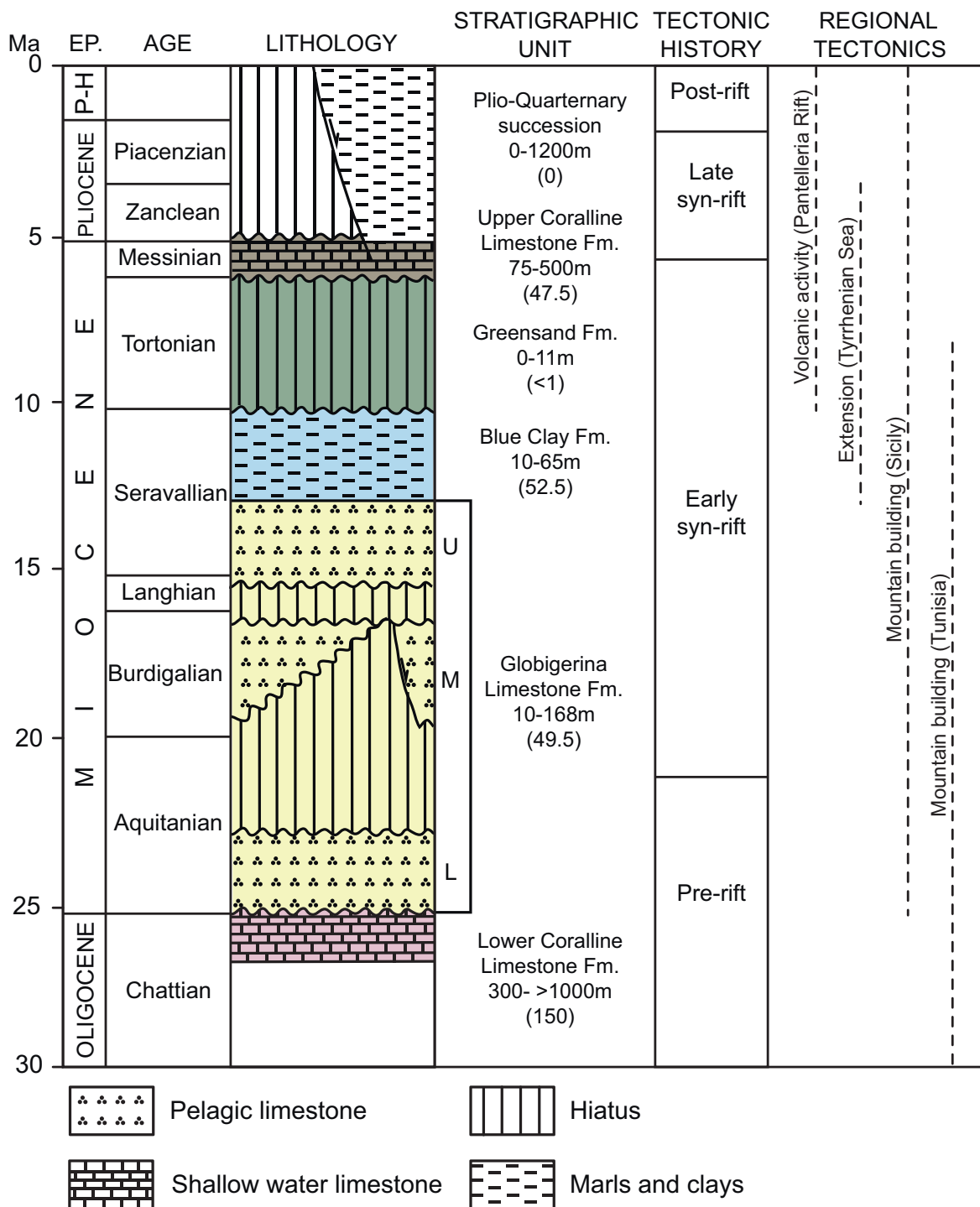
Figure 4.5: Tectono-stratigraphic log of the Oligocene-Quaternary age sediments of the Maltese archipelago. Unit thickness values in parentheses represent thickness along the Maghlaq Fault, as estimated by Bonson et al. (2007). Modified from Dart et al. (1993) and Bonson et al. (2007).

The stratigraphy of the Maltese archipelago is dominated by shallow marine carbonate deposits of Oligocene to late Miocene age (see Figure 4.5). The well-studied and

exposed carbonate succession is comprised of five formations seen in Figure 4.6; the Lower Coralline Limestone Fm. (LCLF), the Globigerina Limestone Fm. (GLF), Blue Clay Fm. (BCF), Greensand Fm. (GSF) and the Upper Coralline Limestone Fm. (UCLF) (Pedley et al., 1976; Dart et al., 1993). The succession can be subdivided with respect to the rifting phase at the time of deposition; pre-rift, early syn-rift, late syn-rift and post-rift. Discontinuous Quaternary deposits of fluvial gravels, paleosoils and cave infills are also present on the islands, but are of limited extent (Illies, 1981). The characteristics of the five outcropping formations are described in further detail below.

4.2.1   Pre-rift

Lower Coralline Limestone Formation

The Lower Coralline Limestone Formation is the oldest formation visible in outcrops on the Maltese islands. Only the top 140 m are exposed, but wells drilled in the area indicate a maximum thickness of at least 300 m (Jongsma et al., 1985; Dart et al., 1993). The oldest exposed layers consist of massive yellow biomicrites with a high content of benthic foraminifera. These beds are conformably overlain by bedded, pale-grey coralline algal limestones dominated by red algae (Pedley et al., 1976). The uppermost 10 m of the formation indicate a shift from rhodolitic favouring conditions and are characterized by coarse, cross-bedded bioclastic limestones dominated by echinoid fossils. The depositional environment of the Lower Coralline Limestone Formation has been interpreted to initially being a shallow gulf-type area (Felix, 1973). Towards the end of the Oligocene this environment became increasingly open marine, as indicated by the deposition of rhodolitic algae (Pedley et al., 1976). A shallow marine shoal environment concluded the Chattian over the archipelago, apart from south-eastern Malta where a protected environment allowed deposition in calmer and deeper waters.

Lower Globigerina Limestone Member

The early Aquitanian Lower Globigerina Limestone Member (LGLM) is named after its high content of the planktonic Globigerina foraminifera (Pedley et al., 1976). The member is comprised of massive bedded, pale-yellow biomicritic wackestones (Dart et al., 1993) or biomicrites (Pedley et al., 1976) and the formation thickness varies from 100 m in the Valletta Basin of Malta to only 40 m on Gozo (Dart et al., 1993). The upper limit of the member is characterized by a thin, phosphorite conglomerate bed overlaying a hardground recognised throughout the Maltese archipelago (Gruszczyński et al., 2008). Phosphorite beds have been attributed to depositional hiati, seafloot lithification and the development of hardgrounds on carbonate shelf environments (Pedley

and Bennett, 1985).
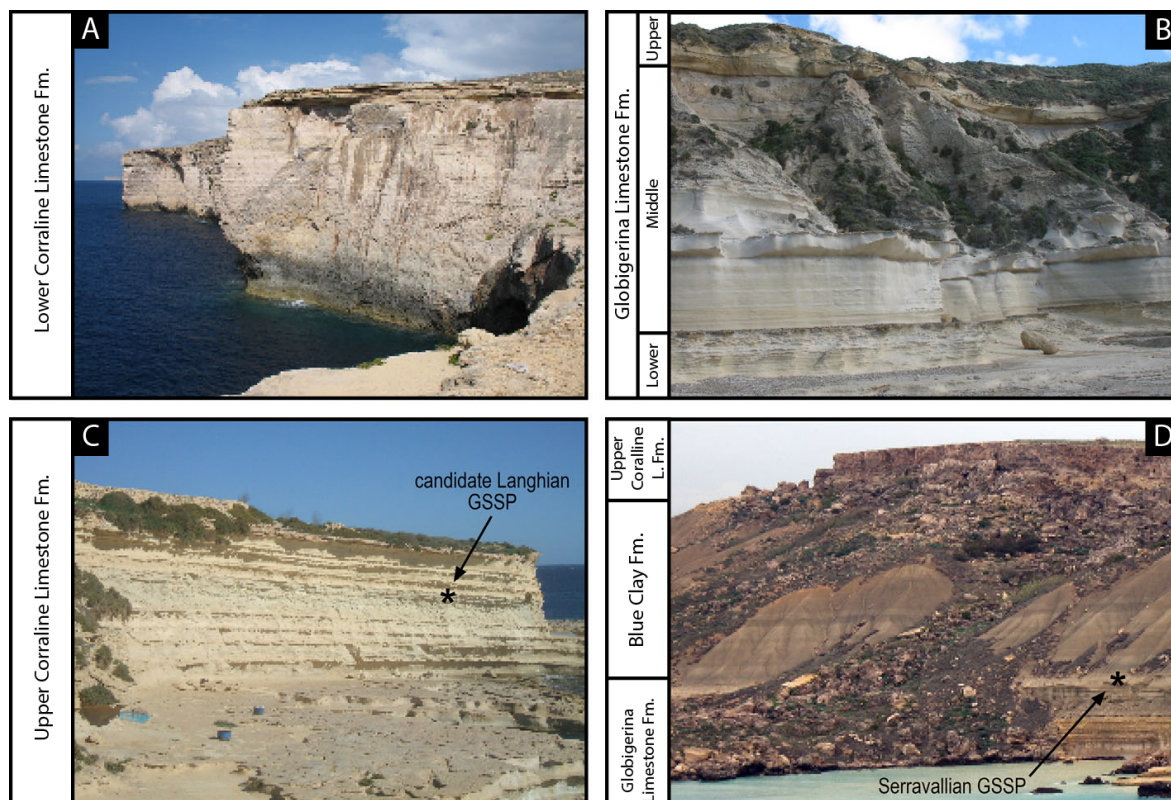
Figure 4.6: Photographs of the formations widely outcropping on the Maltese Archipelago. (A) Lower Coralline Limestone Formation; (B) Globigerina Limestone Formation; (C) Upper Coralline Limestone Formation. The Langhian Global Boundary Stratotype Section and Points (GSSP) is marked by the asterix; (D) Globigerina Limestone Fm, Blue Clay Fm, Upper Coralline limestone Fm outcropping at Ras il-Pellegrin (Malta Island). The Serravallian GSSP is marked by the asterix. Modified from Baldassini and Di Stefano (2017).

4.2.2 Early syn-rift

Middle Globigerina Limestone Member

The Middle Globigerina Member (MGLM) is deposited directly on top of the eroded surface of the phosphorite conglomerate layer capping the Lower Globigerina Limestone Mb. The formation primarily contains pale-grey globigerinid biomicrites deposited during the Burdigalian. The formation reaches its maximum thickness of 100 m at Delimara Point, on the eastern shore of Malta (Pedley et al., 1976). Unlike the LGLM, which is the most outcropped member of the limestone succession, the MGLM is far less abundant on the island surface. The MGLM is capped by an immature hard-ground surface and another conglomerate of phosphate pebbles displaying evidence of significant bioturbation (Gruszczyński et al., 2008).

Upper Globigerina Limestone Member

The Upper Globigerina Limestone Mb. can be divided into three distinct layers, where an upper and a lower yellow biomicritic limestone is separated by a marly pale-gray interval. Like the MGLM, it reaches its maximum at Delimara Point, although it never surpasses 20 m in thickness (Pedley et al., 1976). The base of the UGLM is characterized by a 10-30 cm thick layer of yellow limestone containing phosphatic particles and pebbles (Baldassini and Di Stefano, 2017). The presence of planktonic foraminifera in the rock, like the Globigerina, indicate deposition on an elevated area relative to deeper surroundings (Felix, 1973; Pedley et al., 1976).

Blue Clay Formation

The first meter above the UGLM displays a rapid shift from globigerinid biomicrites to marls of the Serravallian-Tortonian Blue Clay Formation (Pedley et al., 1976). The BCF is characterized by alternating bands of pale- to dark-grey banding related to changes in the carbonate-content (30 %) of the rock. The maximum thickness found on the Maltese Islands is 65 m, but offshore wells to the SE determined a thickness of 95 m (Dart et al., 1993). According to Pedley et al. (1976), the depositional environment of the lowermost BCF was open marine with high amounts of mud and a water depth up to 150 m. The upper parts of the formation indicate a shallowing of the environment to depths of 100 m or less, and according to Pedley (1978), with sediments originating from eroded structural highs to the west and north of the archipelago.

Greensand Formation

The Tortonian Greensand Formation on the Maltese Islands varies in thickness throughout the archipelago, but is generally only 1 m thick (Dart et al., 1993). The formation is made up of poorly cemented limestones with an abundance of dark-green and black glauconite grains. It generally caps the Blue Clay Formation with a sharp contact, but in some localities bioturbation has altered the transition to appear more gradual (Pedley et al., 1976; Pedley and Moores, 1997). The GSF is characterized by intense bioturbation, indicating shallow marine conditions during deposition (Pedley et al., 1976).

Upper Coralline Limestone Formation:
Depositional sequence 1 & 2

The Upper Coralline Limestone Formation is by Pedley et al. (1976) and (Dart et al., 1993) divided into three depositional sequences where the lower two were deposited during the early syn-rift phase (DS1 & DS2) and the final UCLF sequence (DS3) was

deposited late syn-rift. DS1 shows deposits of coralline algal biostrome facies disturbed by the Victoria Lines fault. A thin deposit of algal marl is found within the hanging-wall while a thicker algal debris succession of up to 10 m is found within the footwall. The greater carbonate sediment-accumulation on the footwall can be explained by its elevated and more photic environment relative to the subsiding hanging-wall (Dart et al., 1993). DS2 is dominated by patch reefs deposits and lies directly on top of both facies identified in DS1. Patch reefs only develop in shallow marine settings where the water depth does not exceed 10 m, indicating that the difference in elevation between hanging-wall and footwall was minimal (Dart et al., 1993).

4.2.3   Late syn-rift

Upper Coralline Limestone Formation:
Depositional sequence 3

According to Dart et al. (1993), the late syn-rift phase is defined by major growth faults creating breaks on the sea surface of up to several hundred meters and significant fault control on facies distribution. The deposits in the third sequence of the UCLF can be divided into a footwall and a hanging-wall succession separated by the Ras Hanzir fault. The footwall succession is composed of platform facies while the 30 m thicker hanging-wall succession show deposits of slope facies (Dart et al., 1993).

Pliocene succession

The Gozo Horst, North Malta Graben and Malta Horst were all significantly elevated relative to the surrounding areas during the Zanclean reflooding of the Mediterranean. This is supported by the absence of Pliocene deposits on the archipelago, while thick successions are present in the North Gozo Graben and Pantellaria Rift (Illies, 1981). According to Dart et al. (1993), the UCLF was uplifted up to 260 m relative to modern sea level on Malta.

4.2.4   Post-rift

Plio-Quaternary succession

Today, sediment is deposited in the post-rift phase as indicated by the lack of recent seismicity and lack of marine strata offset above faults (Jongsma et al., 1985; Dart et al., 1993). Onshore Malta, several caves and fissures show deposits of Pleistocene animal bones related to a fauna suited to a more temperate climate than on present Malta. It is reasonable to believe that a land-bridge existed between the Malta Horst and Sicily at the time of deposition. Alluvial fans, calcrete soils and breccias are the

youngest deposits on the Maltese archipelago (Pedley et al., 1976). The alluvial fan deposits can be attributed to the retreat of onshore fault scarps during the Quaternary (Dart et al., 1993).

Chapter 5

Results

In this chapter, data collected through field work, microscopic analysis and digital image analysis will be presented. The first section concerns new stratigraphic and structural inputs to the studied area, whereas the following sections will focus on host rock properties and characteristics of sampled deformation bands. Analysis of deformation mechanisms on the micro scale and pore size distributions within the host rock and deformation bands have been allocated significant attention.

5.1 Geology of the study area

5.1.1 Stratigraphic overview

The studied stratigraphic interval along the study area spans the Lower and Middle Globigerina Limestone Member, here referred to as LGLM and MGLM. After detailed area-mapping and consulting with local sedimentologist Peter Gatt (University of Malta), the existing stratigraphic interpretation of the outcrop (Rotevatn et al., 2016a,b) was modified to the log seen in Figure 5.1. The updated interpretation defines the phosphatic conglomerate layer, here labelled MGLM-1 (C1 in Pedley et al. (1976)), as the base of the MGLM. Digital image acquisition through the use of an UAV allowed for a geo-referenced, high-resolution 2D-model of the study area to be made (Figure 5.2). Based on field observations, the Lower Globigerina Limestone Mb. (LGLM) can be split into three units outcropping along the study area with a combined maximum thickness of 9 m. LGLM-1 (2 m) is the stratigraphically lowermost unit and is characterized by a greyish weathering surface (see Figure 5.3a). Fresh surfaces reveal a pale-yellow colour and minor bioturbation is observed throughout the unit. Deformation bands are present, both as single bands and in networks of >10s of bands. A patchy hardground surface defines the top of the subunit. The LGLM-2 unit (3.5 m) appears pale-yellow in the field and bioturbation is primarily localised in the top and
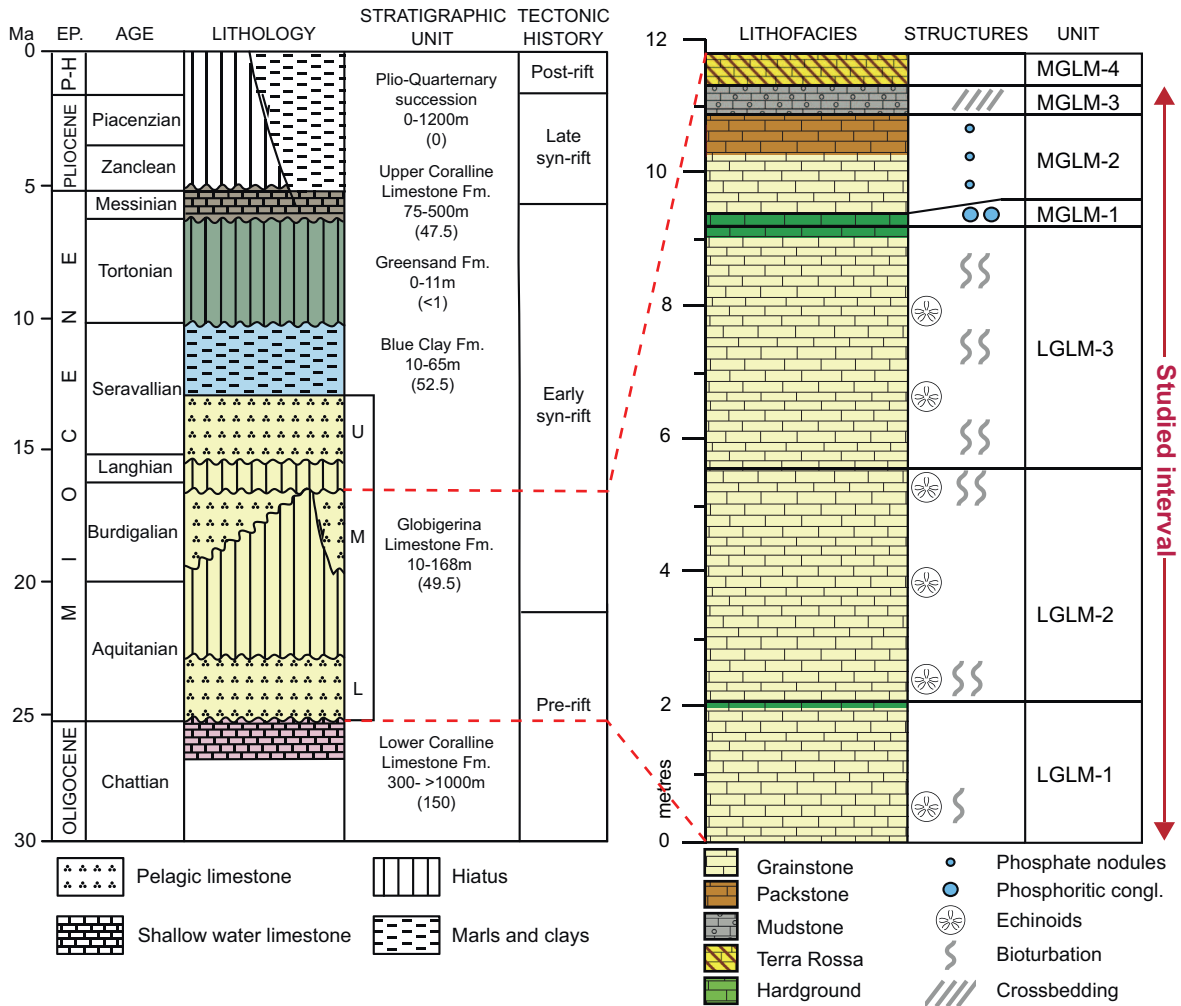
Figure 5.1: Stratigraphic log of Malta (left) and detailed log of the outcropping units in the study area (right). Modified after Rotevatn et al. (2016b).

bottom 30 cm of the subunit. LGLM-2 is characterised by narrowly spaced (<5 cm) deformation bands along the whole study area (see Figure 5.3b). The stratigraphically uppermost unit of the LGLM is LGLM-3 (3.5 m) which, similar to LGLM-2, appears pale-yellow in colour. Echinoderms fragments are observed throughout, and the top 40 cm of the unit is characterised by a patchy hardground, defining the top of the LGLM. NW-SE striking (312°), vertically dipping neptunian dykes cut through all three subunits of the LGLM.

The MGLM outcropping along the Maghlaq Fault can also be divided into three subunits of dissimilar compositions. The lowermost unit, MGLM-1 (30 cm), which sits directly on top of the LGLM, is a phosphoritic conglomerate hardground layer consisting of >2 cm large clasts of brown coloured phosphorite in a pale-yellow grainstone matrix. No deformation bands have been observed within the MGLM-1. The overlying MGLM-2 (2 m) contains smaller (<1 cm) phosphoritic clasts throughout the unit, but the majority of the rock is made up of a pale-yellow, heavily bioturbated grain-
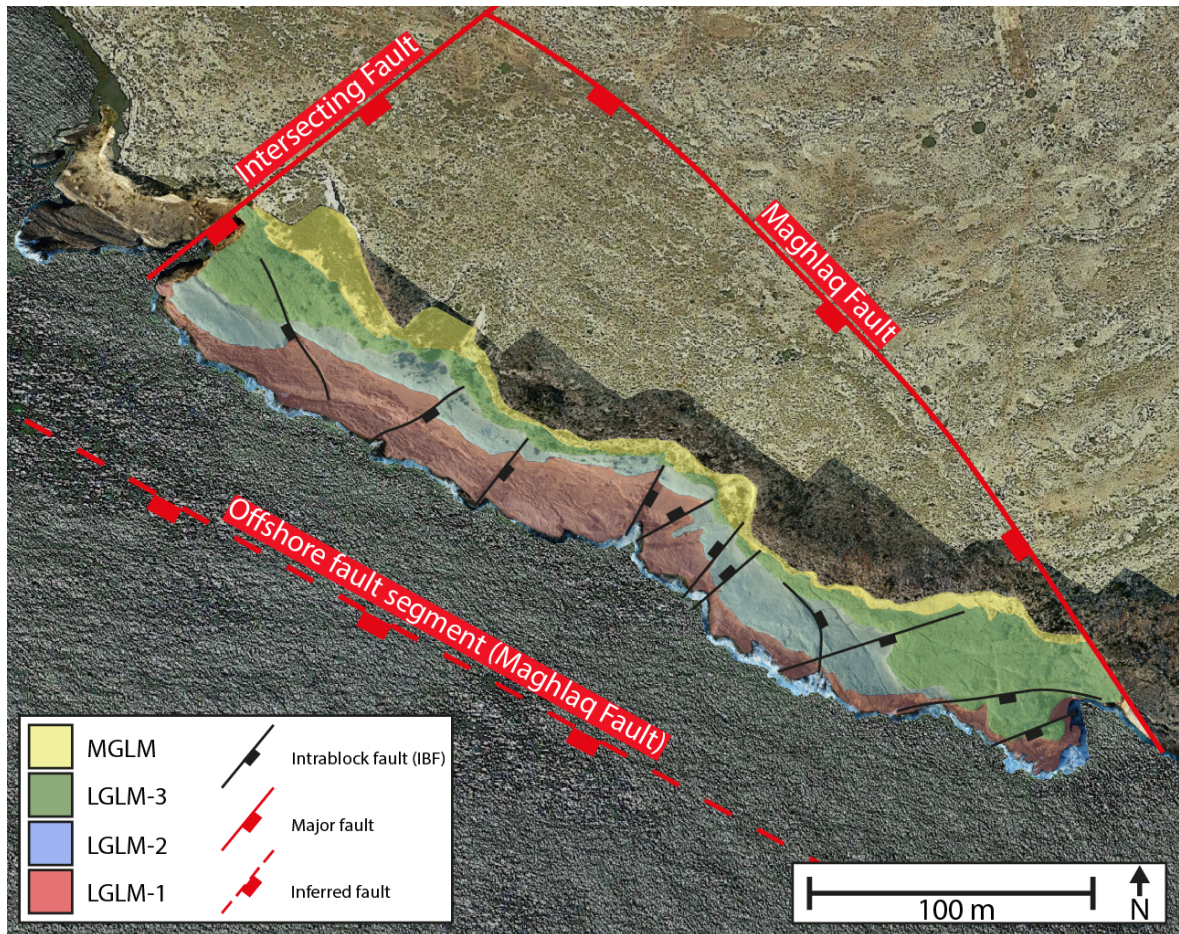
Figure 5.2: Overview of the study area at Ras il-Bajjada on the southwestern coast of Malta. Major faults (red), intrablock faults (black) and the outcropping units of the Globigerina Limestone Formation are marked and labelled on the map. Images from UAV-mapping and Google Earth.

stone. Only a few deformation bands are present, with an average deformation band frequency of less than 1 per metre (see Figure 5.4b). The uppermost unit, MGLM-3 (1 m), appears pale-gray to white in the field (see Figure 5.4c) and the grain size overall finer-grained. The height of the outcropping MGLM-3 varies from 0 m to 3 m along the outcrop. Within the steep, cliff-like (up to 3 m) sections of the MGLM-3, multiple extension fractures within the unit can be observed 5.4c. No deformation bands have documented in MGLM-3. Sample collection from the DB-lacking MGLM-1 and MGLM-3 was not prioritized and their characteristics will not be elaborated on further in the chapter.
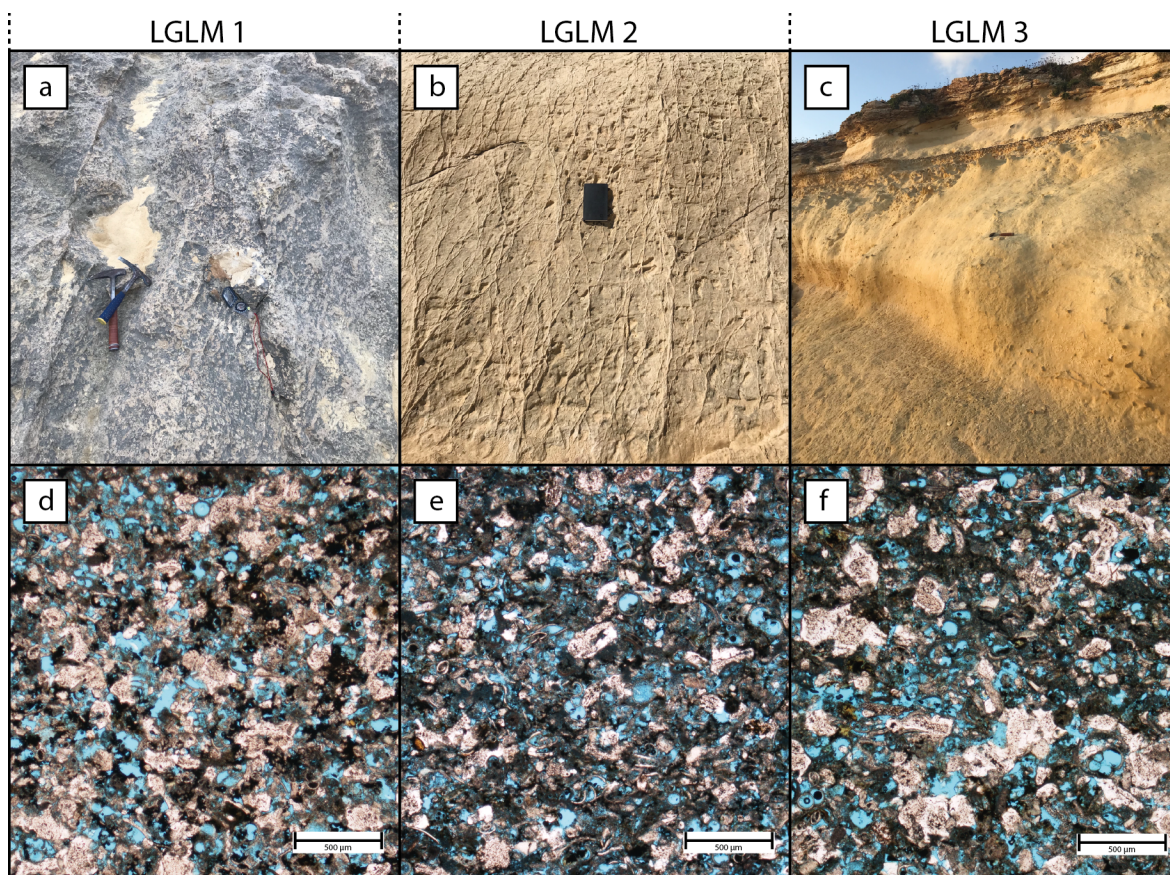
Figure 5.3: Overview and comparison of the outcropping units of the Lower Globigerina Limestone Member in field scale and in thin sections. Although the units' macro-scale appearance vary ((a)-(c)), their composition on the micro-scale is similar ((d)-(f)). (a) LGLM-1 field photo displaying the gray weathering surface and pale-yellow fresh surface. Hammer for scale. (b) LGLM-2 field photo showing the characteristic deformation band network found throughout the unit. Notebook for scale. (c) LGLM-3 field photo. Although deformation bands are present, the unit contains significantly less deformation bands than the underlying LGLM-2. (d) LGLM-1 in thin section. (e) LGLM-2 in thin section. (f) LGLM-3 in thin setion. Bioclasts are primarily composed of echinoderms, bivalves and foraminifera. Pores, highlighted by the blue epoxy, is found both between bioclasts (interporosity) and within foraminifera tests (intraporosity).

5.1.2 Structural overview

Faults

The studied outcrop is situated along the hanging wall of the Maghlaq Fault (MF), on the coast of southwest Malta. Two large, sub-perpendicular faults confine the study area. Of these two, a NW-SE oriented segment of the MF is the largest, wheras the intersecting fault is oriented SW-NE (see Figure 5.2). Minimum displacement for the MF within the study area is estimated by Bonson et al. (2007) to be >50 m and >10 m for the intersecting fault. Bonson et al. (2007) also proposed a large NW-SE oriented segment of the MF located just offshore from the study area (see Figure 5.2).
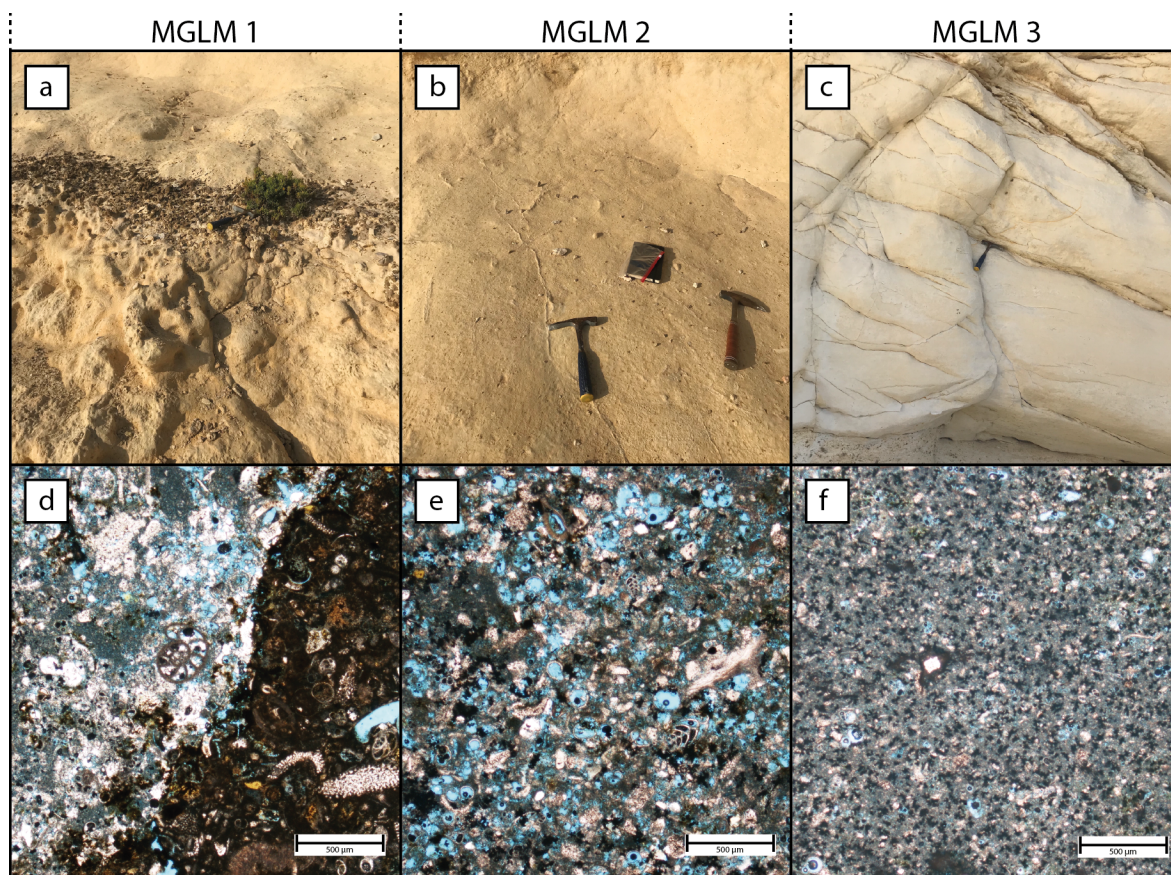
Figure 5.4: Overview and comparison of the outcropping units of the Middle Globigerina Limestone Member in field scale and in thin sections. Within the MGLM units there are significant differences both in outcrop appearance ((a)-(c)) and in composition on the micro-level ((d)-(f)). (a) MGLM-1 field photo of the phosphatic conglomerate defining the base of the MGLM. Hammer for scale. (b) MGLM-2 field photo showing one of the isolated deformation bands overlapping with another. Hammer and notebook for scale. (c) MGLM-3 field photo of the pale-gray unit. Multiple fractures are found in the unit, but deformation bands are absent. Hammer for scale. (d) MGLM-1 in thin section showing a dark phosphorite clast next to the grainstone-matrix. (e) MGLM-2 in thin section showing a composition similar to LGLM.(f) LGLM-3 in thin section displaying a clear grain-size reduction from the other outcropping units.

This proposed fault is extrapolated from the outcropping MF segment outcropping at Tal-Gawwija, 200 m west of the study area (see Figure 1.2). A number of smaller faults offset the exposed Globigerina Limestone Formation along the whole outcrop (see Figure 5.5). The smaller intrablock faults (IBF) were categorized into two: (1) IBF oriented SW-NE and (2) IBF oriented NW SE. As seen in Figure 5.5, the two orientations are perpendicular to the two major faults confining the study area. Three IBFs oriented ESE-WNW were also observed along the western part of the study area, highlighted in green in Figure 5.5. The fault traces were up to 20 m long with a distinct serpentine shape, parallel to the coastline. These were interpreted as growth faults as lithified, in-situ reef-remnants were seen growing from the footwall down onto the fault
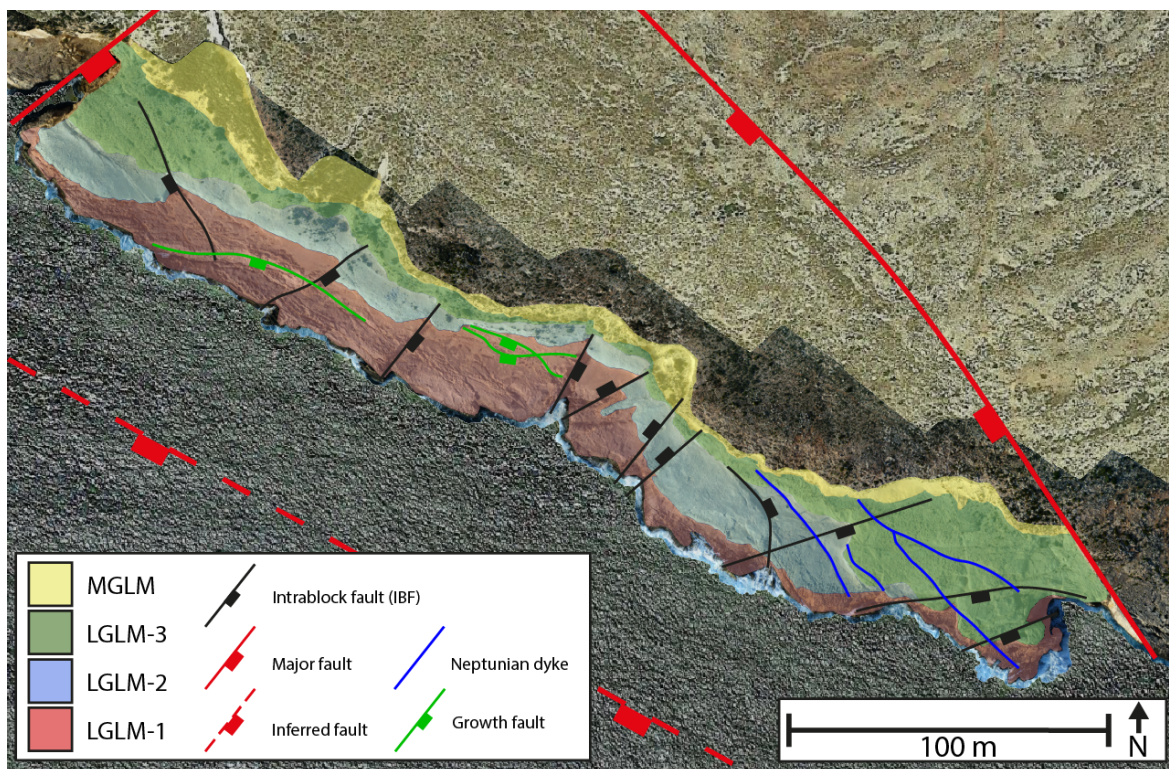
Figure 5.5: Structural overview of the study area. In addition to major faults and units of the GLF, neptunian dykes (blue) and observed growth faults (green) have been highlighted.

scarp, which has a displacement of around 1 m.

Deformation bands

Deformation bands (DB) have been found in host rock of different compositions and porosities within both the Lower and Middle Globigerina Limestone Member. The variation in DB frequency and distribution between LGLM subunits have been extensively documented by previous studies and a summary of key measurements is listed in Table 5.1. Bed-perpendicular deformation bands were documented in all of the LGLM subunits at the study area by Rotevatn et al. (2016b), and they were classified as compactional shear bands (CSB) with measured displacements of up to 6 mm. Within the deformation bands, pressure solution processes were the dominant deformation mechanisms, although cataclasis-dominated bands have also been documented in the study area. A thorough description of observed deformation mechanisms is presented as part of the micro-structural analysis in section 5.2.2.

In LGLM-1, DBs appear both as single, isolated bands and in networks of >5 cm spaced DBs. The overall trend of DBs in LGLM-1 is ENE-WSW (Table 5.1), but there are some variations in measured orientations. The DB frequency in LGLM-1 varies from less than 1, to 6 DBs per metre, with an average of 1.4 per metre (Table 5.1). Average thickness of DBs in LGLM-1 is 2.7 mm. DBs in LGLM-2 are primarily found in up to

(10 m) wide networks of >5 cm spaced bands, as seen in Figure 5.3b. DBs in MGLM-2 have a ENE-WSW trend and are predominantly oriented at a high angle to bedding. Bed-parallel bands have been documented in the western part of the study area, but are not common. Below the intensively burrowed top of LGLM-2, frequencies of up to 12 DBs per metre have been recorded, which is the highest along the study area. The average frequency of DBs in LGLM-2 is 5.2 DBs per metre and their average thickness is 3.5 mm (Table 5.1). Large planar surfaces of outcropping LGLM-3 are not found along the entire study area, but are limited to one location in the western end of the outcrop and one in the eastern end (Figure 5.5). Due to scree material covering the western LGLM-3 surface, deformation bands are only exposed in the eastern part. The measured DBs in LGLM-3 show a WNW-ESE trend and are oriented with a high angle to bedding, similar to the two underlying subunits. The average DB frequency is 5 DBs per metre and the average DB thickness is 3.2 mm. The maximum measured frequency in LGLM-3 is 9 DBs per metre. In the MGLM, compactional shear bands are only observed within MGLM-2, displaying a ENE-WSW trend with a high angle (>80°) to bedding. The average DB frequency in MGLM-2 is estimated to be 0.1 DB per metre. No bed-parallel bands and no networks or clusters of DBs have been documented in the MGLM.

Table 5.1: Summary of key measurements done on deformation band characteristics in the Lower Globigerina Limestone Member (LGLM) by previous studies (Thorsheim, 2015; Rotevatn et al., 2016b). DBs in the Middle Globigerina Limstone Member (MGLM) were recorded during field work for this project. No deformation bands have been found in MGLM-1 and MGLM-2. Steronet plots of DBs orientations measured by Thorsheim (2015) can be seen in Figure 1 in Appendix A.

Parameters	Subunits			
	LGLM-1	LGLM-2	LGLM-3	MGLM-2
Frequency (DB per m)	1.4	5.2	5.0	0.5
Thickness (mm)	2.7	3.5	3.2	-
Dominating trend	ENE-WSW	ENE-WSW	ENE-WSW	ENE-WSW

5.2 Micro-structural analysis

5.2.1 Host Rock Characterization

The host rock samples from the LGLM and MGLM are classified as bioclastic packstones to grainstones (sensu Dunham 1962, Figure 3.1) as they are consistently grain-supported, but with a varying mud-content. This mud, or matrix, consists of fine- to cryptocrystalline carbonate fragments, clay minerals and quartz. The matrix also contains significant amounts of micropores, often far smaller in size than the macro-
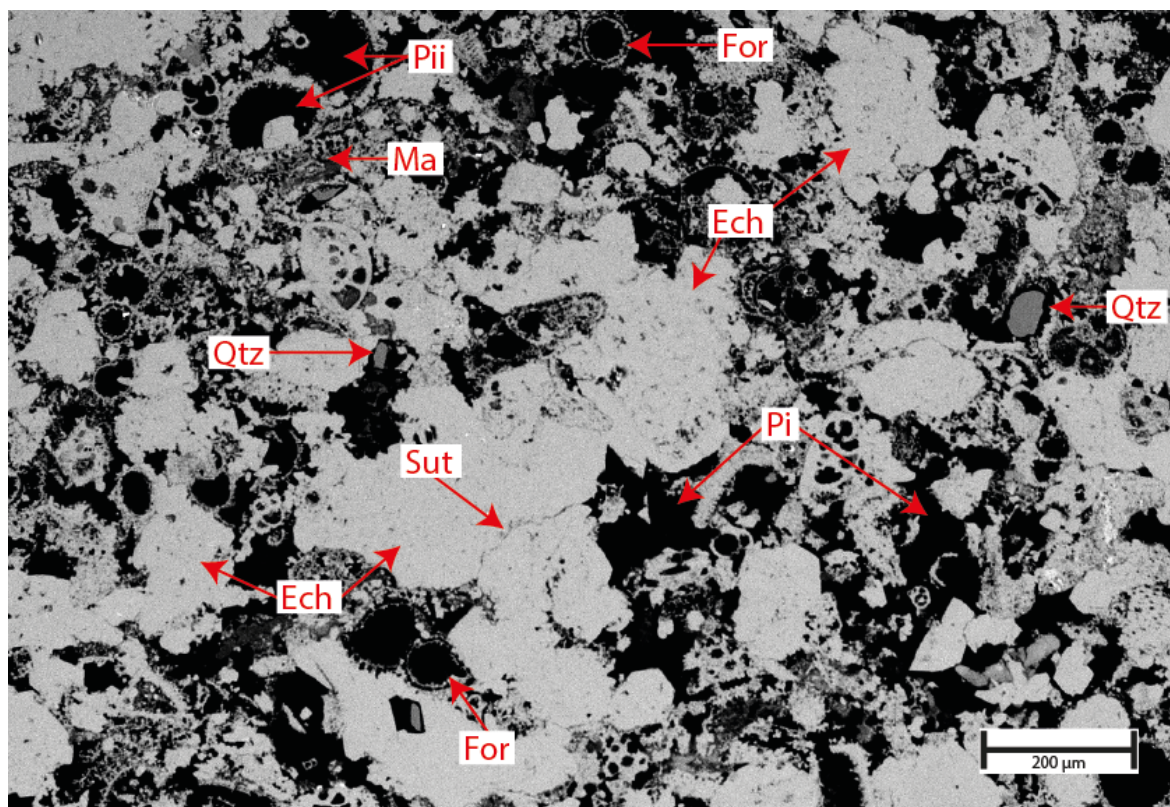
Figure 5.6: BSE-SEM image with labelled components of the host rock grain assemblage. Echinoderm fragments (Ech), are the most common bioclasts in the rock. Sutured grain contacts (Sut) can be observed between echinoderm fragments, indication pressure solution. Foraminifera (For) are also common in the assemblage, typically displaying intraporosity (Pii) within intact tests. Quartz grains (Qtz) are easily recognized in BSE-SEM images by their dark appearance, in contrast to brighter carbonate grains. Matrix (Ma) consisting of fine- to cryptocrystalline carbonate fragments, quartz and clay minerals can be observed in varying amounts filling both interpores (Pi) or intrapores (Pii).

/micropore treshold at $<500\,\mu m^2$, sensu Anselmetti et al. (1998). Bioclasts account for the majority of the host rock volume and the grain assemblage consists primarily of echinoderm spines and fragments, planktonic foraminifera (mostly globigerinids) and bivalves (Figure 5.6). Quartz grains ($<100\,\mu m^2$) are scattered throughout the samples from all the members and formations. Pores within the host rock can be split into two categories: interpores (interporosity, between grains) and intrapores (intraporosity, inside grains), sensu Choquette and Pray (1970). Most of the intrapores preserved in the host rock stems from chambers of more or less intact foraminifera tests. Comparing the LGLM host rock in Figure 5.3d-f with the MGLM-2 host rock in Figure 5.4e, foraminifera bioclasts are qualitatively determined to be more frequent in MGLM-2 than in the subunits of LGLM. Within the different formations and units, compositional heterogeneities are primarily caused by changes in the relative amount of bioclasts, pores and matrix. Between the two formations however, the dissimilarity can be attributed to bioclast diversity in addition to differences in overall grain and
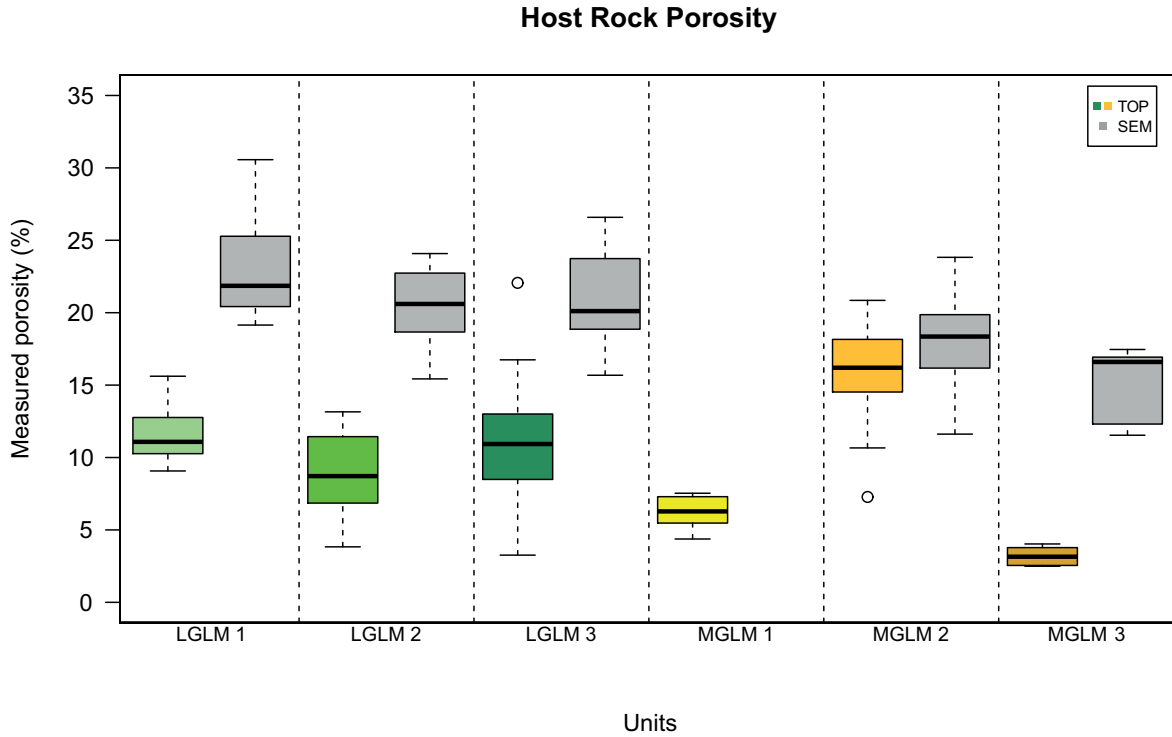
Host Rock Porosity

Figure 5.7: Boxplots of measured porosity of undeformed host rock samples from thin section photomicrographs from the geological units in the study area. The figure displays the difference in measured macroporosity (from photomicrographs) and combined macro- and microporosity (from SEM-BSE images, TOP). The boxes display interval of measurements within the 2nd and 3rd quantile, with the mean represented by the horizontal black line. The dashed lines above and below the boxes indicate the interval between the maximum and minimum measured value (exluding outliers, plotted as points). For the TOP-measurements, no pores below $500\,\mu m^2$ are included as they fall below the image resolution of the photomicrographs. Mean values of the measurements can be seen in Table 5.2. See Appendix B for the full dataset.

pore size.

Table 5.2: Mean values for measured macroporosity (OM) and micro- and macroporosity (SEM) in outcropping Lower and Middle Globigerina Limestone Mb. Macroporosity is here defined as pores ($>500\,\mu m^2$). Deformation bands have been observed in all units except for MGLM-1 and MGLM-3.

Unit	Macroporosity	Macro- and microporosity	DB-hosting unit
LGLM-1	11.52 %	23.08 %	Yes
LGLM-2	8.77 %	20.46 %	Yes
LGLM-3	11.29 %	21.00 %	Yes
MGLM-1	6.19 %	-	No
MGLM-2	15.75 %	18.17 %	Yes
MGLM-3	3.19 %	14.99 %	No

Measurements of pore properties like perimeter, roundness and size have been ac-

Figure 5.8: Pore-size distribution analysis of LGLM-1 and MGLM-2 thin section samples. Exceedence frequency (points) and cumulative porosity, or cumulative pore volume, (dashed lines) is plotted against pore size (μm^2). Exceedence frequency displays the distribution of pore sizes, while the cumulative porosity plot shows the contribution of increasing pore sizes to the overall porosity. The dashed vertical line represents the threshold for micro- and macroporosity

quired through digital image analysis (DIA) on SEM-BSE images. Figure 5.7 displays the results of porosity measurements on BSE-SEM images (SEM) and optical microscope (TOP) for the different subunits. Because measured porosity from BSE-SEM images includes all pores $>2\,\mu m^2$ and TOP-measurements only include pores $<500\,\mu m^2$ (i.e. macroporosity), the difference in porosity from these two methods gives an estimate of the microporosity (Anselmetti et al., 1998). To quantify the relative size and distribution of pores within a unit, pore size distribution analysis has been carried out. Figures 5.8-5.10 compares pore size distribution of the units with high (>1 DB per metre) deformation band frequencies (LGLM-1, LGLM-2 and LGLM-3) with MGLM-2, where deformation bands are more widely spaced (<1 DB per metre). The figures show Exceedence Frequency (EF) and cumulative porosity (%) plotted against pore sizes (μm^2). At each measured pore size, EF is defined as the number of measurements larger than that specific size, divided by the total number of measurements (Torabi et al., 2007). By comparing the EF curve for the three LGLM units, a gradual shift of
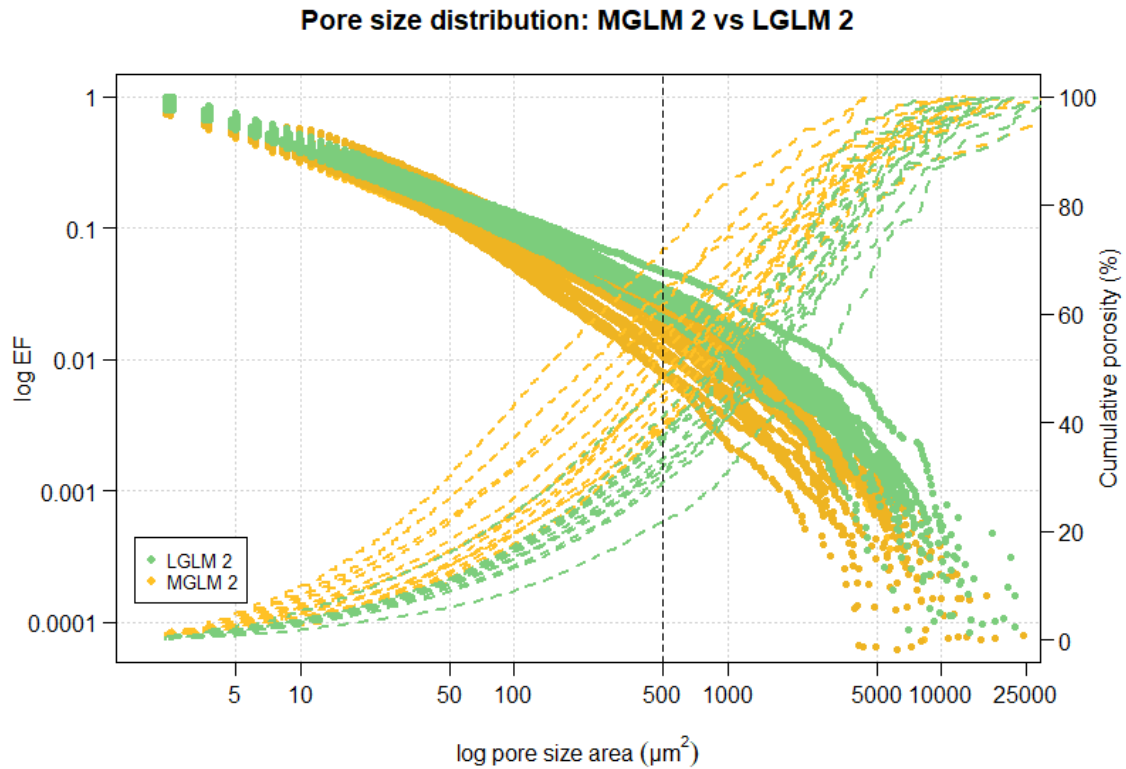
Figure 5.9: Pore-size distribution analysis of LGLM-2 and MGLM-2 thin section samples. Exceedence frequency (EF) and cumulative porosity is plotted against pore size (μm^2).

the curve downwards is observed when moving stratigraphically upwards. The cumulative porosity plots shows, for given pore sizes, how much of the measured porosity stems from pores up to that size. For MGLM-2, the cumulative porosity plots in Figures 5.8-5.10 show that micropores account for a larger portion of the total porosity than what is seen for the three subunits of LGLM. A shift for the cumulative porosity curve is also observed between the three LGLM units. In this case, the curve gradually moves towards the left when moving stratigraphically upwards, showing an increase in the relative porosity contribution from smaller pores. For pore sizes $<500\,\mu m^2$ (i.e. micropores), the mean porosity contribution in MGLM-2 is just below 50% (see Table 5.3). For units LGLM-1, -2 and -3, micropores account for around 26%, 35% and 38% of the measured porosity, respectively. For macropore-porosity in LGLM, the highest gradient in the cumulative plot is observed in pore sizes from $1000\,\mu m^2$-$5000\,\mu m^2$. In MGLM, the highest gradient in equivalent plot is observed over a larger span of pore sizes than, from $300\,\mu m^2$-$5000\,\mu m^2$.
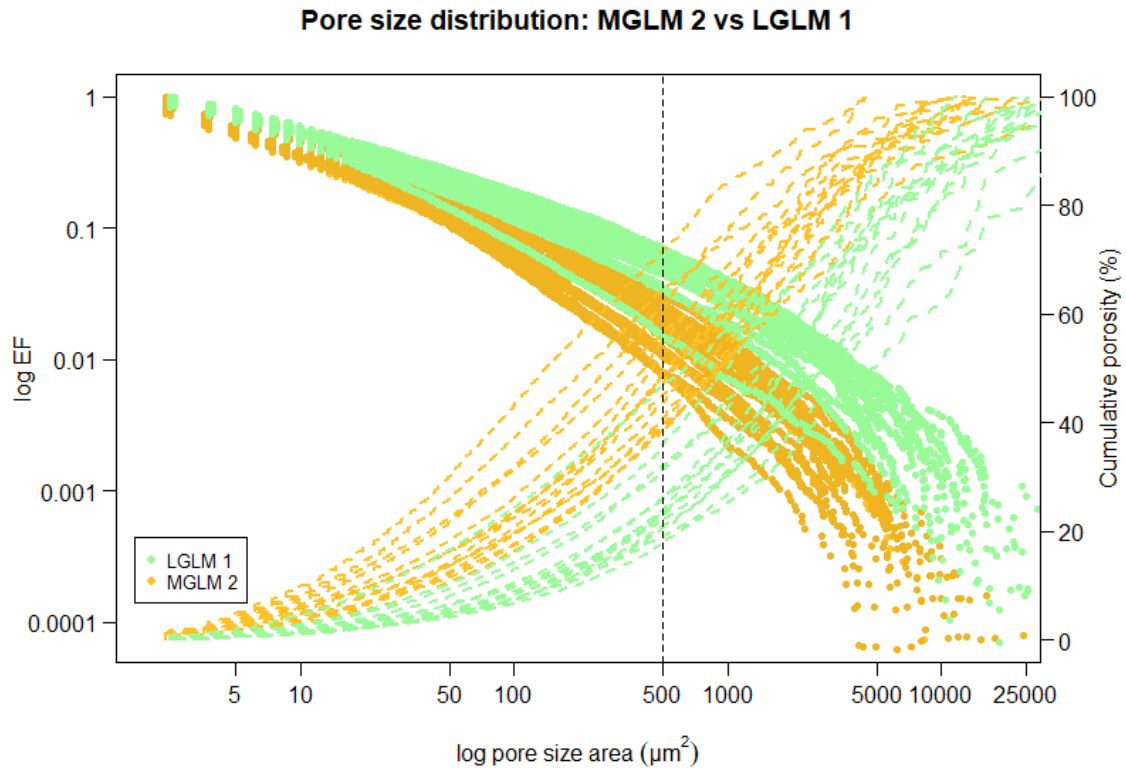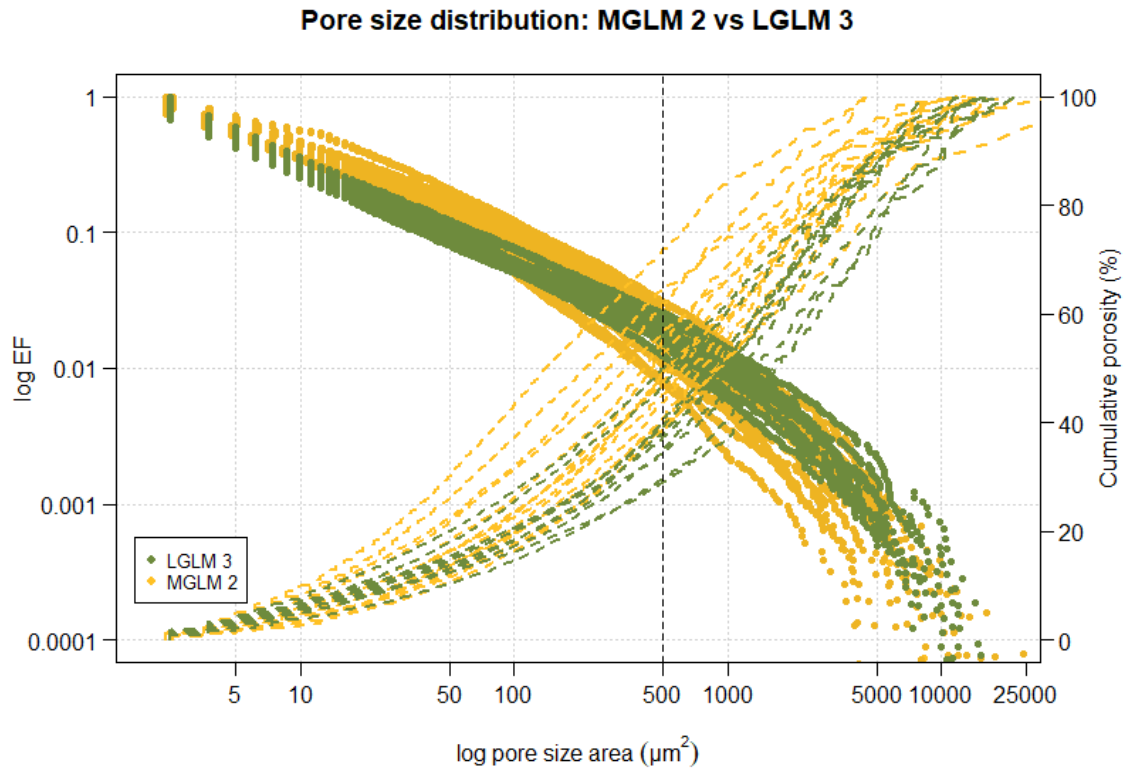
Figure 5.10: Pore-size distribution analysis of LGLM-3 and MGLM-2 thin section samples. Exceedence frequency (EF) and cumulative porosity is plotted against pore size (μm^2).

Table 5.3: Mean values for cumulative porosity at specific pore sizes within the undeformed host rock of deformation band carrying subunits. Plots of the individual sample distributions can be seen in Figures 5.8-5.10.

	Pore size area				
Subunit	$10\,\mu m^2$	$50\,\mu m^2$	$500\,\mu m^2$	$5000\,\mu m^2$	$10\,000\,\mu m^2$
MGLM-2	5.5 %	16.9 %	49.6 %	90.7 %	96.6 %
LGLM-3	5.9 %	14.5 %	38.0 %	84.3 %	94.6 %
LGLM-2	3.2 %	10.6 %	34.6 %	83.7 %	94.6 %
LGLM-1	1.8 %	7.0 %	26.4 %	72.0 %	84.9 %

5.2.2   Deformation band characterisation

Deformation bands in LGLM

Deformation bands have been found in all three LGLM subunits outcropping at the study area. A porosity reduction in all DBs, relative to the host rock, is observed for all LGLM subunits. Table 5.4 shows the mean measured porosities for DBs and HR for the DB hosting subunits, along with the calculated reduction factor (R_f), which is the ratio between the HR and DB porosity measurements. Of the LGLM subunits,
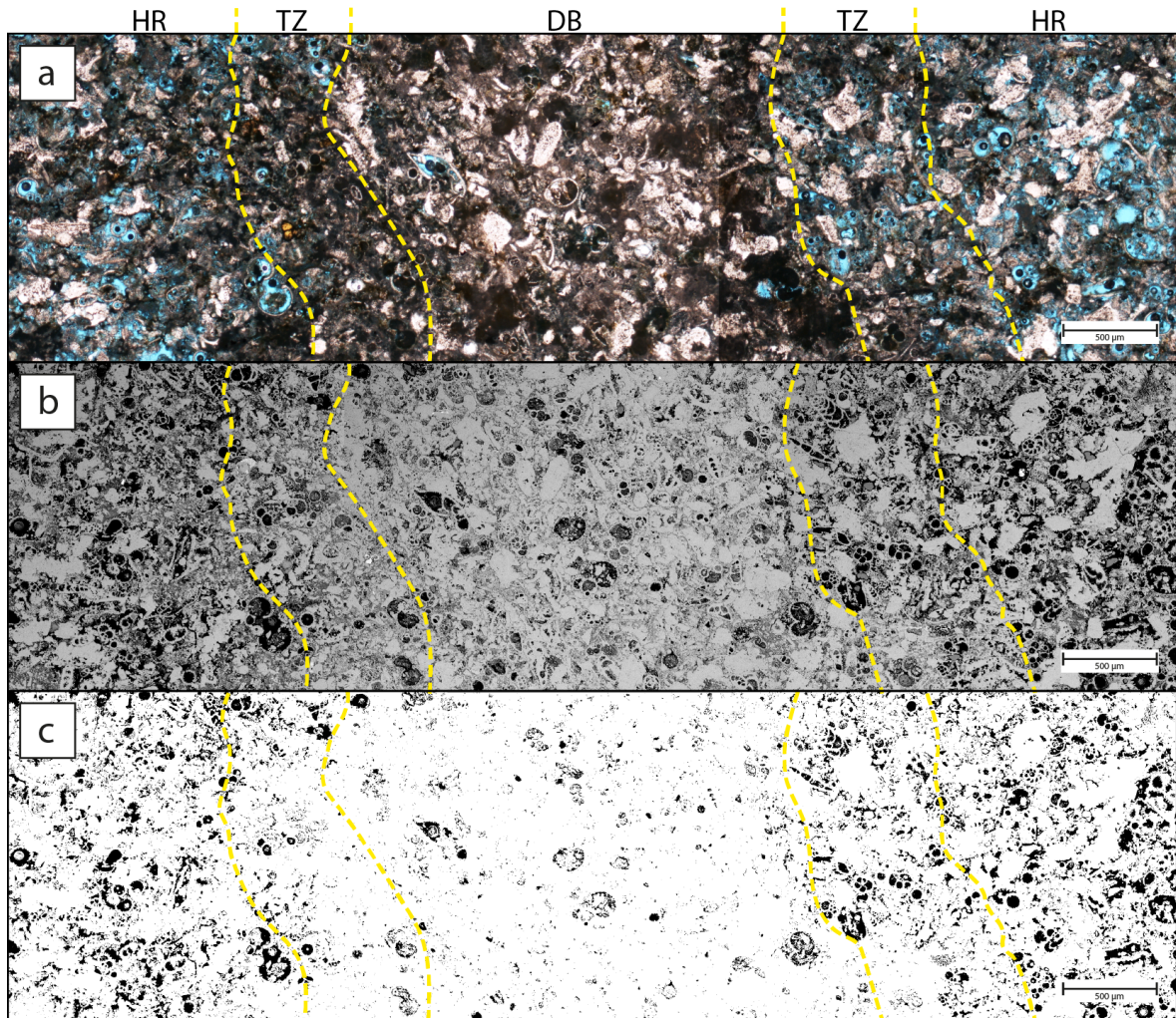
Figure 5.11: Profiles across a single deformation band in LGLM-2. The borders between undeformed host rock (HR), transition zone (TZ) and deformation band core (DB) have been marked with dashed yellow lines. (a) Thin section photomicrographs from an optical microscope where pores are filled with blue-coloured epoxy. (b) Stiched SEM-BSE images of the same profile as (a). (c) Pores (black) detected through digital image analysis (DIA) on the SEM-BSE images from (b). The reduction in overall porosity within the deformation band core is distinctly recognisable relative to the adjacent host rock.

the lowest porosity reduction is seen in bands from LGLM-1 with an R_f of 0.38. DBs from both LGLM-2 and LGLM-3 show just over four times as high porosity in the HR, relative to the DBs ($R_f = 0.24$). Figures 5.11-5.12 show two sets of three profiles across two DBs from LGLM-2 and MGLM-2. Combining the three profiles ((a) optical microscope, (b) BSE-SEM, (c) binary pore-images) allows for different characteristics across the deformation band to be observed. Within the core of LGLM deformation bands, little matrix is observed between bioclasts (Figure 5.13). Looking at Figure 5.11b, it is possible to qualitatively determine that echinoderm fragments make up of most of the bioclasts wheras foraminiferas are the second most abundant in the profile. The alignment of elongated grains with the DB orientation seems to increase from the
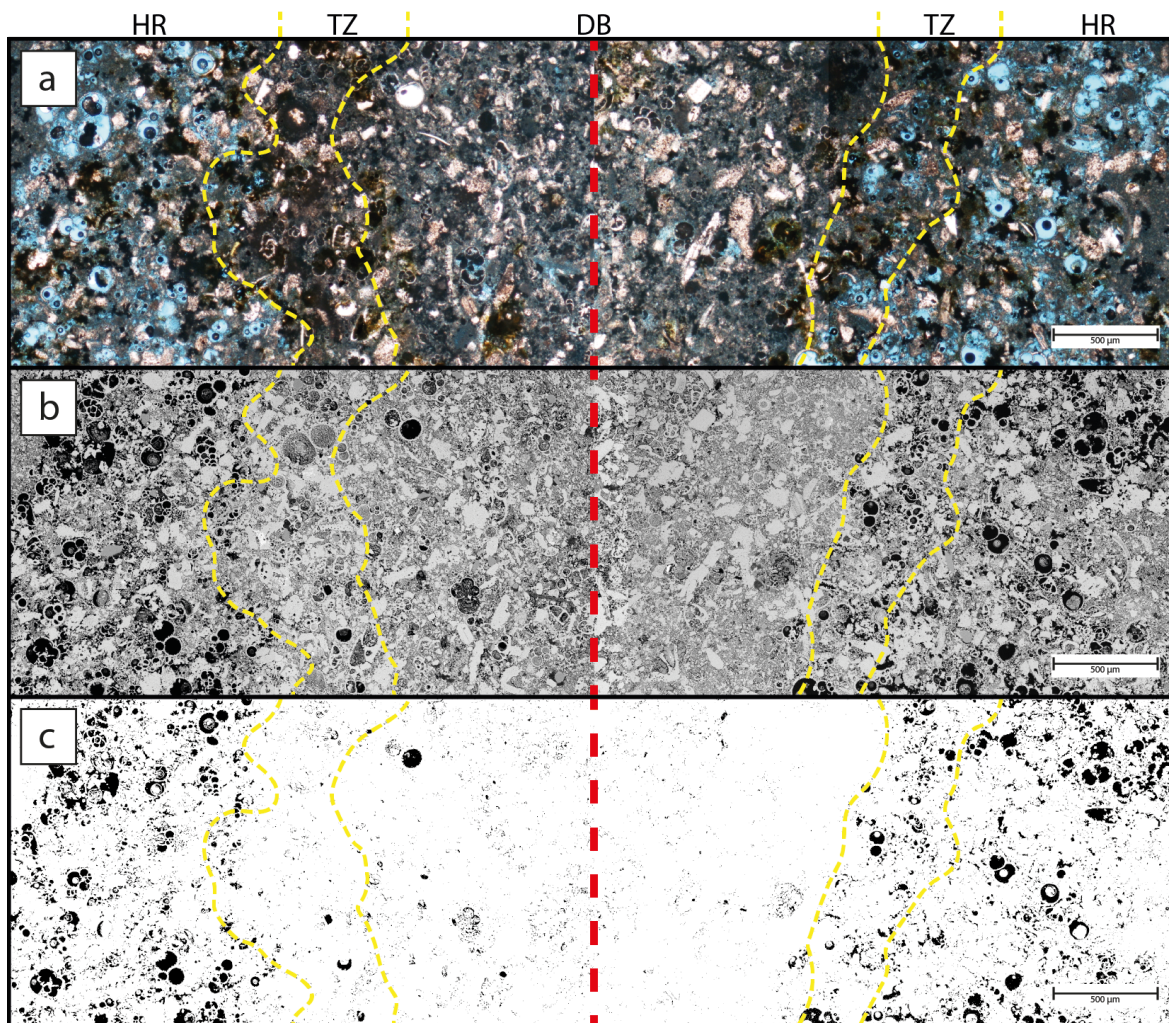
Figure 5.12: Profiles across a single deformation band in MGLM-2. The borders between undeformed host rock (HR), transition zone (TZ) and deformation band core (DB) have been marked with dashed yellow lines. A portion of the DB core has been removed at centre of the image (dashed red line) to include the zones on both sides. (a) Thin section photomicrographs from an optical microscope where pores are filled with blue-coloured epoxy. (b) Stiched SEM-BSE images of the same profile as (a). (c) Pores (black) detected through digital image analysis (DIA) on the SEM-BSE images from (b). The reduction in overall porosity within the deformation band core is distinctly recognisable relative to the adjacent host rock.

undeformed HR to the DB core. Sutured grain contacts are frequently observed at grain boundaries between echinoderm fragments (Figure 5.6). Cement growth inside intrapores is observed in most foraminifera tests, but have also been observed inside interpores. Intact foraminifera tests inside deformation bands have preserved a proportion of its intraporosity. This proportion, which is dependant on the the amount of matrix filling in the intrapores, is relatively higher within the bands compared to the foraminifera found in the undeformed host rock, as seen in Figure 5.11b. The difference is seen more clearly by comparing 5.11b and 5.11c.
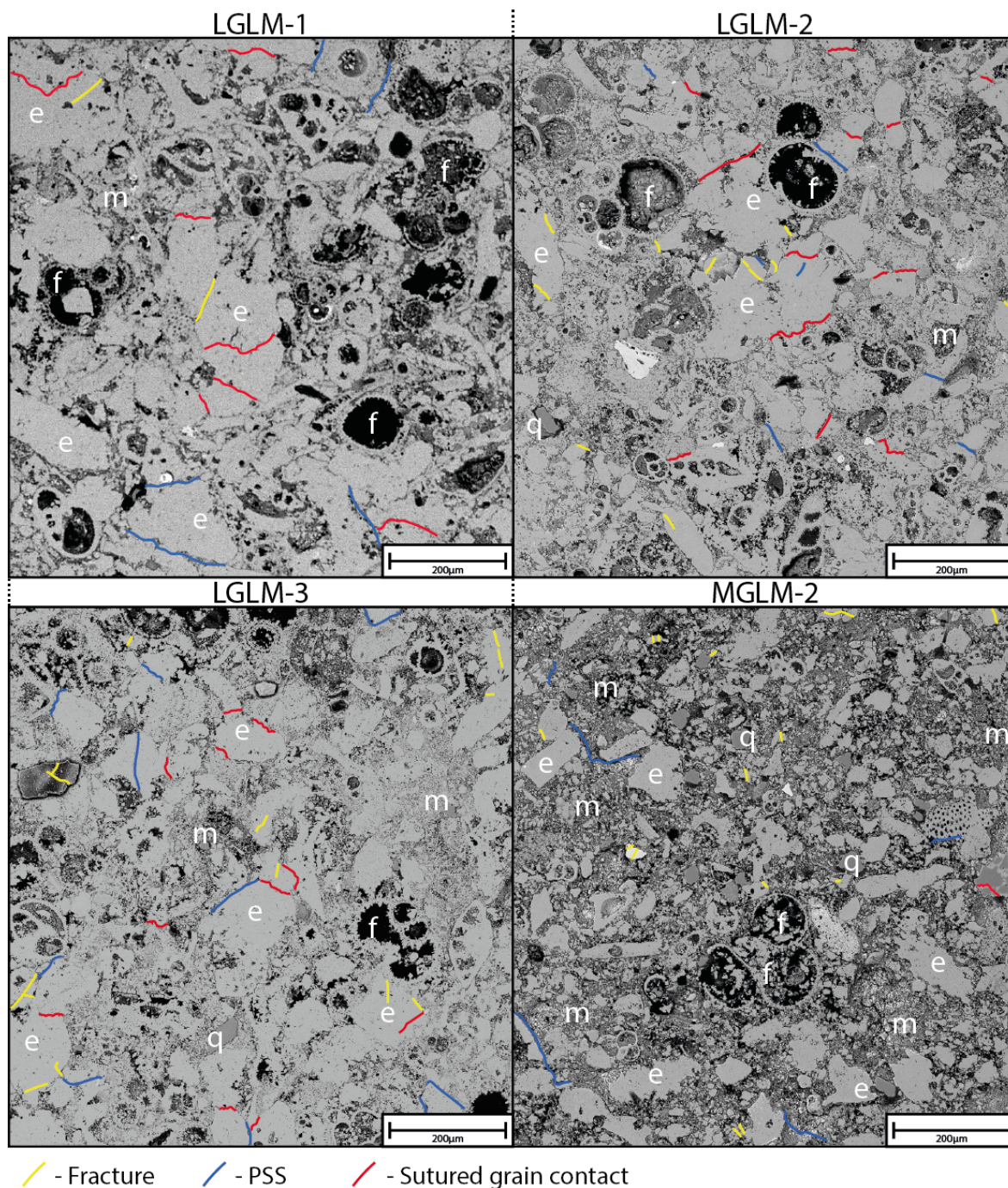
Figure 5.13: BSE-SEM images of deformation band cores from all units that host DBs. Grain components like echinoderms (e), foraminifera (f), quartz grains (q) and matrix (m) have been labelled. Fractures, pressure solution seams (PSS) and sutured grain contacts have also been highlighted in the figure. The vertical axis for all cores is parallel to the corresponding DB orientation.

Deformation bands in MGLM

Of the three outcropping units of the MGLM along the Maghlaq Fault, deformation bands have only been observed in MGLM-2. Unlike what is commonly observed in
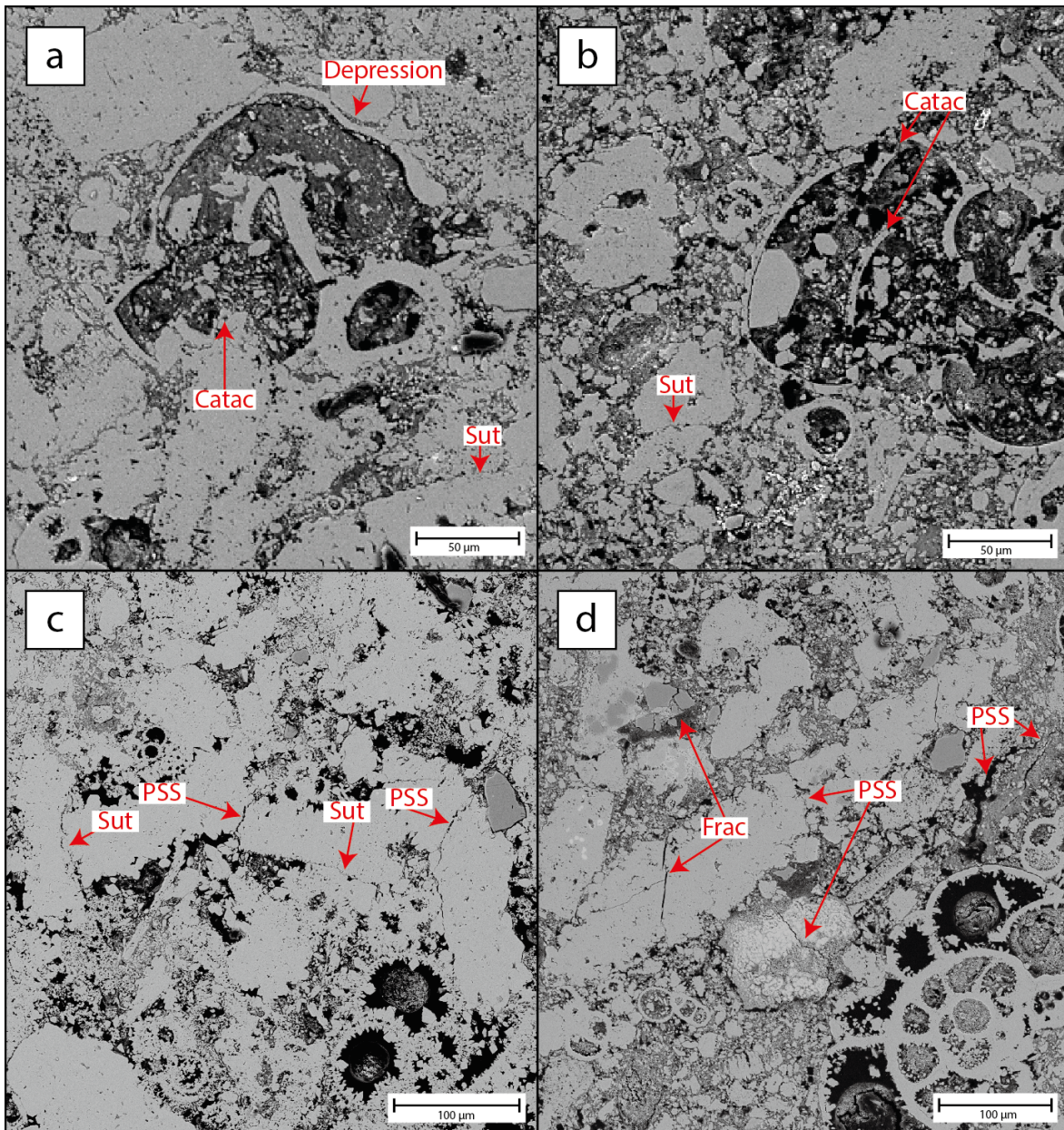
Figure 5.14: BSE-SEM images with highlighted deformation mechanisms. (a) A fractured foraminifera test from inside a deformation band in LGLM-2. An impression made by an adjacent grain have also been marked. (b) A distinctly fractured foraminifera test with matrix infill from MGLM-2. (c) LGLM-1 DB with distinct sutured grain contacts between echinoderm fragments. (d) Fractures within echinoderm fragments and quartz grains in an LGLM-3 DB. PSS are also seen between grains and within the matrix.

LGLM, the DBs in MGLM-2 are isolated and the overall frequency of bands is lower. A porosity reduction from the undeformed HR to DBs is also observed in MGLM-2 bands. Here, the measured porosity in the HR is on average over five times higher than inside the DBs, with a R_f value of 0.19 (Table 5.4). At microscale, the DB core in MGLM-2 appears to be separated from the host rock by two distinct transition zones (Figure 5.12a). In the DB from MGLM-2 in Figure 5.12, the overall grain size within

Figure 5.15: Pore-size distribution analysis of LGLM-1. Exceedence frequency (points) and cumulative porosity (dashed lines) is plotted against pore size (μm^2). Exceedence frequency displays the distribution of pore sizes, while the cumulative porosity plot shows the contribution of increasing pore sizes to the overall porosity. The dashed vertical line represents the threshold for micro- and macroporosity

the DB is visibly lower than what is observed in LGLM bands 5.11. By looking at the undeformed host rock in the same profile, it is evident that the size reduction of echinoderm fragments, compared to in the LGLM, is present also outside the DB. Most forminifera tests temain intact within the DB core, although fractured tests have been observed 5.14b. The bioclasts inside the DB are generally matrix supported, leading to fewer long grain-to-grain contact surfaces, which is where most of the observed grain sutures is located in other units.

Deformation mechanisms

Visible evidence of specific deformation mechanisms within the deformation band cores have been highlighted in Figure 5.13. Here, a high-resolution BSE-SEM image of a DB core from each of the DB-containing units of the study area have been analysed for fractures, pressure solution seams (PSS) and sutured grain contacts. Although PSSs and sutured grain contacts are evidence for the same deformation mechanism, pressure solution, they represent different stages, where sutured grain contacts are considered
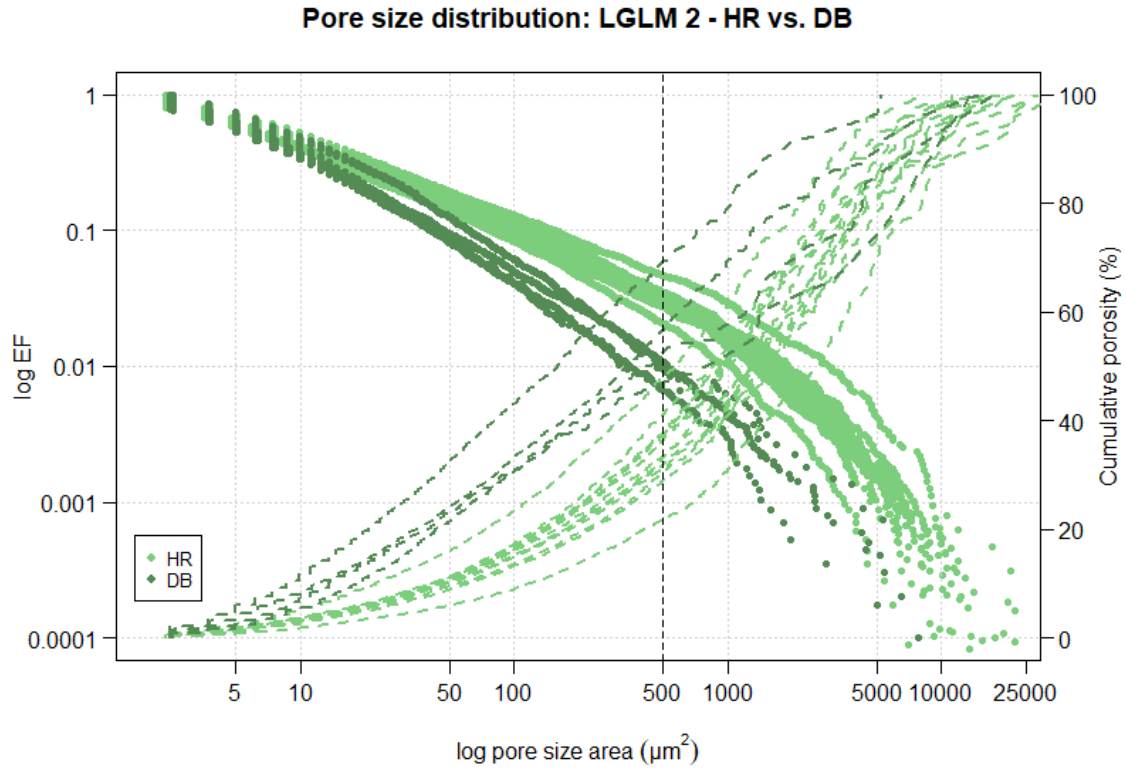
Figure 5.16: Pore-size distribution analysis of LGLM-2. Exceedence frequency (points) and cumulative porosity (dashed lines) is plotted against pore size (μm^2).

Table 5.4: Mean values of measured porosity (ϕ) from undeformed host rock and inside deformation bands. D represents the dimension (exponent) of the power law fitted to the pore size distribution plots seen in Figures 5.15-5.18. D is originally two dimensional, but the listed mean values in the table have been converted to three dimensions. ΔD is simply the difference between the calculated D value from HR and DB. Reduction factor (R_f) quantifies the porosity reduction from the host rock to deformation bands and is simply the DB porosity divided by the HR porosity.

	HR		DB			
Subunit	ϕ (%)	D	ϕ (%)	D	R_f	ΔD
MGLM-2	18.17	1.71	3.43	2.11	0.19	0.40
LGLM-3	21.00	1.74	7.83	1.98	0.37	0.24
LGLM-2	20.46	1.65	4.92	1.82	0.24	0.17
LGLM-1	23.08	1.59	5.59	1.75	0.24	0.16

incipient PSSs (Rustichelli et al., 2012). By comparing the different cores, the reduced grain size in MGLM-2 relative to the other DB cores is striking. It is primarily the size reduction seen in echinoderm fragments that contribute to the difference. Another key observation is the lack of sutured grain contacts within MGLM-2. Sutured grain contacts are clearly visible between larger echinoderm fragments within the three LGLM-1
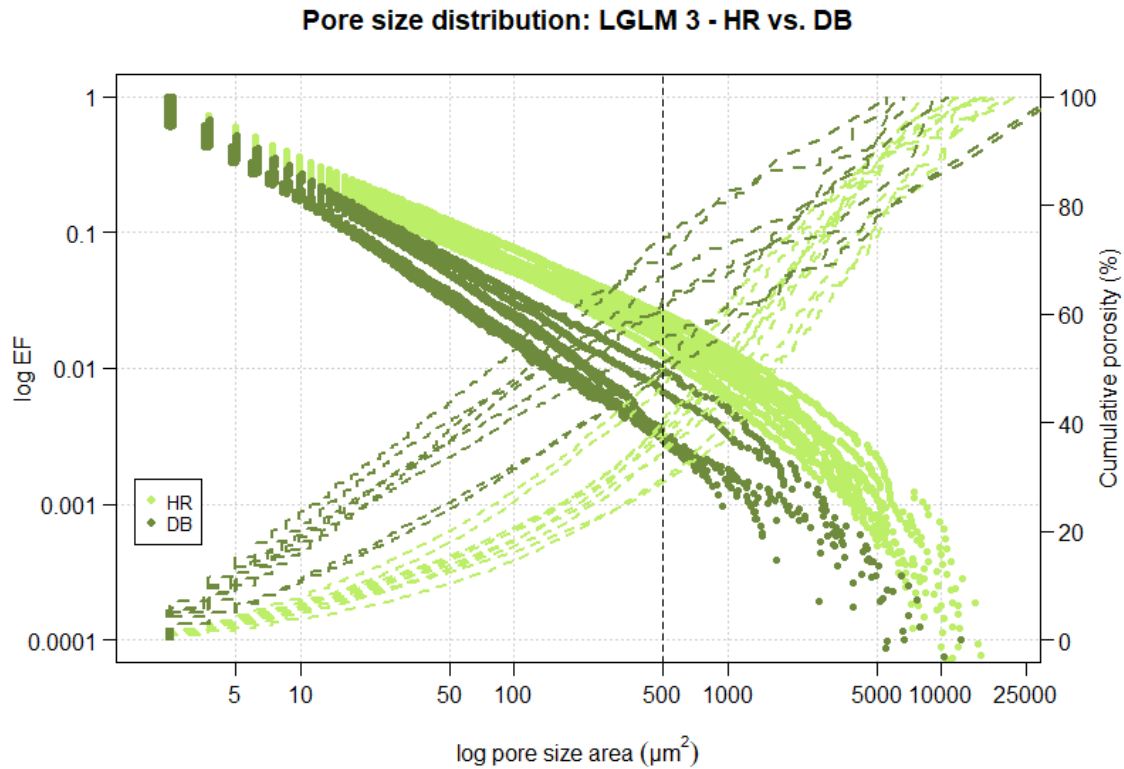
Figure 5.17: Pore-size distribution analysis of LGLM-3. Exceedence frequency (points) and cumulative porosity (dashed lines) is plotted against pore size (μm^2).

DB cores. Fractured foraminifera tests inside deformation bands can be seen in Figure 5.14a,b. Fractured foraminifera tests are rare, but easily recognized by the lack of preserved intraporosity due to infilling of matrix and cataclastic material. Examples of PSS and open fractures are found scattered in DBs across all units (Figure 5.14c,d).

Pore size distribution

Macropores observed within deformation bands in both LGLM and MGLM are consistently from intragranular pores of intact foraminifera tests. These intragranular pores account for most of the pore space inside deformation bands, but they do not represent available space for other grains to occupy during by granular flow. The amount of spherical intrapores in the MGLM-2 DB core in Figures 5.12b-c is comparably lower than what is observed in LGLM DBs (Figures 5.11b-c). By studying the binary porosity image in Figure 5.12c, the lack of intrapores could easily be attributed to a lower foraminifera-content, supporting the qualitative observations of a higher foraminifera-content in MGLM-2 (see Section 5.2.1). However, from the BSE-SEM image in 5.12b it does not seem to be the case. Intact foraminifera tests are present in the MGLM DB core, but relative to the foraminifera in LGLM, they contain comparably more
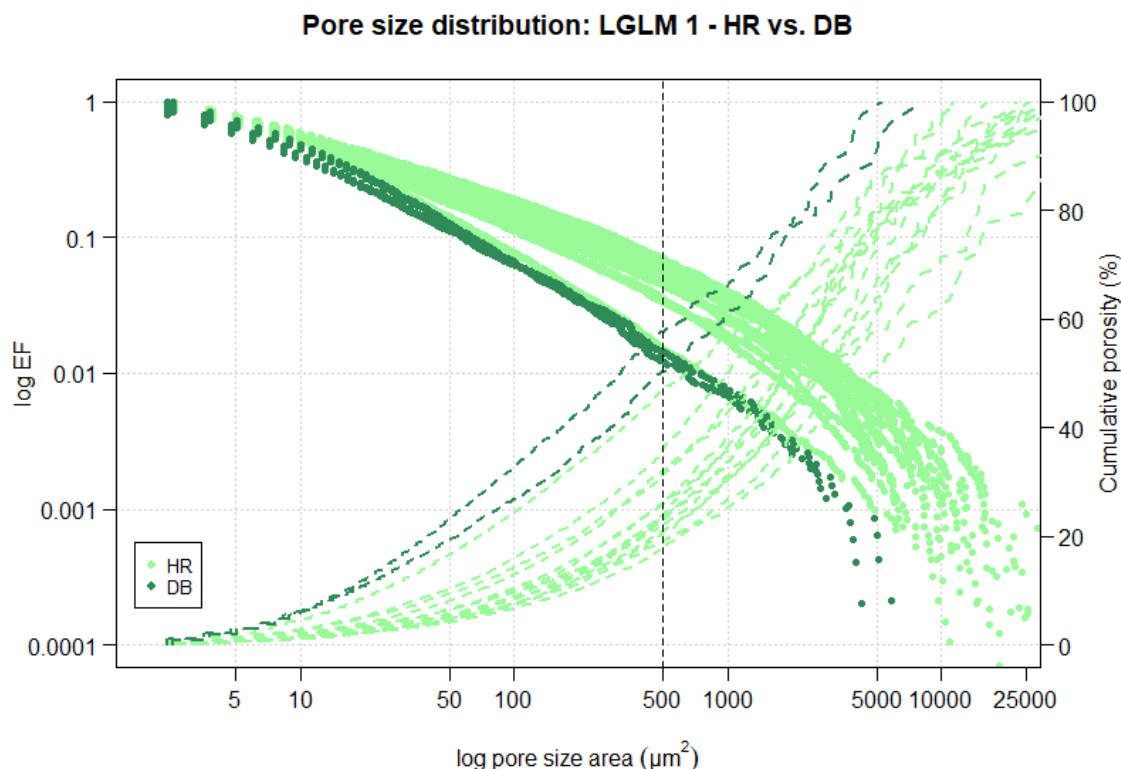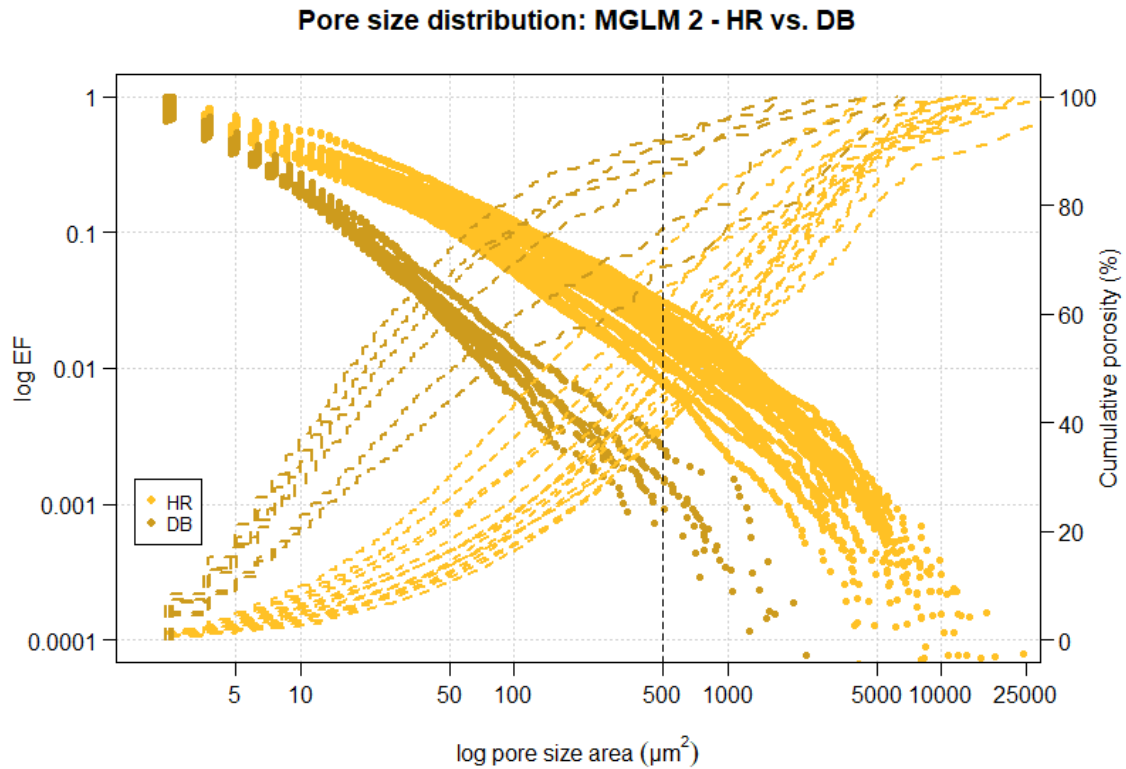
Figure 5.18: Pore-size distribution analysis of MGLM-2. Exceedence frequency (points) and cumulative porosity (dashed lines) is plotted against pore size (µm^2).

fine-grained matrix which suppresses the pore space (Figure 5.13).

The pore size distribution within DBs is compared to the host rock in Figures (5.15-5.18). Figures 5.19-5.20 compares the differences in pore size distribution of HR and DBs between the subunits seperately. Both the values and shape of the EF-curve for DB measurements differs significantly from the HR measurements in all units. There is an overall reduction in pore sizes within the DBs in all the studied DB-carrying subunits, identified by the left-shift of the EF-curves from HR (Figure 5.19) to DB (Figure 5.20). The EF-curves from DB measurements display a more linear shape, contrary to the curved shapes seen in the HR measurements. A power law has been calculated to fit the pore size distribution plots for each HR and DB measurement seen in Figures 5.15-5.18. The dimension D (exponent) of this power law can be used to compare different distributions, in this case EF. D is originally two dimensional, but by adding 1, it can be converted to the third dimension (Sammis et al., 1987; Blenkinsop, 1991). Table 5.4 lists the mean of converted D values for HR and DB measurements from all DB hosting subunits. Blenkinsop (1991) determined that the D value for grain size distributions correlated positively with increasing grain size reduction and cataclastic deformation. In the case of pore size distributions, a similar trend can be observed, where higher
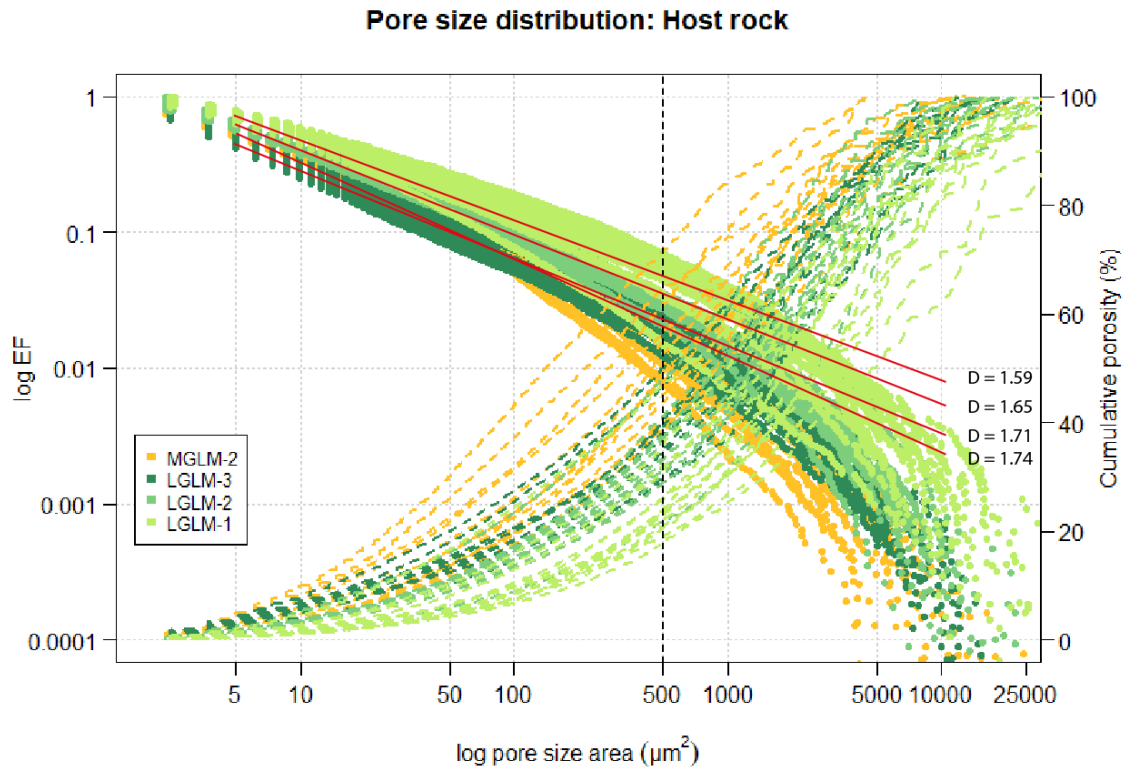
Figure 5.19: Pore-size distribution analysis for undeformed host rock of the DB-hosting subunits. Exceedence frequency (points) and cumulative porosity (dashed lines) is plotted against pore size (μm^2). The red lines correspond to the fitted power law, where the dimension (exponent) is given by the value D.

values of D correlates with greater pore size reduction. Although the overall grain size in the undeformed host rock of MGLM-2 is smaller when compared to LGLM, their D values are more or less the same. However, when looking at the change in D from HR to DB, (ΔD) is consistently higher for MGLM-2 (0.40) than in the three LGLM subunits (0.16, 0.17 and 0.24), indicating that the pore size reduction from HR to DB is greater in MGLM-2.

As for the cumulative porosity plots, they also show a shift leftwards, indicating a larger porosity contribution from smaller pores inside DBs than in the HR. For the cumulative porosity plots (with logarithmic x-axis), all HR-distributions from the subunits display a sigmoidal shape. Inside DBs, the cumulative porosity plots of all LGLM subunit display a more linear shape. The shape of the MGLM-2 distribution is more concave, showing a steep rise in porosity from pores up to around 200 μm^2, before stagnating. From 500 μm^2 and upwards, a new steep increase in porosity is observed. Values for the cumulative porosity at specific pore sizes can be found in Table 5.5. Looking at values from Table 5.5, pores below the micro-/ macroporosity treshold (500 μm^2) account for 84.5 % of the porosity in MGLM-2, compared to only
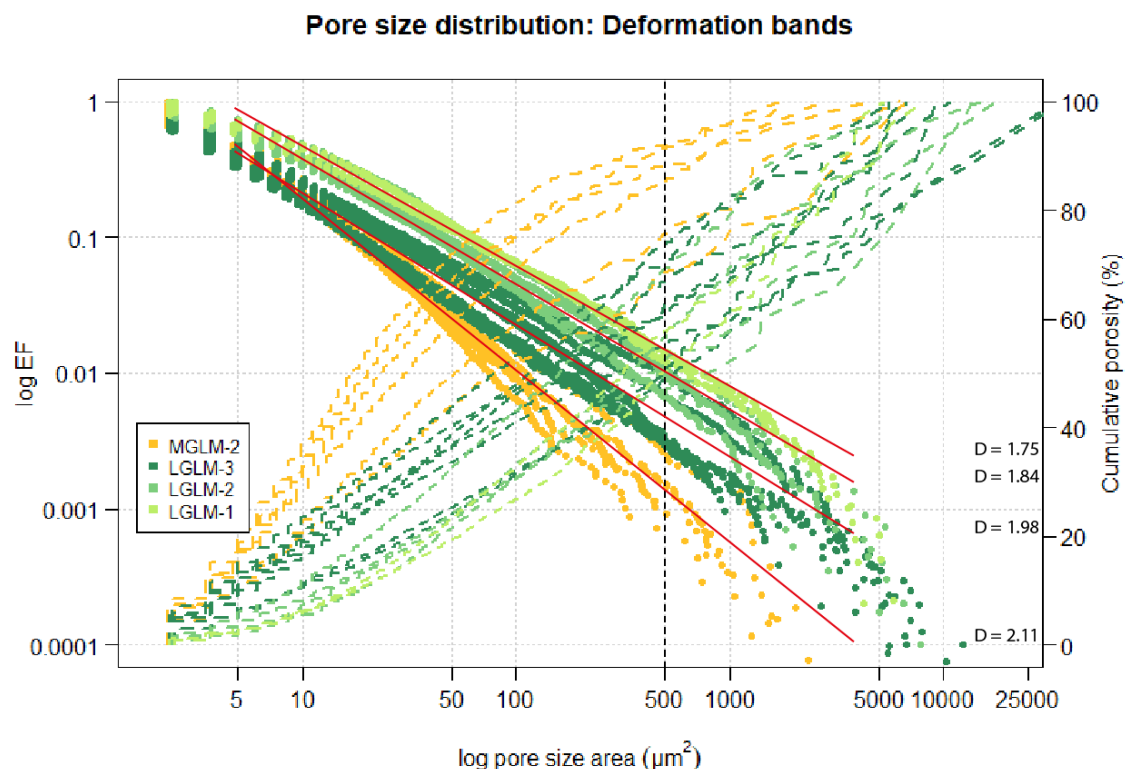
Figure 5.20: Pore-size distribution analysis from within deformation bands in the different subunits of the study area. Exceedence frequency (points) and cumulative porosity (dashed lines) is plotted against pore size (μm^2). The red lines correspond to the fitted power law, where the dimension (exponent) is given by the value D.

54.0 %, 56.4 % and 61.2 % for LGLM-1,-2, and -3.

Table 5.5: Mean values for cumulative porosity at specific pore sizes inside deformation bands from the different subunits. Plot of individual sample distributions can be seen in Figures 5.15-5.18.

Subunit	Pore size area				
	$10\,\mu m^2$	$50\,\mu m^2$	$500\,\mu m^2$	$5000\,\mu m^2$	$10\,000\,\mu m^2$
MGLM-2	28.4 %	59.2 %	83.5 %	98.6 %	100 %
LGLM-3	17.0 %	34.8 %	61.2 %	95.3 %	100 %
LGLM-2	8.0 %	25.3 %	56.4 %	86.2 %	94.2 %
LGLM-1	6.0 %	21.2 %	54.0 %	88.4 %	96.4 %

Chapter 6

Discussion

In this chapter, the results and observations from host rock and deformation band samples in the Lower and Middle Globigerina Limestone Members will be analysed to provide insight into the controls on deformation band nucleation. In what ways host rock characteristics control deformation band formation in carbonate grainstones will be discussed in detail. The first part of the chapter, Section 6.1, discusses the validity of the results given by two methods used to acquire pore size distributions, upon which a considerable part of the study is based. The next two sections, Sections 6.2 and 6.3, discusses two essential questions related to DB formation in the Globigerina Limestone Formation along the Maghlaq Fault:

1. Are there kinematic, mechanical or other differences in the DBs formed in LGLM and MGLM? (Section 6.2)

2. Why do DBs preferentially form in LGLM and not in MGLM? (Section 6.3)

The final section, Section 6.4, presents a proposed evolution history of the CSBs in LGLM and MGLM. Determining the controls on DB formation in this reservoir analogue could provide valuable insight into the deformation of porous carbonate grainstones in general.

6.1 Validity of the collected pore size distribution data

The pore size distribution plots seen in Section 5.2, allow for quantitative assessments of the effect that deformation band formation has on host rock of dissimilar compositions. Whereas previous studies on deformation bands in siliciclastics have quantified the degree of deformation through analysis of the grain size distribution (Torabi et al., 2007; Rotevatn et al., 2008; Cilona et al., 2012), the heterogenious composition of the

studied carbonate grainstone prevents the accurate measurement of grain sizes by digital image analysis. Instead, changes in the distribution of pore sizes have here been investigated in order to determine if a simlar correlation between the intensity of deformation and, in this case, pore sizes can be established. Cilona et al. (2012) analysed grain and pore size distribution on redrawn photomicrograhps of grainstones from Majella, Italy, but plotted the reverse of EF (% of pores/grains smaller than) as a function of sizes. In BSE-SEM images of carbonate grainstones from the Globigerina Limestone Formation, grain contacts are often sutured or show a minimal lack in contrast between bioclasts (as seen in figure 5.6), making it difficult for the DIA-software (ImageJ) to identify the extent of individual grains. A consequence of this would be that grain size distribution analysis would overestimate the presence of larger grains in the thin sections, as separate grains are interpreted as one, skewing the distribution plots. The contrast between grain and pores however, is easily detected by the software, making pore size ($>2\,\mu m$) the preferred parameter to investigate, rather than grain size.

The results of two methods, used to determine the relative proportions of pore sizes in the studied subunits, were presented in Section 5.2.1 of the results chapter. Although they both aim to determine the distribution of pore sizes in the host rock, the methods provide contradicting results. The results of the first method, seen in Figure 5.7, are based on first estimating the macroporosity from thin section photomicrographs and then estimating the combined macro and microporosity on BSE-SEM images. The second method (results seen in Figure 5.19) utilizes the data collected from porosity measurements on BSE-SEM images to plot pore size distribution curves for each subunit. The box plot (Figure 5.7) suggests that for MGLM-2, the macropores make up 87 % of the total estimated porosity. The cumulative porosity plots however (Figure 5.19), estimates that the macropores in MGLM-2 only account for 50 % of the total estimated porosity. For the LGLM subunits, the values derived from the host rock box plot and cumulative porosity plots are more similar, but still not close, with differences between the two methods ranging from 9 % to almost 25 % (Table 6.1).

What is interesting to note from the comparison of these methods, is that the difference in estimated porosity from these methods seems to reverse going stratigraphically upwards. For the lowermost unit, LGLM-1, the measurements from photomicrographs estimate the macroporosity proportion to be almost 25 % lower than what is observed in the cumulative porosity plot. This gap (Δ) decreases to 22.5 % for LGLM-2 and to 9.2 % for LGLM-3. For MGLM-2 the gap is reversed, with the cumulative porosity plot estimating a lower macroporosity than the photmicrographs ($\Delta = 36.3$ %). The fact that these methods contradict each other when it comes to the estimation of macroporosity, could be indicative of certain restrictions and shortcomings of the methods themselves. Whereas the the porosity estimation for the cumulative porosity plots is

based on BSE-SEM images with a high contrast between grains and pores, this is not the case for the estimation done on photomicrographs. Here, an increased amount of finer grained matrix in the sample can lead to overestimation of the porosity, due to lower contrasts between the blue epoxy and grains. This could explain why the macroporosity estimation on photomicrographs is significantly higher in the more distally deposited and more matrix rich subunits like MGLM-2. To summarise, the data shows that the estimation of relative proportions of pore sizes is more accurately given by the pore size distributions in Figure 5.19 and the listed mean values of the cumulative porosity plots in Table 6.1.

Table 6.1: The table shows the estimated macroporosity ($>500\,\mu m$) in the host rock of all DB-hosting subunits from two methods: (1) estimated macroporosity from photomicrographs, Figure 5.7 and Table 5.2, and (2) macroporosity derived from the cumulative porosity plots in Figure 5.19 and Table 5.3.

	Subunits			
Macroporosity from	LGLM-1	LGLM-2	LGLM-3	MGLM-2
Box plot (%)	49.0	42.9	52.8	86.7
Cumulative plot (%)	73.6	65.4	62.0	50.4
Δ (%)	-24.6	-22.5	-9.2	36.3

6.2 Dominating deformation mechanisms in LGLM and MGLM

In this section, observations and interpretations of the deformation mechanisms in deformation bands within LGLM and MGLM are discussed in order to answer the following question:

- Are there kinematic, mechanical or other differences in the DBs formed in LGLM and MGLM?

Microstructural observations indicate that different deformation mechanisms accommodated strain localisation during the formation of DBs in LGLM and MGLM. In terms of kinematics, all studied DBs in LGLM and MGLM were classified as compactional shear bands (CSBs), in agreement with observations of Rotevatn et al. (2016b). Bed-parallel, pure compaction bands (PCBs) at the outcrop were identified and sampled, but were not investigated as part of this project. By comparing DB cores seen in Figure 5.13, DBs from all three subunits of LGLM show similar characteristics with regards to grain assemblage and size, in contrast to the DB core from MGLM. The porosity reduction from HR to DB is slightly greater in LGLM-1 and LGLM-2 than

in LGLM-3, as shown in Table 5.4. Intragranular macropores from intact foraminifera inside LGLM-3 DBs account for the relatively higher measured porosity, relative to the bands in LGLM-2 and LGLM-3. Rustichelli et al. (2012) determined that the presence of intragranular micropores had no effect on the development of DBs, as these pores do not represent available space for other grains to occupy during compaction. Evidence of intergranular pressure solution between echinoderm fragments and pressure solution seams (PSS) are common throughout the DBs from the three subunits. This, combined with the lack of evidence for cataclasis, suggests that pressure solution has been a dominating deformation mechanisms during the formation of DBs in the LGLM.

One of the most prominent differences between the DB cores seen in Figure 5.13, is the finer grain size seen in the DB from MGLM-2. Bioclasts in the MGLM-2 are also more angular than equivalent grains in the LGLM. Very few examples of pressure solution between bioclasts have been observed in MGLM, indicating that pressure solution is less active mechanism for strain localisation in the subunit. As the grain fragments inside the DB are angular and that little evidence of pressure solution processes have been observed, a case can be made for cataclasis as being the dominant deformation mechanism in MGLM DBs.

The recorded porosity reduction from HR to DB in MGLM-2 is up to 1 order of magnitude (Table 5.4), which is more than what is commonly observed in disaggregation bands where the strain is accommodated purely by granular flow (Fossen et al., 2007). This indicates that another deformation mechanism has contributed to the porosity reduction seen in the DB. Rath et al. (2011) observed a porosity reduction of up to 1.5 orders of magnitude in cataclastic CSBs in a carbonate grainstone. By excluding the porosity contribution from the intragranular macropores from intact foraminifera, deemed not to affect the development of DBs by Rustichelli et al. (2012), the observed porosity reduction in MGLM-2 would be similar to that of the cataclastic DBs studied by Rath et al. (2011).

The data from the pore size distribution plots in Section 5.2.2 also indicate variations in the way strain is localised in the separate units. From the initial state of pore size distributions in the host rock (Figure 5.19) to deformation bands (Figure 5.20), the observed change in EF and cumulative porosity differs greatly between the subunits, suggesting that different modes, or intensities, of deformation mechanisms are driving the DB formation, or that the intensity of the deformation mechanisms vary between the subunits.

These findings are in agreement with Rotevatn et al. (2016b), who documented two types of compactional shear bands (CSBs) in the Globigerina Limestone Formation along the Maghlaq Fault; (i) Solution-dominated compactional shear bands (SCSB) and (ii) cataclais-dominated shear bands (CCSB). In addition to the identification of

the two types, we are here able to determine that the two types have originated in different members of the GLF.

6.3 Controlling factors on DB formation

As previously mentioned, deformation band frequency varies both between and within the subunits. The objective of this section is to discuss the following question related to the dissimilar distribution of DBs between the subunits:

- Why do DBs preferentially form in LGLM and not in MGLM?

To answer this question, acquired data and results will be discussed in light of previous studies. Four potential controlling factors are presented to explain the inter-subunit distribution of deformation bands: (i) Dominating deformation mechanism, (ii) Characteristics and variations in grain assemblage, (iii) pore size distribution within the subunits and (iv) post-depositional alterations of the host rock.

(i) Dominating deformation mechanism as a response to stress regime

Having established in Section 6.2 that there are different dominating deformation mechanisms driving the DB formation in LGLM (pressure solution) and MGLM (cataclasis), they could be a controlling factor behind the observed difference in DB frequency between the units. Cilona et al. (2012) showed that which deformation mechanisms dominated during strain localization in porous grainstones was strongly related to confining pressure. Disaggregation bands are believed to form under low confining pressures, and mechanisms of cataclasis or pressure solution is though to initiate at higher confining pressures Fossen et al. (2007). Baud et al. (2009) observed through laboratory experiments on carbonate grainstones that compactive shear bands in developed by granular flow and pore collapse at low confining pressure (5 MPa to 10 MPa), and that cataclasis is the dominant deformation mechanisms at high confining pressures (>10 MPa). Cilona et al. (2012) determined that natural compactive shear bands in grainstones from Majella, Italy, where formed under pressure conditions of <10 MPa, at depths shallower than 500 m. Seeing as MGLM is deposited on top of LGLM, it is unlikely that the two experienced significantly different confining pressures during burial, which never exceeded 300 m (Bonson et al., 2007). However, it is possible that pressure solution at echinoderm grain contacts in LGLM initiated at lower confining pressures than what was needed to enable cataclasis of bioclasts in MGLM. The smaller grain size in the MGLM may have promoted granular flow longer than what was possible in LGLM, where larger grain sizes would lead to an earlier onset of echinoderm grains interlocking, promoting PS. This hypothesis is explored further in Section 6.1. Another

explanation could be that the CSBs in LGLM and MGLM formed during separate tectonic (rifting) events with different stress fields. This hypothesis requires the pressure solution dominated CSBs in LGLM to have formed first, followd by lithification of the host rock. Subsequently, the second tectonic event formed the cataclastic CSBs in the overlying and less compacted MGLM. A strong case can be made against this hypothesis, with the first argument being that the overall orientation trend of CSBs in LGLM and MGLM are both ENE-WSW, indicating a similarly oriented stress field. The second argument is the lack of evidence for rifting events other than the development of the Maghlaq Fault, which is part of the regional Pantellaria Rift System, as documented by Bonson et al. (2007).

(ii) Grain assemblage and characteristics

Seeing as differences in both grain types, sizes and sphericity have been observed between the studied units, we here discuss whether these differences could affect strain localisation. Studies by Cheung et al. (2012); Rustichelli et al. (2012) have shown that in the grain assemblage, both in terms of bioclast type and size, is as a controlling factor on the development of DBs within a unit. Rustichelli et al. (2012) concluded that the skeletal grain assemblage of the host rock was one of the main controlling factors on the development of pressure solution in grainstone deformation bands. Like Rustichelli et al. (2012), Rotevatn et al. (2016b) found that pressure solution mainly developed at grain contacts of echinoderms, similar to what is observed in LGLM DBs here (see Section 5.2.2 and Figure 5.14). Less evidence for pressure solution is observed in DBs in MGLM, where the grain assemblage is characterised by overall more angular and smaller echinoderm fragments, both in the undeformed HR and inside DBs. The fact that less evidence for pressure solution is found within MGLM is in contrast to the findings of Rustichelli et al. (2012), who argued that finer grain sizes, along with better sorting and sphericity, promoted pressure solution processes.

Schultz et al. (2010) determined that the size of the plastic yield envelope during compaction banding in porous sandstones was inversely proportional to increased porosity and grain size, meaning compaction bands formed more easily in layers characterised by high porosities and large grain sizes. If transferred to grainstones, a similar correlation could be made for the observations of this study, where deformation bands are more frequent in the LGLM (higher porosity, coarser-grained) than MGLM (slightly lower porosity, finer-grained).

Another hypothesis to explain why deformation band formation prefers LGLM to MGLM-2 is the relatively higher proportion of foraminifera bioclasts in the host rock of MGLM-2. After investigating the test strength of different foraminifera, Wetmore (1987) concluded that the test shape had a bigger impact on the resistance of frac-

turing than morphology or composition. Rotevatn et al. (2016b) proposed that the spherical foraminifera tests in the Globigerina Limestone Fm. could withstand more stress without fracturing or being affected by pressure solution, compared to more angular and larger bioclast fragments of echinoderms. As seen in Figures 5.11-5.12, foraminifera test do remain more intact within the DBs relative to other bioclasts. A higher relative amount of foraminifera in the grain assemblage would mean a relatively lower amount of other bioclasts like echinoderms, which in turn would demote cataclasis and pressure solution. Less cataclasis and pressure solution due to changes in the foraminifera-content could thus explain why strain localisation in the form of DBs would prefer one lithology over another, seeing as cataclasis and pressure solution, in addition to granular flow, are considered the main deformation mechanisms driving DB formation in grainstones (Tondi et al., 2006; Cilona et al., 2012; Rotevatn et al., 2016b). As the higher foraminifera-content in MGLM has only been determined qualitatively from thin section photomicrographs (Section 5.2.1), concluding that the relative amount of foraminifera bioclasts is a controlling factor on whether DBs form in LGLM or MGLM is difficult without a quantitative analysis of the bioclast proportions. Nevertheless, the observations in this study do support that a higher DB frequencies are associated with a lower foraminifera-content.

(iii) Pore size distributions

Previous studies on deformation band formation have highlighted the relative proportions of macro- and micropores as controlling factors on strain localisation (Zhu et al., 2010; Rustichelli et al., 2012; Antonellini et al., 2014). A similar relationship is investigated here, by discussing the pore size distributions of the DB-hosting subunits within LGLM and MGLM from Section 5.2.2. The exceedence frequency and cumulative porosity plots show that MGLM-2 has a larger proportion of micropores, and that they account for a larger proportion of the total porosity within the subunit than what is observed in LGLM, where macroporosity and DB frequency is higher. This supports the conclusion from Rustichelli et al. (2012), that there is a positive relationship between the amount of macroporosity and the development of compactive deformation bands. However, Rustichelli et al. (2012) specified that it was the intergranular macroporosity which positively correlated with the formation of DBs. The software used to estimate the porosity in this study does not separate between intra- or intergranular macropores. This must be assessed qualitatively from BSE-SEM images in conjunction with interpretations of the pore size distribution plots. Figures 5.11-5.12 show that the largest pores, both in the HR and inside DBs, are consistently intragranular in both units. The figures also show that intergranular pores in LGLM are consistently larger than in MGLM.Cheung et al. (2012) found that pore collapse during deforma-

tion banding initiated at the larger pores in the host rock. A similar scenario can be proposed here, with more DBs developing in LGLM due to the larger pores.

Seeing as high levels of intergranular macroporosity is believed to promote DB formation, these observations suggests that the scarcity of bands in MGLM-2 could be explained by a relatively high proportion of *intra*granular macroporosity in the host rock. Similarly, the higher frequency of DBs in LGLM could thus be explained by a relatively high proportion of *inter*granular macroporosity.

(iv) Post-depositional factors

Given the same overall orientation trend for CSBs in all subunits, they are all interpreted to have developed under the same tectonic regime, in agreement with Rotevatn et al. (2016b). The depositional hiatus between LGLM and MGLM, during which the phosphorite conglomerate bed (MGLM-1) developed (Pedley et al., 1976), lasted for around 4 Ma during the early syn-rift period (Dart et al., 1993). Although the sediments of the Globigerina Limestone Formation were never buried more than 300 m (Bonson et al., 2007), differences in degree of cementation and compaction between the sediments of LGLM and MGLM at the time of DB formation could have affected which deformation mechanism that dominated. The differences in cement between the subunits could be controlled by timing, where pre-compactional cement growth would be expected to have developed further in the older subunits of LGLM, compared to the younger MGLM-2. Rustichelli et al. (2012) suggested that increased amounts of pre-compactional cements promoted deformation through pressure solution over physical compaction processes, as grains were cemented together which prevented compaction by granular flow. If the deformation bands in LGLM and MGLM were formed at the same time, with cement well developed in the lowermost subunits and less in the uppermost, DB's forming in LGLM would show evidence of more advanced deformation mechanisms (porosity reduction by pressure solution or cataclasis) than DB's in MGLM (porosity reduction by granular flow), according to Rath et al. (2011); Antonellini et al. (2014). This is supported by the observations in Figure 5.13 of the results chapter, where especially pressure solution at grain contacts is more abundant in LGLM 5.13 than in MGLM. However, the cementation of carbonate sediments deposited in shallow-marine environments often start right after deposition, according to Flügel (2004), and so the presence of cement in all subunits at the time of deformation seems likely. Also, cataclasis is in Section 6.2 proposed to have been one of the main deformation mechanisms accommodating strain in MGLM CSBs. On the basis of that, it seems more likely that cement was either equally distributed in LGLM and MGLM at the time of CSB formation and was not a significant controlling factor causing CSBs to preferentially form in LGLM.

6.4 Evolution of CSBs in LGLM and MGLM

The phosphoritic conglomerate bed (MGLM-1) separating the CSB-hosting MGLM-2 and LGLM does not contain any deformation bands. Determining the relative age of the two described types of CSBs on the basis of cross-cutting relations is therefore not possible. However, based on micro-structural observations and knowledge of the tectono-stratigraphic history of the study area, we propose that the CSBs in LGLM and MGLM formed in the same stress field, associated with growth of the Maghlaq Fault, but evolved differently over time due to differences in the host rock (see Figure 6.1). After deposition and the undeformed stage 1, CSB formation by granular flow was initiated (stage 2) at the same time in LGLM and MGLM, with induced stress from the extensional Maghlaq Fault. After further burial (stage 3) and increasing confining pressure, CSBs in LGLM began to accommodate strain by PS at grain contacts between large echinoderm fragments. Because of the lower echinoderm grain size in MGLM-2, less interlocking of PS-susceptible bioclasts took place, and granular flow was still the dominating deformation mechanism. At higher confining pressures in stage 4, compaction by granular flow was inhibited and strain was accommodated by cataclasis inside CSBs in MGLM-2, in agreement with Baud et al. (2009), wheras PS still dominated in LGLM. Because of the high amounts of stress needed to initiate cataclasis compared to PS, fewer CSBs were developed in MGLM-2. Although a plausible explanation for the evolution, large uncertainties remain around the relative age of the two CSB-types outcropping at the study area. For example, that PS initiates at lower confining pressures than cataclasis, in grainstones of exactly the same composition, has not been established through experiments.
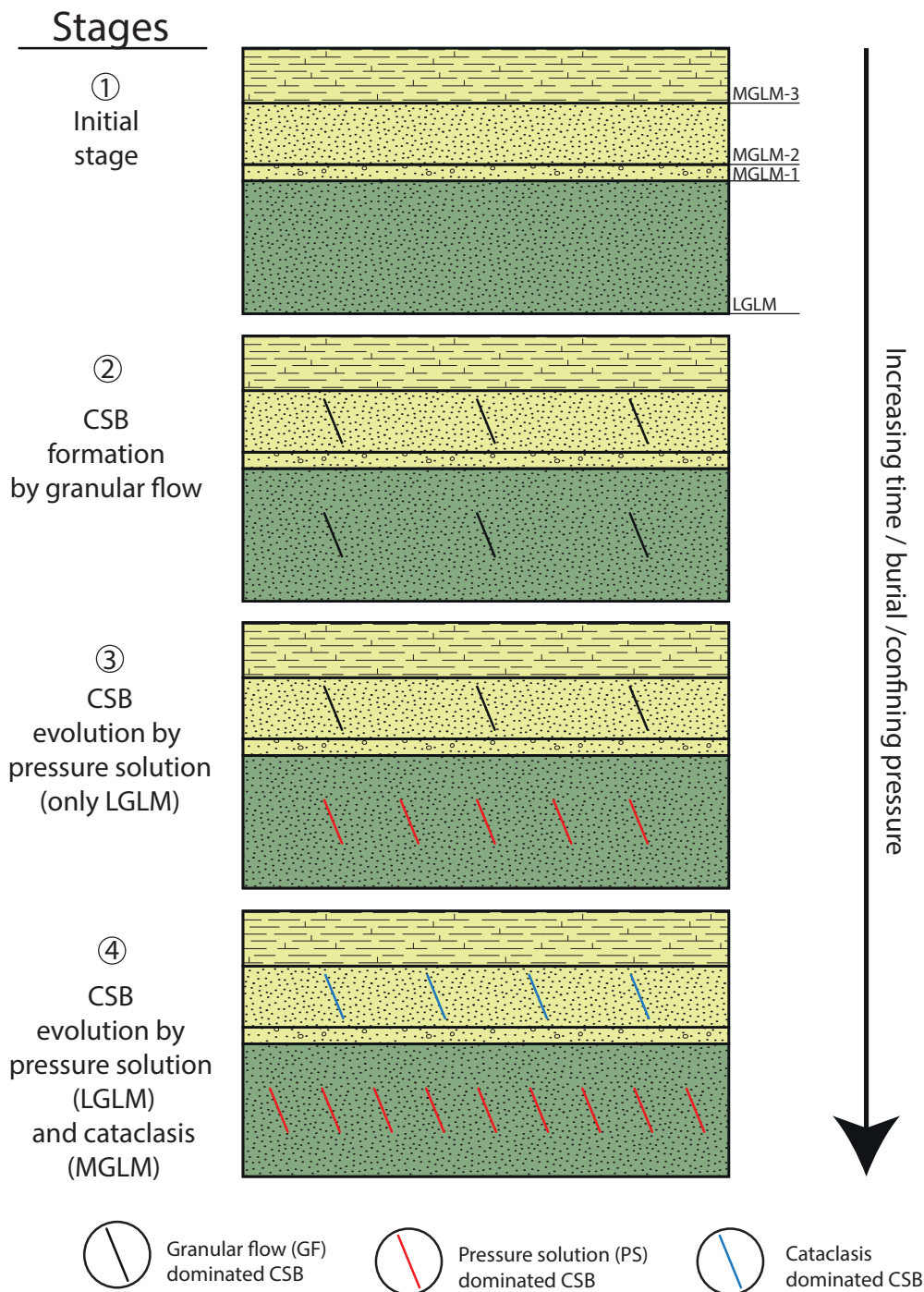
Figure 6.1: Sketch of the proposed, sequential evolution of CSBs within the grainstones of the Lower and Middle Globigerina Limestone Member. Four stages, at increasing burial, time and confining pressure, are highlighted: (1) initial state at the onset of burial. (2) CSBs form in LGLM and MGLM-2 by granular flow as a response to the activation of the normal Maghlaq Fault. (3) Pressure solution starts to initiate at grain contacts between larger echinoderm fragments inside LGLM CSBs, prompting the nucleation of more CSBs. The different characteristics of the MGLM-2 grain assemblage does not facilitate deformation by PS. (4) Increasing confining pressure and stress leads to the initiation of cataclasis as a mechanism for strain localisation in MGLM. PS solution is still driving the deformation in LGLM CSBs.

Chapter 7

Conclusions

The primary aim of this study has been to further investigate how deformation bands form and evolve in carbonate grainstones through outcrop observations and micro-analysis of host rock and deformation band samples from the outcropping Globigerina Limestone Formation in the hangingwall of the Maghlaq Fault, Malta. The conclusions of the study have been reached as a result of digital outcrop mapping by use of an UAV, acquisition of host rock and deformation band samples, thin section analysis by the use of optical and scanning electron microscopes and quantitative, statistical analysis on digitally acquired pore size data.

  i The studied units of the Globigerina Limestone Formation are classified as bioclastic grainstones to packstones with a host rock porosity of 18 - 23 %. Naturally occurring deformation bands have been described in three subunits of the Lower Globigerina Limestone Member and in one subunit of the overlying Middle Globigerina Member. All studied deformation bands have been classified as compactional shear bands (CSBs), with a dominating ENE-WSW orientation trend.

  ii Porosity reduction of up to 1 order of magnitude is observed from host rock to deformation band in the Globigerina Limestone Formation. Other studies of deformation band formation in carbonate grainstones have documented higher porosity reductions, but the relatively high porosity observed within CSBs in the studied units stems from the preservation of intrapores inside intact foraminifera tests, which have minimal effect on strain localisation.

  iii The exponent, D, of the fitted power law to the pore size distribution plots scales positively with increased pore size reduction of the host rock. The largest change in D, and so the largest pore size reduction from host rcok to deformation band, is found in the subunit MGLM-2.

  iv The CSBs formed in LGLM show evidence of different deformation mechanism than

what is observed in the overlying MGLM. Intergranular pressure solution processes and granular flow are thought to have been a more dominant deformation mechanism in the CSB formation in LGLM than in MGLM, where cataclasis combined with granular flow is thought to be the main facilitators for strain localisation.

v The CSBs in LGLM and MGLM initially formed in-concert by granular flow, in response to induced stress from the extensional Maghlaq Fault. Further, CSBs accumulated strain by pressure in LGLM at lower confining pressure, whereas pressure solution was less significant in MGLM-2 and cataclasis eventually developed when the confining pressure had increased further.

vi The preference of CSB nucleation in LGLM over MGLM can be attributed to a combination of the following controlling factors:

- Pressure solution is proposed to initiate at lower confining pressures than cataclasis. With pressure solution being the dominating deformation mechanism in LGLM, more CSBs have developed over time, in contrast to MGLM where cataclasis is believed to have initiated at a later stage, albeit in the same tectonic event.

- Higher recorded frequencies of CSBs seem to correlate with host rock characteristics of higher porosites and coarser grain sizes.

- A higher proportion of foraminifera bioclasts in the grain assemblage is here thought to demote pressure solution and cataclasis as mechanisms of strain localisation.

- A larger proportion of intergranular porosity in the host rock is thought to enhance the formation of CSBs.

- Pre-deformational cement is not believed to have been a controlling factor on the preferential formation of CSBs in LGLM over MGLM.

vii In addition to these findings, an important conclusion on the validity of the acquired pore size data used was also reached. Although pore size analysis using digital image analysis software on photomicrographs provides accurate results in well sorted sandstones, differentiation of micro- and macropores in matrix-containing grainstones is significantly more accurate when done on BSE-SEM images. The contrast between pores and matrix in photomicrographs is not distinct enough to enable the retrieval of reliable quantitative data.

Chapter 8

Future work

Field work

Using the high-resolution UAV-images collected during the field work of this project, detailed analysis and mapping of the deformation band networks on the outcrop units is possible. This could provide valuable insight into whether their formation was affected by other structural or lithological elements in the study area. The coastline parallel faults interpreted to be growth faults at the outcrop could also be interesting to investigate further. As they are recorded in the Lower Globigerina Limestone Formation, which according to the established stratigraphic interpretation of Malta was deposited pre-rifting, future studies could propose changes to the interpreted tectonic history of the Maltese Islands. The work to determine the time of nucleation and relative age of the recorded deformation bands could also benefit from further field work investigating the observed neptunian dykes at the outcrop. As neptunian dykes form in response to tectonic events, knowledge about their origin could shed a light on the timing of deformation band nucleation as well. This is particularly interesting as neptunian dykes only dissect the Lower Globigerina Limestone Member, not the Middle.

Microanalysis

A single sample from this project was run through a CT-scanner at the University of Bergen to investigate what data could be extracted using this method. In theory, the density contrast between deformation bands and the surrounding host rock allows for the production of a 3D model, revealing the intricate network of bands within a sample without damaging it. In the attempt associated with this study, a significant *beam hardening effect* (overestimation of the sample's outer rim density) prevented such a model to be produced. By applying a calcite filter to the CT-scanner, or by developing an algorithm to correct for beam hardening, a 3D model of the deformation network

could be produced. In such a model, identifying offsetting deformation bands would provide valuable information about the relative timing and evolution of deformation bands in the study area.

It could also be interesting for a future project to attempt to analyse the grain size distribution and the relative abundance of different bioclasts using DIA-software. This could have a significant impact on the understanding of which host rock properties enable the formation of deformation bands. Combining the pore size distribution data from this study with a dataset of grain size distributions from a future project could lead to an improved understanding of how the two parameters correlate in response to deformation. The results of such an analysis help to enhance the general knowledge about how carbonate grainstones deform.

Another method that could help determine the relative timing of the observed deformation mechanisms is the use of cathodoluminescence in conjuction with a scanning electron microscope. This method enables the identification of different cement generations inside the sampled thin sections. By determining the relative age of cements, this method could help deduce if the observed pressure solution in the samples occurred during a single or multiple events.

Abbreviations

Table 8.1: List of abbreviations used throughout the thesis (alphabetical order).

Abbreviation	Explanation
ϕ	Porosity
BSE-SEM	Scanning electron microscope with a backscatter elextron detector
CSB	Compactional shear band
D	Exponent of the fitted power law to pore size distribtion plots
DB	Deformation band
EF	Exceedence frequency
GF	Granular flow
GLF	Globigerina Limestone Formation
GSD	Grain size distribution
HR	Host rock
LGLM	Lower Globigerina Member
MF	Maghlaq Fault
MGLM	Middle Globigerina Member
OM	Optical microscope
PS	Pressure solution
PSD	Pore size distribution
PSS	Pressure solution seam
R_f	Reduction factor
UAV	Unmanned aerial vehicle

Bibliography

Anselmetti, F., Luthi, S., and Eberli, G. (1998). Quantitative characterization of carbonate pore systems by digital image analysis. 82:1815–1836.

Antonellini, M. and Aydin, A. (1994). Effect of faulting on fluid flow in porous sandstones; petrophysical properties. *AAPG Bulletin*, 78(3):355.

Antonellini, M., Petracchini, L., Billi, A., and Scrocca, D. (2014). First reported occurrence of deformation bands in a platform limestone, the jurassic calcare massiccio fm., northern apennines, italy. *Tectonophysics*, 628:85–104.

Antonellini, M. A., Aydin, A., and Pollard, D. D. (1994). Microstructure of deformation bands in porous sandstones at arches national park, Utah. *Journal of Structural Geology*, 16(7):941–959.

Argnani, A. (1990). The strait of sicily rift zone: Foreland deformation related to the evolution of a back-arc basin. *Journal of Geodynamics*, 12(2):311–331.

Aydin, A. (1978). Small faults formed as deformation bands in sandstone. *pure and applied geophysics*, 116(4):913–930.

Aydin, A., Borja, R. I., and Eichhubl, P. (2006). Geological and mathematical framework for failure modes in granular rock. *Journal of Structural Geology*, 28(1):83 – 98.

Aydin, A. and Johnson, A. M. (1978). Development of faults as zones of deformation bands and as slip surfaces in sandstone. *pure and applied geophysics*, 116(4):931–942.

Baldassini, N. and Di Stefano, A. (2017). Stratigraphic features of the maltese archipelago: a synthesis. *Natural Hazards*, 86(2):203–231.

Ballas, G., Fossen, H., and Soliva, R. (2015). Factors controlling permeability of cataclastic deformation bands and faults in porous sandstone reservoirs. *Journal of Structural Geology*, 76:1 – 21.

Baud, P., Vinciguerra, S., David, C., Cavallo, A., Walker, E., and Reuschlé, T. (2009). Compaction and failure in high porosity carbonates: Mechanical data and microstructural observations. *Pure and Applied Geophysics*, 166(5):869–898.

Blenkinsop, T. G. (1991). Cataclasis and processes of particle size reduction. *pure and applied geophysics*, 136(1):59–86.

Bonson, C. G., Childs, C., Walsh, J. J., Schöpfer, M. P. J., and Carboni, V. (2007). Geometric and kinematic controls on the internal structure of a large normal fault in massive limestones: The maghlaq fault, malta. *Journal of Structural Geology*, 29(2):336–354.

Cashman, S. and Cashman, K. (2000). Cataclasis and deformation-band formation in unconsolidated marine terrace sand, humboldt county, california. *Geology*, 28(2):111.

Chen, L., Xu, J., and Chen, J. (2015). Applications of scanning electron microscopy in earth sciences. *Science China Earth Sciences*, 58(10):1768–1778.

Cheung, C. S. N., Baud, P., and Wong, T.-f. (2012). Effect of grain size distribution on the development of compaction localization in porous sandstone. *Geophysical Research Letters*, 39(21):n/a–n/a. L21302.

Choquette, P. W. and Pray, L. C. (1970). Geologic nomenclature and classification of porosity in sedimentary carbonates. *AAPG Bulletin*, 54(2):207.

Cilona, A., Baud, P., Tondi, E., Agosta, F., Vinciguerra, S., Rustichelli, A., and Spiers, C. J. (2012). Deformation bands in porous carbonate grainstones: Field and laboratory observations. *Journal of Structural Geology*, 45:137–157.

Dart, C. J., Bosence, D. W. J., and McClay, K. R. (1993). Stratigraphy and structure of the maltese graben system. *Journal of the Geological Society*, 150(6):1153–1166.

Dewey, J. F., Helman, M. L., Knott, S. D., Turco, E., and Hutton, D. H. W. (1989). Kinematics of the western mediterranean. *Geological Society, London, Special Publications*, 45(1):265–283.

Du Bernard, X., Eichhubl, P., and Aydin, A. (2002). Dilation bands: A new form of localized failure in granular media. *Geophysical Research Letters*, 29(24):29–1–29–4. 2176.

Dunham, R. J. (1962). Classification of carbonate rocks according to depositional textures. *American Association of Petroleum Geologists Memoir*, 1.

Felix, R. (1973). *Oligo-Miocene Stratigraphy of Malta and Gozo*, volume 73. Veenman Wageningen.

Fisher, Q. and Knipe, R. (2001). The permeability of faults within siliciclastic petroleum reservoirs of the north sea and norwegian continental shelf. *Marine and Petroleum Geology*, 18(10):1063 – 1081.

Flügel, E. (2004). *Microfacies of Carbonate Rocks. Analysis, Interpretation and Application.* Springer-Verlag Berlin, Heidelberg, New York.

Folk, R. L. (1959). Practical petrographic classification of limestones. *AAPG Bulletin*, 43(1):1–38.

Fossen, H. and Bale, A. (2007). Deformation bands and their influence on fluid flow. *AAPG Bulletin*, 91(12):1685–1700.

Fossen, H. and Rotevatn, A. (2012). Characterization of deformation bands associated with normal and reverse stress states in the navajo sandstone, utah: Discussion. *AAPG Bulletin*, 96(5):869–876.

Fossen, H., Schultz, R., Shipton, Z., and Mair, K. (2007). Deformation bands in sandstone: a review. *Journal of the Geological Society*, 164:755–769.

Fossen, H., Soliva, R., Ballas, G., Trzaskos, B., Cavalcante, C., and Schultz, R. A. (2017). A review of deformation bands in reservoir sandstones: geometries, mechanisms and distribution. *Geological Society, London, Special Publications*, 459:9–33.

Fossmark, H. S. S. (2015). Petrophysical properties of deformation bands and their influence on fluid flow in carbonate grainstones: insights from the maghlaq fault, malta. Msc thesis, University of Bergen.

Gibson, R. G. (1998). Physical character and fluid-flow properties of sandstone-derived fault zones. *Geological Society, London, Special Publications*, 127(1):83.

Gruszczyński, M., Marshall, J. D., Goldring, R., Coleman, M. L., Małkowski, K., Gaździcka, E., Semil, J., and Gatt, P. (2008). Hiatal surfaces from the miocene globigerina limestone formation of malta: Biostratigraphy, sedimentology, trace fossils and early diagenesis. *Palaeogeography, Palaeoclimatology, Palaeoecology*, 270(3):239–251.

Gueguen, E., Doglioni, C., and Fernandez, M. (1998). On the post-25 ma geodynamic evolution of the western mediterranean. *Tectonophysics*, 298(1):259–269.

Hesthammer, J. and Fossen, H. (2001). Structural core analysis from the gullfaks area, northern north sea. *Marine and Petroleum Geology*, 18(3):411 – 439.

Illies, J. H. (1981). Graben formation — the maltese islands — a case history. *Tectonophysics*, 73(1):151–168.

Jongsma, D., van Hinte, J. E., and Woodside, J. M. (1985). Geologic structure and neotectonics of the north african continental margin south of sicily. *Marine and Petroleum Geology*, 2(2):156–179.

Kanaya, K. and Okayama, S. (1972). Penetration and energy-loss theory of electrons in solid targets. *Journal of Physics D: Applied Physics*, 5(1):43–58.

Knipe, R. J., Fisher, Q. J., Jones, G., Clennell, M. R., Farmer, A. B., Harrison, A., Kidd, B., McAllister, E., Porter, J. R., and White, E. A. (1997). *Fault seal analysis: successful methodologies, application and future directions*, volume 7, pages 15–38. Elsevier.

Lonergan, L. and White, N. (1997). Origin of the betic-rif mountain belt. *Tectonics*, 16(3):504–522.

Pedley, H. M. (1978). A new lithostratigraphical and palaeoenvironmental interpretation for the coralline limestone formations (miocene) of the maltese islands. *Overseas Geology & Mineral Resources*, 54:18.

Pedley, H. M. and Bennett, S. M. (1985). Phosphorites, hardgrounds and syndepositional solution subsidence: A palaeoenvironmental model from the miocene of the maltese islands. *Sedimentary Geology*, 45(1):1–34.

Pedley, H. M., House, M. R., and Waugh, B. (1976). The geology of malta and gozo. *Proceedings of the Geologists' Association*, 87(3):325–341.

Pedley, H. M. and Moores, E. M. (1997). *Malta*, book section 68, pages 535–537. Springer Netherlands, Dordrecht.

Rath, A., Exner, U., Tschegg, C., Grasemann, B., Laner, R., and Draganits, E. (2011). Diagenetic control of deformation mechanisms in deformation bands in a carbonate grainstone. *AAPG Bulletin*, 95(8):1369–1381.

Rosenbaum, G., Lister, G., and Duboz, C. (2002). Reconstruction of the tectonic evolution of the western mediterranean since the oligocene. *Journal of the Virtual Explorer*, 8:107–130.

Rotevatn, A. and Fossen, H. (2011). Simulating the effect of subseismic fault tails and process zones in a siliciclastic reservoir analogue: Implications for aquifer support and trap definition. *Marine and Petroleum Geology*, 28(9):1648–1662.

Rotevatn, A., Fossmark, H. S., Bastesen, E., Thorsheim, E., and Torabi, A. (2016a). Do deformation bands matter for flow? insights from permeability measurements and flow simulations in porous carbonate rocks. *Petroleum Geoscience*.

Rotevatn, A., Thorsheim, E., Bastesen, E., Fossmark, H. S. S., Torabi, A., and Sælen, G. (2016b). Sequential growth of deformation bands in carbonate grainstones in the hangingwall of an active growth fault: Implications for deformation mechanisms in different tectonic regimes. *Journal of Structural Geology*, 90:27–47.

Rotevatn, A., Torabi, A., Fossen, H., and Braathen, A. (2008). Slipped deformation bands: A new type of cataclastic deformation bands in western sinai, suez rift, egypt. *Journal of Structural Geology*, 30(11):1317–1331.

Rotevatn, A., Tveranger, J., Howell, J. A., and Fossen, H. (2009). Dynamic investigation of the effect of a relay ramp on simulated fluid flow: geocellular modelling of the delicate arch ramp, utah. *Petroleum Geoscience*, 15(1):45–58.

Royden, L. H. (1993). Evolution of retreating subduction boundaries formed during continental collision. *Tectonics*, 12(3):629–638.

Rustichelli, A., Tondi, E., Agosta, F., Cilona, A., and Giorgioni, M. (2012). Development and distribution of bed-parallel compaction bands and pressure solution seams in carbonates (bolognano formation, majella mountain, italy). *Journal of Structural Geology*, 37(Supplement C):181–199.

Sammis, C., King, G., and Biegel, R. (1987). The kinematics of gouge deformation. *pure and applied geophysics*, 125(5):777–812.

Schneider, C. A., Rasband, W. S., and Eliceiri, K. W. (2012). Nih image to imagej: 25 years of image analysis. *Nature methods*, 9(7):671.

Schultz, R. and Siddharthan, R. (2005). A general framework for the occurrence and faulting of deformation bands in porous granular rocks. *Tectonophysics*, 411(1):1 – 18.

Schultz, R. A., Okubo, C. H., and Fossen, H. (2010). Porosity and grain size controls on compaction band formation in jurassic navajo sandstone. *Geophysical Research Letters*, 37(22).

Seeger, A., Duci, A., and Haussecker, H. (2006). Scanning electron microscope charging effect model for chromium/quartz photolithography masks. *Scanning*, 28(3):179–186.

Sim, K. S., Tan, Y. Y., Lai, M. A., Tso, C. P., and Lim, W. K. (2010). Reducing scanning electron microscope charging by using exponential contrast stretching technique on post-processing images. *Journal of Microscopy*, 238(1):44–56.

Soliva, R., Schultz, R. A., Ballas, G., Taboada, A., Wibberley, C., Saillet, E., and Benedicto, A. (2013). A model of strain localization in porous sandstone as a function of tectonic setting, burial and material properties; new insight from provence (southern france). *Journal of Structural Geology*, 49:50 – 63.

Sternlof, K. R., Karimi-Fard, M., Pollard, D. D., and Durlofsky, L. J. (2006). Flow and transport effects of compaction bands in sandstone at scales relevant to aquifer and reservoir management. *Water Resources Research*, 42(7):n/a–n/a. W07425.

Thorsheim, E. (2015). The geometry and evolution of deformation bands in carbonate grainstones along the maghlaq fault, malta. Msc thesis, University of Bergen.

Tondi, E. (2007). Nucleation, development and petrophysical properties of faults in carbonate grainstones: Evidence from the san vito lo capo peninsula (sicily, italy). *Journal of Structural Geology*, 29(4):614–628.

Tondi, E., Antonellini, M., Aydin, A., Marchegiani, L., and Cello, G. (2006). The role of deformation bands, stylolites and sheared stylolites in fault development in carbonate grainstones of majella mountain, italy. *Journal of Structural Geology*, 28(3):376–391.

Torabi, A., Braathen, A., Cuisiat, F., and Fossen, H. (2007). Shear zones in porous sand: Insights from ring-shear experiments and naturally deformed sandstones. *Tectonophysics*, 437(1):37 – 50.

Torabi, A. and Fossen, H. (2009). Spatial variation of microstructure and petrophysical properties along deformation bands in reservoir sandstones. *AAPG Bulletin*, 93(7):919–938.

Torabi, A., Fossen, H., and Braathen, A. (2013). Insight into petrophysical properties of deformed sandstone reservoirspetrophysical properties. *AAPG Bulletin*, 97(4):619–637.

Ujiie, K., Maltman, A. J., and Sánchez-Gómez, M. (2004). Origin of deformation bands in argillaceous sediments at the toe of the nankai accretionary prism, southwest japan. *Journal of Structural Geology*, 26(2):221 – 231.

Vajdova, V., Baud, P., and Wong, T.-f. (2004). Compaction, dilatancy, and failure in porous carbonate rocks. *Journal of Geophysical Research: Solid Earth*, 109(B5).

Vajdova, V., Baud, P., Wu, L., and fong Wong, T. (2012). Micromechanics of inelastic compaction in two allochemical limestones. *Journal of Structural Geology*, 43:100 – 117.

Wennberg, O. P., Casini, G., Jahanpanah, A., Lapponi, F., Ineson, J., Wall, B. G., and Gillespie, P. (2013). Deformation bands in chalk, examples from the shetland group of the oseberg field, north sea, norway. *Journal of Structural Geology*, 56:103–117.

Wetmore, K. L. (1987). Correlations between test strength, morphology and habitat in some benthic foraminifera from the coast of washington. *Journal of Foraminiferal Research*, 17(1):1.

Wong, T., David, C., and Zhu, W. The transition from brittle faulting to cataclastic flow in porous sandstones: Mechanical deformation. *Journal of Geophysical Research: Solid Earth*, 102(B2):3009–3025.

Zhu, W., Baud, P., and Wong, T. (2010). Micromechanics of cataclastic pore collapse in limestone. *Journal of Geophysical Research: Solid Earth*, 115(B4).

Appendices

Appendix A

Previous work
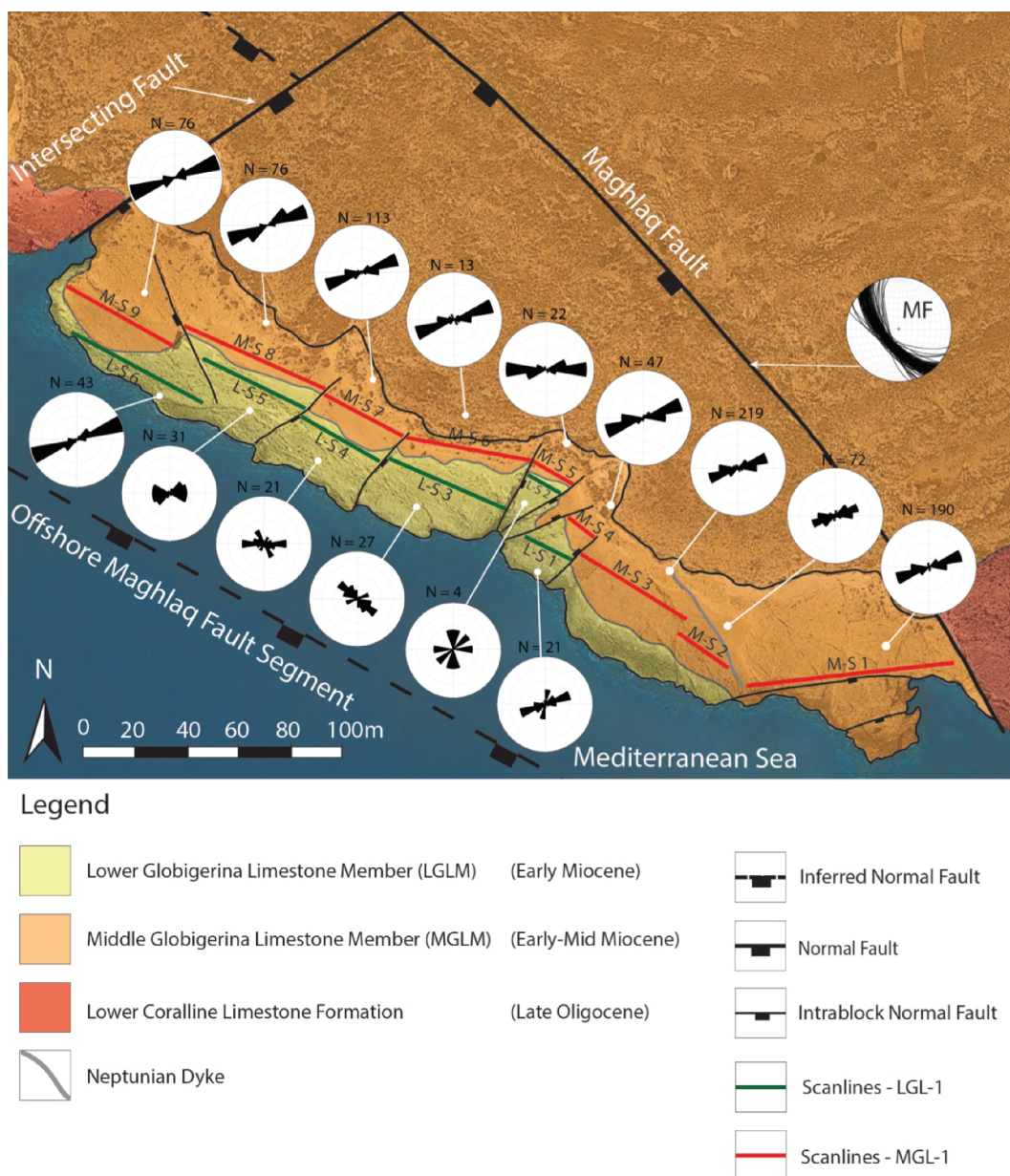
Figure 1: Map of the study area with inferred scanlines and deformation band orientation trends plotted as rose diagrams by Thorsheim (2015). The stratigraphic boundaries between the Lower and Middle Globigerina Limestone Formation have been reinterpreted as part of this thesis.
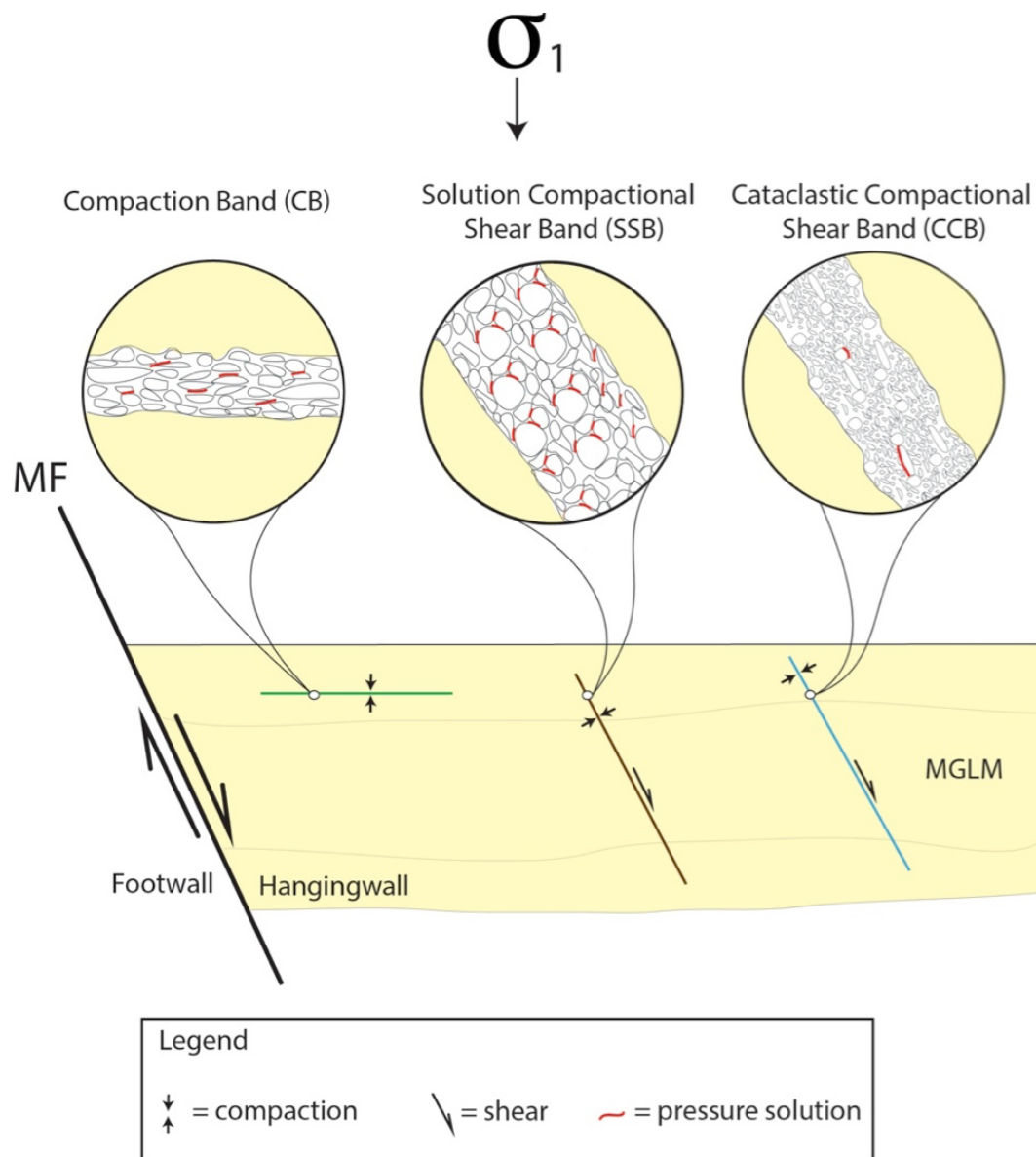
Figure 2: Conceptual sketch showing the three types of bands classified by Thorsheim (2015) – bed-parallel compaction bands (CB), high-angle to bedding solution compactional shear bands (SSB) and high-angle to bedding cataclastic compactional shear bands (CSB).

Appendix B

Tables and measurements

Porosity measurements

Host rock

Table 2: Parameters and results from porosity estimation on BSE-SEM images.

SampleID	ImageID	Subunit	Scale (px/µm)	Magnification	Porosity
DB-1	DB-1-28.tif	LGLM-3	0.3688	133	24.27
DB-1	DB-1-40.tif	LGLM-3	0.8883	161	25.24
DB-1	DB-1-42.tif	LGLM-3	0.8983	162	19.66
DB-1	DB-1-43.tif	LGLM-3	0.8883	161	21.08
DB-1	DB-1-45.tif	LGLM-3	0.9183	162	26.59
DB-3	DB-3-01.tif	LGLM-2	0.8883	160	23.14
DB-3	DB-3-05.tif	LGLM-2	0.8883	160	15.45
DB-3	DB-3-07.tif	LGLM-2	0.8883	160	21.86
DB-3	DB-3-11.tif	LGLM-2	0.8983	161	18.13
DB-3	DB-3-12.tif	LGLM-2	0.8983	161	24.10
DB-3	DB-3-13.tif	LGLM-2	0.8983	161	22.70
DB-3	DB-3-14.tif	LGLM-2	0.9183	165	19.04
DB-3	DB-3-15.tif	LGLM-2	0.8983	161	23.13
DB-3	DB-3-16.tif	LGLM-2	0.8983	161	22.75
DB-5	DB-5-1-01.tif	LGLM-2	0.8983	161	18.68
DB-5	DB-5-1-05.tif	LGLM-2	0.8983	161	16.82
DB-5	DB-5-1-06.tif	LGLM-2	0.8983	161	19.61
DB-5	DB-5-1-10.tif	LGLM-2	0.8983	161	20.62
DB-7	DB-7-01.tif	MGLM-2	0.8983	161	16.84
DB-7	DB-7-02.tif	MGLM-2	0.8983	161	19.70
DB-7	DB-7-03.tif	MGLM-2	0.8983	161	14.99

Table 2 continued from previous page

SampleID	ImageID	Subunit	Scale (px/µm)	Magnification	Porosity
DB-7	DB-7-04.tif	MGLM-2	0.8983	161	16.20
DB-7	DB-7-07.tif	MGLM-2	0.9183	166	17.13
DB-7	DB-7-08.tif	MGLM-2	0.9183	166	20.54
DB-7	DB-7-12.tif	MGLM-2	0.8983	161	19.89
DB-7	DB-7-16.tif	MGLM-2	0.8983	161	22.84
DB-7	DB-7-85.tif	MGLM-2	0.8983	161	23.41
DB-7	DB-7-87.tif	MGLM-2	0.8883	160	16.32
DB-7	DB-7-96.tif	MGLM-2	0.8983	161	18.39
DB-12	DB-12-2-04.tif	LGLM-2	0.9083	163	13.33
DB-12	DB-12-2-05.tif	LGLM-2	0.9083	163	10.36
DB-12	DB-12-2-82.tif	LGLM-2	0.8983	161	10.24
DB-13	DB-13-1-01.tif	LGLM-1	0.8983	161	20.28
DB-13	DB-13-1-05.tif	LGLM-1	0.8883	160	20.42
DB-13	DB-13-1-12.tif	LGLM-1	0.8983	161	21.47
DB-13	DB-13-1-14.tif	LGLM-1	0.8983	161	20.98
DB-13	DB-13-1-15.tif	LGLM-1	0.8983	161	22.81
DB-13	DB-13-1-16.tif	LGLM-1	0.8983	161	19.15
DB-13	DB-13-1-17.tif	LGLM-1	0.8983	161	20.20
HR-2	HR-2-01.tif	LGLM-1	0.8883	159	21.89
HR-2	HR-2-02.tif	LGLM-1	0.8783	157	28.44
HR-2	HR-2-03.tif	LGLM-1	0.8783	157	21.83
HR-2	HR-2-04.tif	LGLM-1	0.8783	157	27.16
HR-2	HR-2-05.tif	LGLM-1	0.8983	161	22.61
HR-2	HR-2-06.tif	LGLM-1	0.8983	161	25.28
HR-2	HR-2-07.tif	LGLM-1	0.8983	161	30.57
HR-3	HR-3-08.tif	MGLM-2	0.8983	161	13.68
HR-3	HR-3-09.tif	MGLM-2	0.8983	161	13.14
HR-3	HR-3-10.tif	MGLM-2	0.8983	161	15.18
HR-3	HR-3-11.tif	MGLM-2	0.8983	161	11.64
HR-3	HR-3-12.tif	MGLM-2	0.8983	161	19.52
HR-5	HR-5-06.tif	LGLM-3	0.8983	161	16.77
HR-5	HR-5-07.tif	LGLM-3	0.8983	161	17.57
HR-5	HR-5-08.tif	LGLM-3	0.8983	161	15.68
HR-5	HR-5-09.tif	LGLM-3	0.8983	161	15.71
HR-5	HR-5-10.tif	LGLM-3	0.8983	161	20.08

Table 2 continued from previous page

SampleID	ImageID	Subunit	Scale (px/µm)	Magnification	Porosity
HR-6	HR-6-01.tif	MGLM-3	0.8983	161	17.14
HR-6	HR-6-02.tif	MGML-3	0.8983	161	11.77
HR-6	HR-6-03.tif	MGLM-4	0.8983	161	13.41
HR-6	HR-6-04.tif	MGML-4	1.6767	301	16.58
HR-6	HR-6-05.tif	MGLM-5	1.6767	301	16.72
HR-6	HR-6-06.tif	MGML-5	1.6767	301	16.70
HR-6	HR-6-08.tif	MGLM-6	0.8983	161	12.14
HR-6	HR-6-09.tif	MGML-6	1.6767	301	16.61
HR-6	HR-6-10.tif	MGLM-7	0.8983	161	11.54
HR-6	HR-6-11.tif	MGML-7	1.6767	301	17.46
HR-6	HR-6-12.tif	MGLM-8	0.8983	161	12.48
HR-6	HR-6-13.tif	MGML-8	1.6767	301	17.36

Deformation bands

Table 3: Parameters and results from porosity estimation on BSE-SEM images.

SampleID	ImageID	Subunit	Scale (px/µm)	Magnification	Porosity
DB-1-1	3	LGLM-3	0.9175	161	24.27
DB-1-1	8	LGLM-3	0.8975	161	25.24
DB-1-1	11	LGLM-3	1.6567	301	19.66
DB-1-1	12	LGLM-3	1.6567	301	21.08
DB-1-1	13	LGLM-3	1.6567	301	26.59
DB-1-2	2	LGLM-3	0.8983	161	23.14
DB-1-2	5	LGLM-3	0.8983	161	15.45
DB-2-2	3	LGLM-3	0.8983	161	21.86
DB-2-2	4	LGLM-3	0.8983	161	18.13
DB-2-2	8	LGLM-3	0.8875	160	24.10
DB-2-2	9	LGLM-3	0.8875	160	22.70
DB-3	3	LGLM-2	0.8883	160	19.04
DB-3	9	LGLM-2	0.8983	161	23.13
DB-3	17	LGLM-2	1.6767	301	22.75
DB-3	18	LGLM-2	1.6767	301	18.68
DB-3	19	LGLM-2	1.6767	301	16.82
DB-5-1	3	LGLM-2	0.8983	161	19.61
DB-5-2	8	LGLM-2	0.8983	161	20.62

Table 3 continued from previous page

SampleID	ImageID	Subunit	Scale (px/µm)	Magnification	Porosity
DB-7	88	MGLM-2	0.8883	160	16.84
DB-7	89	MGLM-2	0.8883	160	19.70
DB-7	90	MGLM-2	0.8883	160	14.99
DB-7	94	MGLM-2	0.8983	161	16.20
DB-7	95	MGLM-2	0.8983	161	17.13
DB-7	5	MGLM-2	0.9183	166	20.54
DB-7	17	MGLM-2	1.6767	301	19.89
DB-7	18	MGLM-2	1.6767	301	22.84
DB-7	19	MGLM-2	1.6767	301	23.41
DB-7	20	MGLM-2	1.6767	301	16.32
DB-13-1	3	LGLM-1	0.8883	160	18.39
DB-13-1	10	LGLM-1	0.9167	161	13.33

Porosity approximation from PSD-plots

Table 4: Porosity approximation of cumulative porosity plot for LGLM-1. The calculated D value for the associated EF-plots are also listed

LGLM-1 Image ID	Porosity at pore sizes (um2)					
	10	50	500	5000	10000	D
DB-13-1-01	1.93	8.04	31.34	84.26	95.84	0.60
DB-13-1-05	1.43	6.63	26.01	79.85	86.33	0.58
DB-13-1-12	2.81	10.30	35.99	85.80	97.56	0.63
DB-13-1-14	4.54	16.58	47.13	80.02	87.42	0.72
DB-13-1-15	1.71	6.47	21.83	61.06	81.71	0.60
DB-13-1-16	1.88	6.38	25.80	75.80	90.21	0.58
DB-13-1-17	2.52	9.45	32.13	78.52	90.53	0.63
HR-2-01	1.45	5.30	22.97	72.72	85.94	0.56
HR-2-02	1.10	4.10	17.95	50.38	62.36	0.56
HR-2-03	1.39	5.60	23.44	76.46	87.00	0.56
HR-2-04	1.19	4.77	21.10	63.89	81.86	0.55
HR-2-05	1.20	5.10	23.93	74.69	90.41	0.54
HR-2-06	1.04	4.47	20.61	67.35	79.70	0.55
HR-2-07	1.26	4.96	18.97	57.78	71.48	0.58
Mean	1.8	7.0	26.4	72.0	84.9	0.59
Stdev	0.9	3.3	7.9	10.5	9.3	0.005

Table 5: Porosity approximation of cumulative porosity plot for MGLM-2. The calculated D value for the associated EF-plots are also listed.

LGLM-2	Porosity at pore sizes (um2)					
Image ID	10	50	500	5000	10000	D
DB-3-01	2.94	10.00	33.33	83.02	94.45	0.65
DB-3-05	5.07	16.07	47.87	96.15	100.00	0.71
DB-3-07	3.52	10.41	31.08	73.49	87.87	0.68
DB-3-11	3.28	11.01	37.58	85.51	97.68	0.64
DB-3-12	3.59	10.61	31.97	80.76	92.22	0.67
DB-3-13	2.97	9.44	30.51	80.82	93.12	0.64
DB-3-14	3.60	11.20	36.46	83.75	95.05	0.66
DB-3-15	2.70	8.81	29.00	78.53	90.31	0.64
DB-3-16	1.83	5.95	21.98	70.15	87.16	0.59
DB-5-1-01	3.03	10.71	33.55	87.72	98.10	0.66
DB-5-1-05	2.89	11.29	41.12	92.20	100.00	0.64
DB-5-1-06	2.82	10.73	37.26	85.22	96.02	0.64
DB-5-1-10	2.99	11.14	37.77	90.56	98.17	0.64
Mean	3.2	10.6	34.6	83.7	94.6	0.65
Stdev	0.7	2.2	6.3	7.2	4.3	0.03

Table 6: Porosity approximation of cumulative porosity plot for MGLM-2. The calculated D value for the associated EF-plots are also listed.

LGLM-3	Porosity at pore sizes (um2)					
Image ID	10	50	500	5000	10000	D
DB-1-1-01	6.11	13.03	34.51	80.32	93.95	0.76
DB-1-1-05	5.54	12.40	29.03	76.35	89.22	0.76
DB-1-1-06	6.87	15.38	39.40	84.96	95.92	0.77
DB-1-1-07	5.63	13.03	35.03	85.96	98.01	0.73
DB-1-1-09	6.43	14.88	40.55	86.41	96.74	0.75
HR-5-06	4.85	13.06	37.27	88.33	96.04	0.70
HR-5-07	5.41	14.63	38.13	87.91	92.55	0.73
HR-5-08	7.82	20.02	50.06	90.76	100.00	0.78
HR-5-09	6.42	17.87	46.94	88.22	96.01	0.75
HR-5-10	3.80	10.29	29.39	74.06	87.63	0.68
Mean	5.9	14.5	38.0	84.3	94.6	0.74
Stdev	1.1	2.8	6.7	5.6	3.8	0.03

Table 7: Porosity approximation of cumulative porosity plot for MGLM-2. The calculated D value for the associated EF-plots are also listed.

| MGLM-2 | Porosity at pore sizes (um2) | | | | | |
Image ID	10	50	500	5000	10000	D
DB-7-01	5.94	16.22	45.11	89.75	99.27	0.72
DB-7-02	5.11	13.94	40.77	91.47	99.33	0.70
DB-7-03	6.29	18.32	55.05	92.18	95.44	0.72
DB-7-04	2.62	14.45	52.75	89.92	94.42	0.72
DB-7-07	5.66	16.41	47.13	88.85	96.90	0.69
DB-7-08	4.79	13.79	39.78	83.95	93.61	0.70
DB-7-12	5.85	16.42	49.03	93.83	99.25	0.71
DB-7-16	4.21	12.09	38.62	89.01	94.60	0.67
DB-7-85	3.62	11.51	38.66	79.67	88.87	0.67
DB-7-87	3.76	13.60	48.59	90.60	97.20	0.66
DB-7-96	3.05	10.66	39.57	86.70	95.48	0.63
HR-3-08	7.93	22.45	61.71	100.00	100.00	0.76
HR-3-09	8.39	25.95	64.40	96.09	97.38	0.78
HR-3-10	7.22	21.66	56.82	88.81	95.10	0.76
HR-3-11	9.44	30.14	71.82	100.00	100.00	0.79
HR-3-12	3.80	12.60	43.78	90.29	99.15	0.65
Mean	5.5	16.9	49.6	90.7	96.6	0.71
Stdev	2.0	5.5	10.1	5.2	3.0	0.05